University of California
Santa Barbara

Epitaxial growth and magnetotransport studies of the topological pnictide Cd_3As_2

A dissertation submitted in partial satisfaction of the
requirements for the degree of

Doctor of Philosophy

in

Materials

by

Binghao Guo

Committee in charge:

Professor Susanne Stemmer, Chair

Professor John W. Harter

Professor Bolin Liao

Professor Stephen D. Wilson

June 2024

The Dissertation of Binghao Guo is approved:

Professor John W. Harter

Professor Bolin Liao

Professor Stephen D. Wilson

Professor Susanne Stemmer, Committee Chair

January 2024

This dissertation is dedicated to my parents,
S. Guo
& J. Zhang

Acknowledgements

I am indebted to many individuals for their support that has made this dissertation possible.

- I would like to first thank my advisor, Prof. Susanne Stemmer, for providing the opportunity to do research in her group, for the encouragement and the enthusiasm about my work, for always keeping her door open for conversations about science, and for patiently guiding me in the right directions before I knew it.

- I am grateful to my committee members—Prof. J. Harter, Prof. S. Wilson, and Prof. B. Liao—for their willingness to engage in discussions on my research topic, for sharing their experimental expertise, and for overseeing all my exams. I would also like to thank excellent theory collaborators, Prof. Xi Dai and Wangqian Miao, for the many late night (early afternoon) video calls and the advice that has been instrumental in interpreting our data.

- In the Stemmer group, the past and present members have generously shared their insights and wisdom. I am particularly grateful to Manik Goyal, David Kealhofer, Luca Galletti, Timo Schumann for mentoring me soon after I joined. I not only shared an office with Alex Lygo, but more importantly, all the ups and downs of the graduate student life. I am proud to call him my closest friend in the group. I had the privilege of also knowing and working with Omor Shoron, Tyler Pardue, Salva Salmani-Rezaie, Honggyu Kim, on Cd_3As_2 projects. It has also been a pleasure to work with newer members, Guomin Zhu, Sina Ahadi, Jacob Brady, and William Huynh. Lastly, mentoring the undergraduate students, Pablo Cuadros Romero and Victor Huang, has been as rewarding for me as I hope it has been for them.

- It's only after leaving that one truly appreciates the privilege of working in the various shared labs at UCSB. Members of the MBE lab, managed by Kurt Olsson and John English, have saved me from countless technical mistakes and taught me all I know about epitaxial growth. I am particularly grateful to Jason Dong, Aaron Engel, Hadass Inbar, and Prof. Chris Palmstrøm for being reliable sources of MBE knowledge. In addition, the Materials department staff, Paul Sarte and Amanda Strom, trained me in the LowT lab and were always there to listen and offer advice. Ravit Silverstein, Arda Genc, and Tom Mates, provided expert assistance in the Microscopy facilities, helping me experience the excitement of taking my first HR-STEM images. In the Physics department, Liam Cohen and Prof. Andrea Young, offered timely support and patiently helped me design better transport experiments. Last but not least, I am grateful to the dedicated staff of the UCSB NanoFab, particularly Don Freeborn, Demis John, and Brian Thibeault.

- I would like to acknowledge the National Science Foundation for supporting me through their fellowship programs, including the Graduate Research Fellowship (Grant No. 2139-319) and the Quantum Foundry Fellowship (DMR-1906325).

- I am deeply grateful to my wonderful girlfriend Emily Morgan, for the unconditional love and support during graduate school and these pandemic years. This is only the beginning of good things to come. I also cannot forget my meekest chinchillas, Tofu and Goji, who have always brought me a smile on my meekest days.

- Finally, I want to thank my parents, my brother, and my entire family. Words cannot express my gratitude for all they have done to support my education.

Curriculum Vitæ

Binghao "Evan" Guo

Education

2024 Ph.D. in Materials (expected), University of California, Santa Barbara
2019 B.S. in Materials Science & Engineering and Physics, Northwestern University

Awards & Honors

2021 NSF Graduate Research Fellowship
2020 UC Santa Barbara Quantum Foundry Traineeship

Publications & Preprints

10. W. Miao, **B. Guo**, X. Dai, S. Stemmer, Engineering the in-plane anomalous Hall effect in Cd_3As_2 thin films, [arXiv:2309.15457]
9. G. Zhu, **B. Guo**, S. Stemmer, Interface atomic structures in a cadmium arsenide/III-V semiconductor heterostructure, *APL* **123**, 223101 (2023). [10.1063/5.0173777]
8. **B. Guo**, W. Miao, V. Huang, A. C. Lygo, X. Dai, S. Stemmer, Zeeman field-induced two-dimensional Weyl semimetal phase in cadmium arsenide, *Phys. Rev. Lett.* **131**, 046601 (2023). [10.1103/PhysRevLett.131.046601]
7. A. C. Lygo, **B. Guo**, A. Rashidi, V. Huang, P. Cuadros-Romero, S. Stemmer, Two dimensional topological insulator state in cadmium arsenide thin films, *Phys. Rev. Lett.* **130**, 046201 (2023). [10.1103/PhysRevLett.130.046201]
6. **B. Guo**, A. C. Lygo, X. Dai, S. Stemmer, $\nu = 0$ quantum Hall state in a cadmium arsenide thin film, *APL Mater.* **10**, 091116 (2022). [10.1063/5.0102703]
5. **B. Guo**, A. C. Lygo, T. N. Pardue, S. Stemmer, Hall bar measurements of topological surface states of (001) cadmium arsenide thin films interfaced with superconductors, *Phys. Rev. Mater.* **6**, 034203 (2022). [10.1103/PhysRevMaterials.6.034203]
4. L. Galletti, A. Rashidi, D. A. Kealhofer, M. Goyal, **B. Guo**, Y. Li, C. Shang, J. E. Bowers, S. Stemmer, Quantum Hall effect of the topological insulator state of cadmium arsenide in Corbino geometry, *APL* **118**, 261901 (2021). [10.1063/5.0056357]
3. T. N. Pardue, M. Goyal, **B. Guo**, S. Salmani-Rezaie, H. Kim, O. Heinonen, S. Stemmer, Controlling the symmetry of cadmium arsenide films by epitaxial strain, *APL Mater.* **9**, 051111 (2021). [10.1063/5.0047933]
2. O. F. Shoron, M. Goyal, **B. Guo**, D. A. Kealhofer, T. Schumann, S. Stemmer, Prospects of terahertz transistors with the topological semimetal cadmium arsenide, *Adv. Electron. Mater.* **20**, 2000676 (2020). [10.1002/aelm.202000676]
1. M. Goyal, S. Salmani-Rezaie, T. N. Pardue, **B. Guo**, S. Stemmer, Carrier mobilities of (001) cadmium arsenide films, *APL Mater.* **8**, 051106 (2020). [10.1063/5.0002771]

Abstract

Epitaxial growth and magnetotransport studies of the topological pnictide Cd_3As_2

by

Binghao Guo

Within the family of II_3V_2 pnictides, cadmium arsenide (Cd_3As_2) is unique for hosting topologically non-trivial bands in its electronic structure. In the bulk limit, it is regarded as a model for topological Dirac semimetals because its inverted bands intersect each other along a 4-fold rotation axis, satisfying a linear dispersion relation without obstruction from nearby Fermi surfaces. When scaled to two-dimensions, the bulk topological bands of Cd_3As_2 can be further engineered to generate new electronic states.

This dissertation presents magnetotransport studies of (001) oriented Cd_3As_2 quantum wells that are grown by solid-source molecular beam epitaxy (MBE). Building on Chapter 1's introduction, Chapter 2 details the MBE growth and structural characterization of these thin film samples. This includes not only the Cd_3As_2 active region, but also the metamorphic (Al,In)Sb buffer, designed to accommodate the film/substrate misfit, and the GaSb capping layer, which is deposited at low temperatures. Chapter 3 then focuses on improvements made to both device fabrication and transport measurements of these quantum wells. This enabled the first demonstration of chemical potential-tuning across the bandgap of confined (001) Cd_3As_2 samples using an electrostatic top gate. Furthermore, an insulating $\nu = 0$ quantum Hall plateau, showing an unusual magnetic field dependence, was observed in an early generation quantum well. Higher mobility samples helped

to resolve the nature of this state, and more important, provided evidence of subband inversion in a range of well thicknesses near 20 nm. Next, Chapter 4 investigates the influence of an in-plane (Zeeman) magnetic field on samples belonging to the band-inverted regime. The transport data are consistent with a predicted topological phase transition from the inverted phase to an emergent 2D Weyl semimetal phase (2D WSM), driven by the in-plane field. In particular, the 2D WSM shows saturated resistivities $\sim h/e^2$ at charge neutrality, and a well-developed odd-integer quantum Hall effect under a small perpendicular magnetic field. These experimental findings are supported by a 4-band $\boldsymbol{k}\cdot\boldsymbol{p}$ model of Cd_3As_2 that incorporates first-principles, effective g factors. Chapter 5 shifts focus to provide a discussion of preliminary results on devices designed to evaluate hybrid interfaces between *ex situ* superconductors and (001) Cd_3As_2 quantum wells. Chapter 6 summarizes the key findings of this dissertation and describes future directions for MBE-grown Cd_3As_2 thin films.

Contents

Chapter 1

Introduction

1.1 Band topology engineering

Materials hosting topologically non-trivial bands in their electronic structure are at the forefront of condensed matter research. Originally a subject in mathematics, topology is now routinely applied as a theoretical framework for understanding a rich variety of electronic states in materials, such as the quantum Hall phases of two-dimensional electronic systems [1, 2], time-reversal invariant topological insulators [3, 4], and, more recently, topological superconductors [5] and topological semimetals [6].

From an experimentalist's viewpoint, the progress in this field is a result of both powerful theoretical modeling and the use of advanced semiconductor technology, often referred to as band structure engineering, to develop the materials that demonstrate and probe the predicted physics. Two celebrated examples illustrate this progress. The first is the experimental realization of the quantum spin Hall insulator in HgTe-based quantum wells [7], which was made possible by the precise control of film thickness at the Ångstrom-scale

using molecular beam epitaxy (MBE). The second example is the observation of the quantum anomalous Hall insulator (or Chern insulator) state in $(Bi, Sb)_2Te_3$ thin films that are magnetically doped by Cr [8], prepared using similar MBE techniques. These materials breakthroughs not only validate theoretical predictions [4, 9], but may also find application in quantum devices leveraging spin effects and low-dissipation charge transport [10]. It's therefore fair to argue that band structure engineering, particularly in the context of MBE, has expanded to include a new capability: the engineering of band topology.

1.2 Cd_3As_2 thin film platform

This dissertation explores the theme of band topology engineering, focusing on the topological pnictide compound cadmium arsenide (Cd_3As_2). Recognized as a three dimensional (3D) topological Dirac semimetal in its bulk form [11, 12], Cd_3As_2 serves as a foundation for generating novel topological phases. This is achieved in this dissertation through several strategies and their combinations: the development of effective gating to tune the chemical potential [13], the reduction of dimensionality (from 3D to 2D) by quantum confinement [13, 14], the application of in-plane magnetic fields [15], and, lastly, the integration with superconductors to form basic hybrid devices [16].

There are several factors driving research on Cd_3As_2 thin films. First, its unique, low-energy band structure is predicted to resemble the relativistic Dirac Hamiltonian in 3D momentum space [11] and is not obstructed by the Fermi surfaces of any overlapping bands. This positions Cd_3As_2, in particular, as a candidate material for transport and spectroscopic

experiments designed to detect the consequences of having a relativistic dispersion [6]. Second, the Dirac-like electrons of Cd_3As_2 possess a vanishingly small effective mass and high Fermi velocity, contributing to its high carrier mobilities [17], which have separately been known for this compound since 1959 [18]. Investigating the evolution of these material properties as the bands of Cd_3As_2 are perturbed and modified by external parameters, such as changes in film thickness, represents a promising area of research. Finally, epitaxial thin films of Cd_3As_2 have been successfully grown on III-V semiconductor substrates and buffer layers using MBE [19, 20]. Chapter 2 describes the growth and characterization of such Cd_3As_2 heterostructures, which serve as a platform for conducting transport experiments discussed later in this dissertation.

One important aspect to keep in mind, among the many opportunities offered by Cd_3As_2, is the predicted energy scale of the 3D Dirac nodes, which is less than 100 meV. This scale, E_D, is estimated by the separation between the upper and lower Lifshitz transition points [12]. For comparison, graphene, the prototype 2D Dirac semimetal, hosts linearly dispersing bands across an energy range of 1 eV, nearly an order of magnitude greater than that of Cd_3As_2. The detectability of the Dirac nodes in graphene is consequently much greater. This fact also emphasizes the need to develop strategies such as chemical doping or gating, as discussed in Chapter 3, to access the low-energy window of interest in Cd_3As_2 samples and to distinguish the Dirac nodes from other trivial band features [12].

1.2.1 Band structure

Understanding Cd_3As_2 starts from a description of its band structure in the bulk limit. A standard approach to modeling bands in compound semiconductors and semimetals is to apply $\boldsymbol{k}\cdot\boldsymbol{p}$ perturbation theory [21, 22, 23]. In brief, it involves representing the single particle wave function in terms of basis states with specific orbital characteristics and the knowledge of a small set of empirical parameters, which may be either determined from experiments or first-principles calculations. It is particularly applicable near high-symmetry points in the Brillouin zone and band edges, regions of the band structure that define the electronic properties. Point group symmetries further determine the allowed matrix elements in the effective $\boldsymbol{k}\cdot\boldsymbol{p}$ Hamiltonian of a crystal. As discussed later in Chapter 2, Cd_3As_2 heterostructures studied in this dissertation belong to the point group $4/mmm$ (or D_{4h}), such that the relevant symmetry generators are 4-fold rotation along c (C_{4z}), 2-fold rotation along a (C_{2x}), time reversal ($\mathcal{T}$), and inversion ($\mathcal{P}$). The $\boldsymbol{k}\cdot\boldsymbol{p}$ Hamiltonian $\mathcal{H}(\boldsymbol{k})$ for Cd_3As_2, up to second order in momentum $\boldsymbol{k}$, can be written as:

$$\begin{aligned}\mathcal{H}(\boldsymbol{k}) = &[C_0 + C_1(k_x^2 + k_y^2) + C_2 k_z^2]\sigma_0 s_0 \\ &+ [M_0 + M_1(k_x^2 + k_y^2) + M_2 k_z^2]\sigma_z s_0 \\ &+ A(k_x \sigma_x s_z - k_y \sigma_y s_0).\end{aligned} \tag{1.1}$$

where the basis states are $|\frac{1}{2}, \pm\frac{1}{2}\rangle$ and $|\frac{3}{2}, \pm\frac{3}{2}\rangle$, which originate from the atomic Cd $5s$ and As $4p$ orbitals. σ_i and s_j refers to Pauli matrices for the spin and the orbital components, respectively. The remaining parameters, C_i, M_i, A_i were determined by fitting the $\boldsymbol{k}\cdot\boldsymbol{p}$

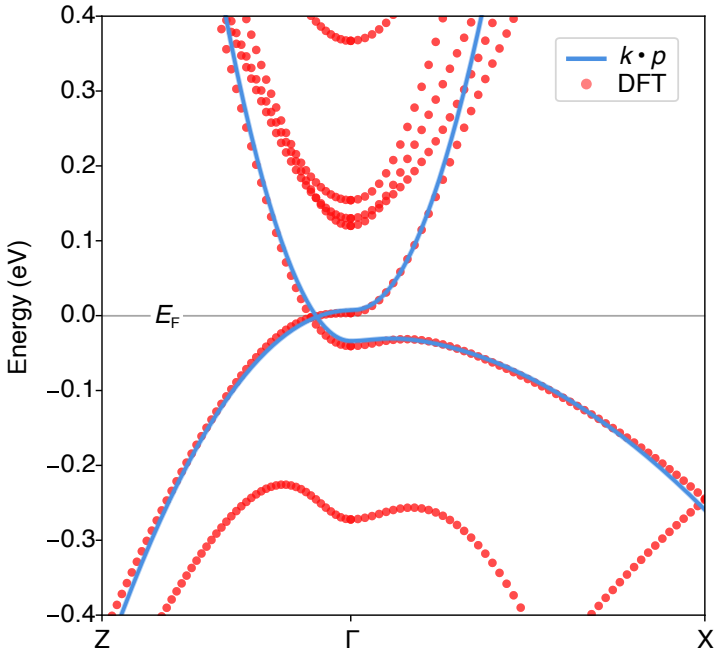

Figure 1.1: Calculated band diagram of Cd_3As_2 near a 3D Dirac node [15]. The results of the 4-band $\boldsymbol{k}\cdot\boldsymbol{p}$ model are drawn (as a blue trace) on top of the DFT calculations (red circles). The 3D Dirac nodes are located at $(0, 0, \pm\sqrt{-M_0/M_1})$, where M_0, M_1 are fitted parameters. The Fermi level E_F crosses through the 3D Dirac nodes, which are sufficiently isolated from nearby bands.

spectrum to results from density functional theory (DFT) band structure calculations of Cd_3As_2 in the $4/mmm$ point group (performed by W. Miao), which is consistent with the results of [24]. Among these material-specific parameters, M_0 and M_1 determine the locations of band crossing points in $\boldsymbol{k}$, which are exactly the 3D Dirac nodes. The nodes appear symmetrically around the Brillouin zone center at the positions:

$$k_x = k_y = 0, k_z = \pm\sqrt{-M_0/M_1} \approx \pm 0.03 \text{ Å}^{-1} \tag{1.2}$$

The 3D Dirac Hamiltonian can now be obtained by expanding $\mathcal{H}(\boldsymbol{k})$ around the crossing points and again retaining terms only up to second order in $\boldsymbol{k}$. The resulting magnitude

of the Fermi velocity that characterizes these nodes is calculated to be $\sim 1 \times 10^7$ cm/s [11]. Figure 1.1 presents the band diagram of Cd_3As_2 in the vicinity of a Dirac node calculated using the $\boldsymbol{k}\cdot\boldsymbol{p}$ approach, and overlaid on the first-principles DFT calculations. The symmetry considerations essential to constructing the 4-band $\boldsymbol{k}\cdot\boldsymbol{p}$ model also suggest why the Dirac nodes of Cd_3As_2 are topologically stable [25]. Although the concept of an inverted band structure in Cd_3As_2 has been acknowledged as early as 1977 [26], this feature alone does not guarantee a band crossing. Typically, band inversion leads to hybridization between states and an avoided crossing. However, in Cd_3As_2, the crossing along Γ-Z arises because the spin-degenerate bands contributing to the low-energy structure possess different C_{4z} eigenvalues [11]. This subtle but important distinction is what leads to Cd_3As_2 being classified as a band-inversion induced topological semimetal.

1.2.2 Quantum confinement

When Cd_3As_2 films are grown to lower thicknesses (~20 nm), they approach the two dimensional limit. As a consequence of the inverted 3D bulk bands, the subband states in this limit can also inherit inversion and develop non-trivial gapped Fermi surfaces. In this dissertation, the particular focus is on Cd_3As_2 grown in the [001] direction, with the 4-fold rotation axis of the crystal oriented out-of-plane. Cd_3As_2 films confined along [001] behave notably simpler than the more commonly studied (112)-oriented films [12] since they do not develop complex surface states, such as Fermi arcs [6].

Starting from the bulk $\boldsymbol{k}\cdot\boldsymbol{p}$ Hamiltonian, quantum confined (001) films can be understood using the model of an infinite potential well, which helps to illustrate the essential subband energy trends. Figure 1.2 shows the subband energies near Γ as a function of thickness for (001) Cd_3As_2 [27]. These calculations show qualitatively similar features to the tight-binding approach described in [11]. In general, the electron-like subbands trend downwards as thickness is increased, while the hole-like subbands trend upwards. The number of subbands in the relevant energy window also grows as thickness is increased. The result is in an oscillatory pattern in the nature of the band gap (and its size), similar to what is found in the Bi_2Se_3 compounds [28]. Within a specific range of film thicknesses, the band gap becomes inverted, indicated by conditions where a subband with hole-like characteristics is positioned higher in energy than an electron-like subband, which is also emphasized by the shading in Figure 1.2. Controlling the Cd_3As_2 thickness by MBE to realize a band-inverted ground state is discussed in Chapters 3 and 4.

1.3 Landau levels

Insight into the zero-field band structure of a quantum well is often gained by exposing it to a magnetic field in the out-of-plane direction. This approach inherently relies on the formation of quantized energy eigenstates known as Landau levels (LLs). Despite the diversity of phenomena in high magnetic fields, there are consistent features of LLs that reflect common underlying physics, which are briefly reviewed here. For charged particles confined to a finite area in 2D, the LL energy spectrum can be found by solving the

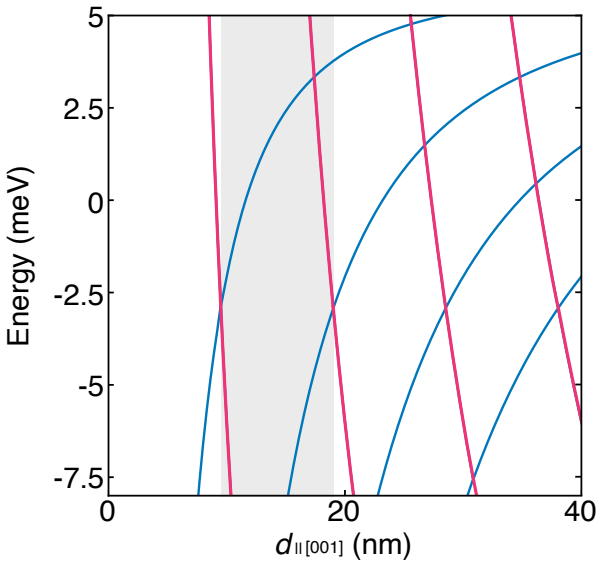

Figure 1.2: Subbands of Cd_3As_2 as a function of thickness in the (001) growth direction, using an infinite potential well approximation [27]. The shaded area highlights the initial range of film thicknesses where subbands are inverted. In experiments, band inversion is observed in ~16 nm to 22 nm films. Pink: electron-like subbands. Blue: hole-like subbands.

Schrödinger equation in a uniform magnetic field applied along the third dimension. The characteristic spectra of three different cases are introduced in the following.

First, in conventional semiconductors with a parabolic dispersion relation, the solutions, E_n, are those of the textbook quantum harmonic oscillator model:

$$E_n = \hbar\omega_c \left(n + \frac{1}{2}\right), \quad n = 0, 1, 2, 3... \tag{1.3}$$

where $\omega_c = eB/m^*$ is the cyclotron frequency, B is the magnetic flux density (commonly referred to as the magnetic field), m^* is the carrier effective mass, and n is a quantum number used to index the LLs. For a given B-field, the LLs of parabolic bands are equally spaced in energy, with $\Delta E = \hbar\omega_c$.

However, in massless Dirac bands with a linear dispersion, like those in graphene [29],

the situation is different and more interesting. In the case of graphene, the resulting LL spectrum, E_n^D, can be obtained as:

$$E_n^D = \alpha\sqrt{2e\hbar v_F^2 nB} = \alpha\hbar\frac{v_F}{l_B}\sqrt{2n}, \quad n = 0, 1, 2, 3... \tag{1.4}$$

where $\alpha = 1(-1)$ for the conduction (valence) band, v_F is the Fermi velocity, and $l_B = \sqrt{\hbar/eB}$ is known as the magnetic length. In graphene, the ratio of (v_F/l_B) can be viewed as the equivalent of the cyclotron frequency. In contrast to the parabolic case, the level spacing here depends on $(\sqrt{n+1} - \sqrt{n})$. Furthermore, the $n = 0$ LL is unique for appearing at zero energy, while every LL in the conduction band is mirrored in the valence band.

For completeness, it is important to mention the LL spectrum of massive Dirac bands, which also exhibit a low-energy linear dispersion but differ by having a bandgap. Compared to massless Dirac LLs, the spectrum, E_n^M, includes an additional mass term M, and can be expressed as:

$$E_n^M = \alpha\sqrt{2e\hbar v_F^2 nB + M^2}, \quad n = 0, 1, 2, 3... \tag{1.5}$$

The $n = 0$ LL in this case is no longer fixed to zero energy and E_n^M deviates from the ideal $E_n^D \propto \sqrt{n}$ relationship.

In general, since the wavefunctions of LLs are further subject to boundary conditions, each LL is associated with a number of electronic states. This is expressed as the level degeneracy, n_L, or the density of states per Landau level per unit area, which scales linearly with the B-field:

$$n_L = \frac{eB}{h}. \tag{1.6}$$

Additional system degeneracies, such as those due to spin or valley, will also enhance n_L. In addition, since the filling of LLs by charged particles determines many physical observables, it's useful to define the filling factor, ν, as the ratio between the charge density n in 2D and the LL degeneracy:

$$\nu = \frac{n}{n_L} = \frac{nh}{eB}. \tag{1.7}$$

The formation of LLs also underlies the observation of the well-known integer quantum Hall effect (QHE) in 2D materials under high B-fields. The QHE is signified by the appearance of series of plateaus in the measured Hall resistivity ρ_{xy}, while simultaneously, the longitudinal resistivity ρ_{xx} drops to near zero:

$$\begin{aligned} \rho_{xy} &= \frac{h}{e^2}\frac{1}{\nu}, \quad \nu \in \mathbb{Z} \\ \rho_{xx} &\to 0 \end{aligned} \tag{1.8}$$

(One of the most striking features of the QHE is the consistency of the plateaus across a diverse array of samples, highlighting the universality of this effect [1]). A semi-classical picture of the integer QHE can be briefly described using the Landauer-Büttiker method [30], which emphasizes the role of edge states. Considering a sample shaped into a Hall bar, all carriers of filled LLs are localized in the bulk of the sample, undergoing closed cyclotron motion, while the applied current is primarily carried by open orbits confined to the edges of the sample. Therefore, measuring ρ_{xx} along the same edge of the sample, i.e., the edge channels at the same chemical potential, produces zero signal. However, measuring ρ_{xy} involves edge channels at different chemical potentials, which are set by the voltage bias driving the current through the Hall bar. As a result, ρ_{xy} effectively measures ν, which can

be interpreted here as the number of edge channels in the integer QHE.

1.4 Permissions

- Chapters 1 and 4 include text and figures that have appeared in *Phys. Rev. Lett.* **131**, 046601 (2023). This article is copyrighted by the American Physical Society and reproduced with permission.

- Chapter 2 includes a figure reproduced from *APL* **123**, 223101 (2023) with the permission of AIP Publishing. This chapter also includes figures reproduced from *APL Mater.* **9**, 051111 (2021) with the permission of AIP Publishing. Both articles are licensed under a Creative Commons Attribution (CC BY) license.

- Chapter 3 includes text and figures reproduced from *APL Mater.* **10**, 091116 (2022) with the permission of AIP Publishing. This article is licensed under a Creative Commons Attribution (CC BY) license.

- Chapter 3 includes figures that have appeared in *Phys. Rev. Lett.* **130**, 046201 (2023). This article is copyrighted by the American Physical Society and reproduced with permission.

- Chapter 5 includes text and figures that have appeared in *Phys. Rev. Mater.* **6**, 034203 (2022). This article is copyrighted by the American Physical Society and reproduced with permission.

Chapter 2

Cd_3As_2 synthesis and characterization

This chapter describes the key aspects of growing heterostructures containing Cd_3As_2 by solid-source MBE as well as the materials characterization integral to this process. While introducing every part of the intricate systems that underpin the research in this dissertation is a nearly impossible task, the goal is to highlight some important considerations and challenges to growing the active region of (001) Cd_3As_2, the metamorphic (Al,In)Sb buffer, and the GaSb capping layer. Furthermore, this chapter will introduce basics of magnetotransport measurements, the primary tool used for evaluating material quality and characterizing Cd_3As_2 devices in subsequent chapters.

2.1 MBE system overview

Vacuum technology is the foundation of a molecular beam epitaxy (MBE) system. The central purpose of vacuum systems is to reduce the background pressure, thereby reducing the amount of impurities that could be incorporated into the thin film during growth. Behind the scaffolding and aluminum foil, the Cd_3As_2 MBE system is built simply from three vacuum chambers: the introduction chamber (or load lock), the buffer chamber, and the growth chamber. The upper panel of Figure 2.1 shows a wide-angle view of the system, which is responsible for producing all the Cd_3As_2 samples investigated in this dissertation.

The process of growth begins with the load lock, where a III-V substrate is placed for initial preparation. This chamber relies on a turbomolecular pump (speed ~250 liters/s), which exhausts into a dry scroll pump (~3 liters/s), to evacuate the space. In a first outgassing step, halogen lamps heat the vacuum surrounding the substrate to 150 °C, bringing the ultimate pressure inside to $\sim 1 \times 10^{-8}$ Torr. Having an introduction chamber for sample entry/exit is crucial to preserving the vacuum quality in subsequent chambers. The introduction of the substrate into the buffer chamber is then facilitated by a rail-guided trolley system. Thanks to a sputtering ion pump (anode voltage ~7 kV), the vacuum environment within the buffer is significantly improved, reaching levels as low as $\sim 5 \times 10^{-10}$ Torr. The ion pump, initially working together with the turbomolecular pump, efficiently reduces the pressure from atmospheric levels (760 Torr) to the desired vacuum in less than 4 hours. Before reaching the growth chamber, the substrate undergoes a second outgassing in the

buffer where it is heated locally to ~300 °C. The native oxide on the surface of the III-V substrate can also be removed at this stage in the buffer chamber by using a regulated flow of atomic hydrogen. Detailed steps for hydrogen cleaning are provided in Appendix A.

The substrate, after two outgassing steps, reaches the growth chamber, the final stage in the MBE system. The lower panel of Figure 2.1 provides a schematic illustration of the most frequently used subsystems attached to this chamber, excluding the cryopanel and a pyrometer (wavelength center ~2.3 μm) for simplicity. In the growth chamber, the base pressure is reduced even further, reaching as low as 5×10^{-11} Torr. This ultra-high vacuum (UHV) condition is sustained by a combination of pumps that are designed to capture the remaining gasses. Alongside an ion pump, similar to the one in the buffer, there is a cryogenic pump (~1500 liters/s) and a cryopanel that lines the chamber walls. A constant supply of liquid nitrogen is needed to keep these panels refrigerated. At this point, the residual gas in the chamber largely consists of hydrogen. This pump combination is a standard choice for III-V MBE chambers, which is in fact what this system was used for, prior to growing Cd_3As_2 in 2016.

2.1.1 The growth chamber

The subsystems on the Cd_3As_2 growth chamber are categorized into two essential groups. The first includes the effusion cells and the substrate heater which are crucial for the actual growth process. The second group comprises monitoring instruments, such as a beam flux monitoring (BFM) ion gauge and a residual gas analyzer (RGA), as well as a reflection

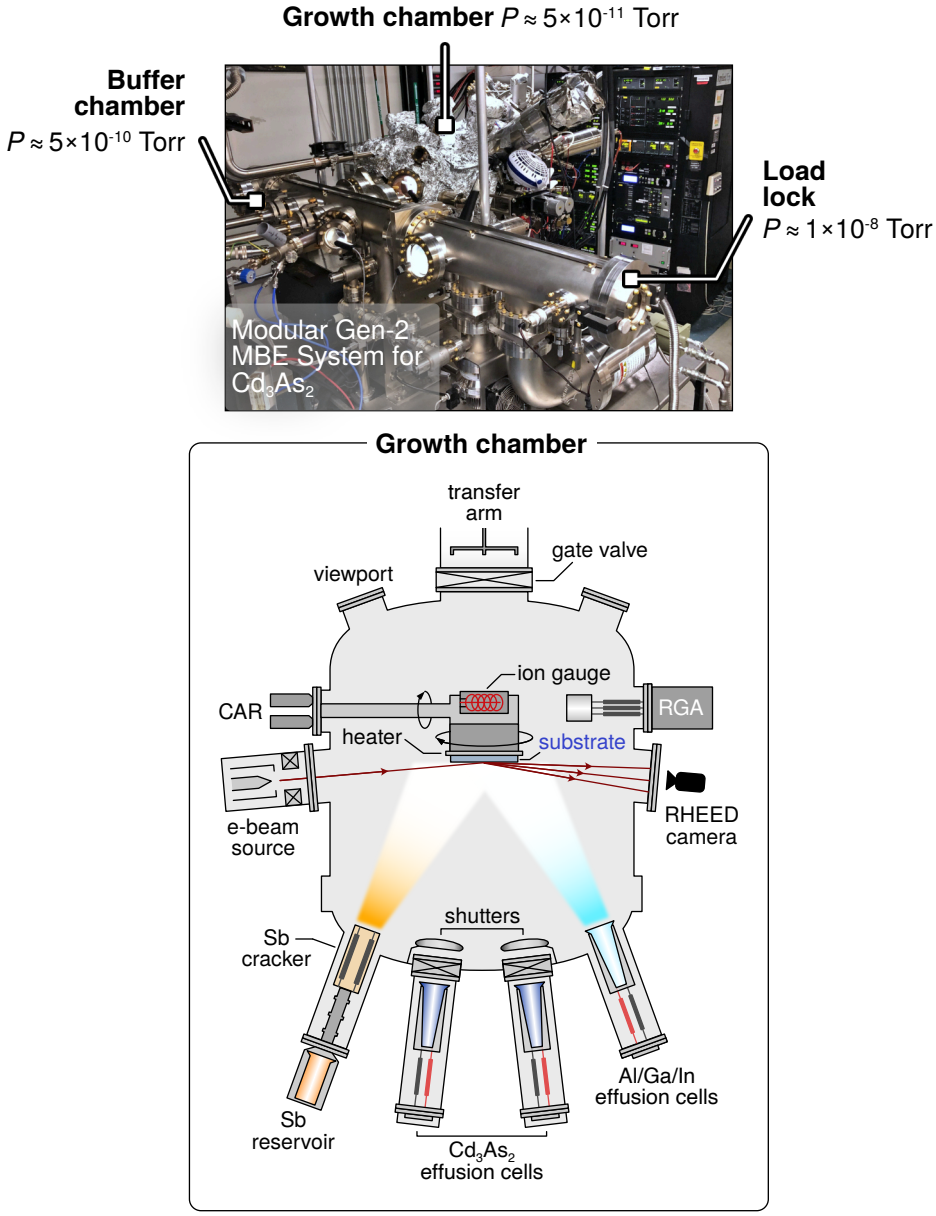

Figure 2.1: Overview of the Cd_3As_2 Gen-2 MBE system. (Top) photograph of the system, showing the three main vacuum chambers and their respective base pressures. (Bottom) illustration of subsystems in the growth chamber. Descriptions are provided in the text.

high energy electron diffraction (RHEED) setup that provides real-time feedback during growth.

The source flange of the Cd_3As_2 growth chamber contains 9 shutter-equipped pockets, which are used to mount 3 group-III element effusion cells (Al, Ga, and In), 2 group-V element cracker sources (Sb and As), 2 doping cells (Be, Eu), and 2 identical compound Cd_3As_2 effusion cells that can be retracted without breaking the vacuum of the chamber. A guide to maintenance procedures for these retractable cells (which are built with standard effusion cells like those of the group-III sources) is provided in Appendix B. Given that the charges in the group-III cells are melted under their operating conditions, they are positioned in upward-facing pockets to prevent spillage. In contrast, the group-V cells, containing solid or powder-like charges, are typically mounted in downward-facing positions. The Cd_3As_2 cells, whose contents are discussed later, remain solid at their relatively low operating temperatures, allowing them to be placed in either orientation. However, when mounted downwards, installing a Ta mesh in the crucible is necessary to keep the Cd_3As_2 pieces stationary. As noted earlier, the advantage of growing Cd_3As_2 by MBE is that it can be nearly seamlessly integrated into a III-V MBE system with minimal modifications to existing technology.

2.1.2 The growth process

MBE growth involves directing a flux of molecular beams from the resistively heated effusion cells to a hot substrate to form the target epitaxial layers. The beam fluxes, and

their relative ratios, are determined by cell temperatures, while the temperature of the substrate (T_S), which is GaSb in this dissertation, is controlled by a radiatively coupled, resistive heater and monitored by a thermocouple from the back side. A second temperature reading is obtained from a pyrometer with a line of sight to the front side of the substrate. A drawback of this method is that the value given by the pyrometer is extremely susceptible to changes in emissivity as the conditions inside the MBE evolve. For example, arsenic (As) is known to exhibit a "memory effect" in vacuum chambers. When layers are grown with an excess of As, this causes the unheated pyrometer viewport to be gradually coated, which in turn skews the temperature measurements. Furthermore, at the low growth temperatures of Cd_3As_2 ($T_S \leq 300\ ^\circ C$), the pyrometer value mostly reflects the temperature of the liquified Ga used for gluing the substrate to a W face plate. Between these two methods to determine the temperature, more reliable thermocouple values can be achieved through practice with Ga bonding and 1-5 growths of the target recipe to optimize the substrate temperature.

The complexity of MBE growth comes from the rich kinetics and surface chemistry involved, contrasting with the purely thermodynamic view of crystal growth that focuses on the initial and final states. This concept can be illustrated using the Kossel crystal picture, as described in [32]. MBE thin film growth modes are traditionally classified into three regimes: layer-by-layer (Frank-van der Merwe), 3D cluster (Volmer-Weber), and monolayer-then-3D cluster (Stranski-Krastanov), with the names in parentheses indicating the pioneers of these respective growth regimes [32]. A vast amount of literature focuses

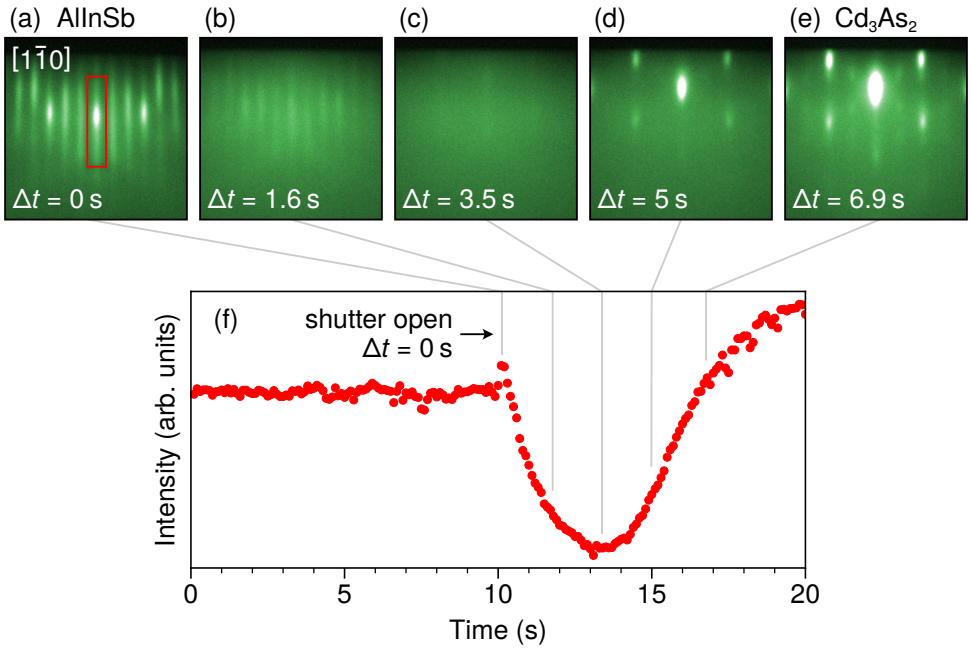

Figure 2.2: *In-situ* RHEED of (001) Cd_3As_2 growth on the standard $Al_{0.45}In_{0.55}Sb$ buffer layer, from [31]. (a) RHEED image with the beam parallel to [1$\bar{1}$0] of the buffer layer. The red box indicates the region over which the intensity of the specular beam was recorded. (b) - (e) RHEED images acquired at different times (Δt) after the Cd_3As_2 cells' shutters were opened. Imaging conditions are the same as in (a). (f) Integrated intensity of the specular beam as a function of time. The points where the RHEED images were recorded are indicated by gray lines. Substrate temperature: 180 °C. Cd_3As_2 beam equivalent pressure: $\sim 3 \times 10^{-6}$ Torr.

on studying the surface science of MBE-growth of III-V compounds, particularly through the use of *in situ* RHEED to investigate the growth modes. A typical RHEED experiment involves diffraction of 15 kV electrons at a grazing incidence from the sample surface, and is capable of providing local information of the surface layers.

For example, RHEED is regularly used to monitor the early stage of Cd_3As_2 growth on a standard $Al_{0.45}In_{0.55}Sb$ buffer, as illustrated in Figure 2.2. The RHEED image of the starting surface features streaks of intensity [Figure 2.2 (a)], which are intrinsically

tied to the smooth, 2D morphology of the surface. As the Cd_3As_2 layer starts growing, shown in Figures 2.2 (b)-(e), the image intensity drops but then recovers after ~5 s to produce a spot-like pattern. This transmission diffraction pattern indicates the completion of a 3D nucleation layer of Cd_3As_2, with a distinct surface crystal structure. As growth continues, the Cd_3As_2 layer will gradually smoothen out (not pictured). Preliminary results on the nucleation and growth of thin (001) Cd_3As_2 films under both higher flux and higher substrate temperatures are included in Appendix C.

Additionally, it's important to note the use of high-resolution x-ray diffraction (HR-XRD) as another reciprocal space characterization technique. Although HR-XRD shares some principles with RHEED, it is primarily employed to analyze the bulk crystallographic features of heterostructures post-growth, thus complementing RHEED's characterization capabilities. Together with routine measurements taken from the previously mentioned BFM gauge, HR-XRD (and x-ray reflectivity) measurements also enable calibration of the growth rate for the individual layers within the heterostructure.

2.2 Epitaxial (001) Cd_3As_2

All efforts in maintaining a clean vacuum environment within the MBE system are devoted to producing the highest quality Cd_3As_2 heterostructures possible. Figure 2.3 displays a photograph of an as-grown sample, alongside a cross-sectional schematic detailing the sample layers, which will be further described in the next sections.

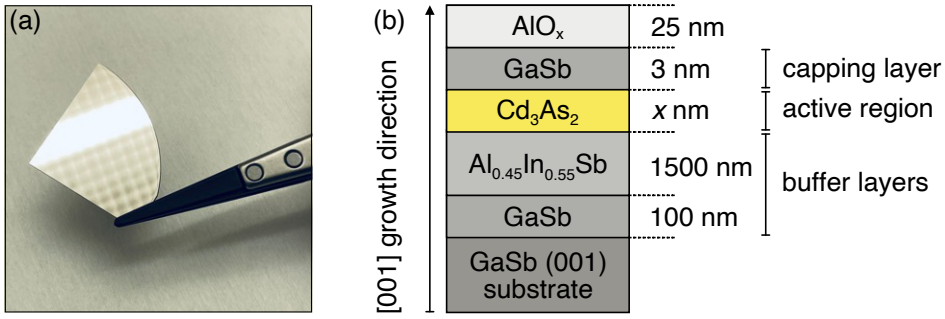

Figure 2.3: Cd_3As_2 heterostructures. (a) Photograph of a Cd_3As_2 film grown on III-V semiconductor layers. The reflections in the film are from the ceiling lights. Size: quarter of a 2" wafer. (b) Cross-section schematic of a typical (001) Cd_3As_2 sample grown on a GaSb substrate, including the buffer layers and the capping layer, with approximate thicknesses labeled. AlO_x is deposited *ex situ* as a gate dielectric.

2.2.1 Crystalline phases and symmetries

Cadmium arsenide, represented by the formula unit Cd_3As_2, can exist in several polymorphic forms. In particular, the compound undergoes three phase transformations while heated from room temperature under atmospheric pressure, as shown in the Cd-As system phase diagram in Figure 2.4 [33]. The polymorph that occurs in equilibrium at ambient conditions, α-Cd_3As_2, is the most extensively studied, topological Dirac semimetal phase, while the physical and electrical properties of other polymorphs, α'-, α''-, and β-Cd_3As_2, have received less attention in recent years [34, 35]. The β-Cd_3As_2 phase, which is cubic and present at high temperatures, exists as an exception among the Cd_3As_2 polymorphs. Apart from this phase, all Cd_3As_2 crystal structures adopt a tetragonal crystal form. Their structures can be viewed as a derivative of the anti-CaF_2 structure and are characterized by the absence of a quarter of the Cd metal sites. This vacancy ordering is essential to produc-

ing band inversion in α-Cd_3As_2, as first-principles band structure calculations have shown [11]. A detailed description of the crystal structure will be presented in a later section. For the sake of simplicity, α-Cd_3As_2 will simply be referred to as Cd_3As_2 in the remainder of this dissertation.

A survey of the phase diagram in Figure 2.4 provides a couple of insights: (1) At the Cd:As 3:2 stoichiometry, besides Cd_3As_2 there are no other competing thermodynamic phases, offering a chance to grow a phase-pure compound. (2) The phase stability of Cd_3As_2 is limited to temperatures below 225 °C. This relatively low thermal threshold places restrictions on MBE growth. Additionally, it suggests that device processing involving Cd_3As_2 must adhere to an equally low thermal budget.

The crystal structure of Cd_3As_2 is a topic of some recent debate. An early single crystal x-ray study [36] suggested that it belongs to space group 110 ($I4_1cd$), while a more recent publication [37] argues for the centrosymmetric space group 142 ($I4_1/acd$). The controversy mainly centers on whether Cd_3As_2 possesses an inversion center, which is an important detail because its absence is a necessary condition for the emergence of a topological Weyl semimetal state (along with the breaking of additional symmetries, i.e., a vertical mirror plane [11]). In light of this complexity, its important to understand the point group symmetries of (001) Cd_3As_2 thin films grown by MBE, particularly those on the now-standard $Al_{0.45}In_{0.55}Sb$ buffer layer. As noted in a later section, these Cd_3As_2 thin films are also subjected to slight biaxial compressive strain from the buffer layer at room temperature.

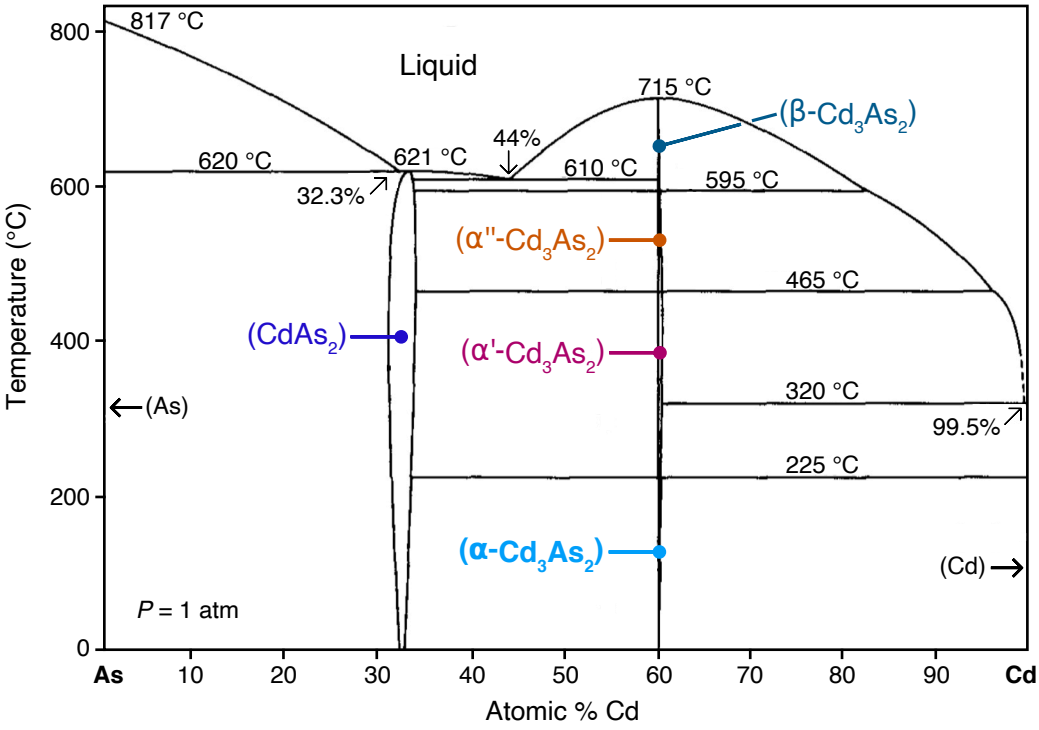

Figure 2.4: As-Cd equilibrium phase diagram. Adapted from [33]. The topological Dirac semimetal phase is α-Cd_3As_2, which is labeled in bold.

To study the point group symmetries of such samples, convergent beam electron diffraction was employed. This electron microscopy technique was previously applied successfully to relaxed, (112)-oriented Cd_3As_2 films that are centrosymmetric [39]. The convergent electron beam in this approach is incident on the specimen at multiple angles, thereby accessing both zeroth order and higher order crystal planes simultaneously, which makes it capable of providing three-dimensional symmetry information. Figures 2.5 (a)-(b) display the experimental diffraction patterns obtained along the $[1\bar{1}0]$ zone axis of a 30 nm (001)-oriented CdAs film [38]. The presence of two mirror planes in both patterns leads to the unique assignment of the diffraction group $2mm$, indicating that the film's point group

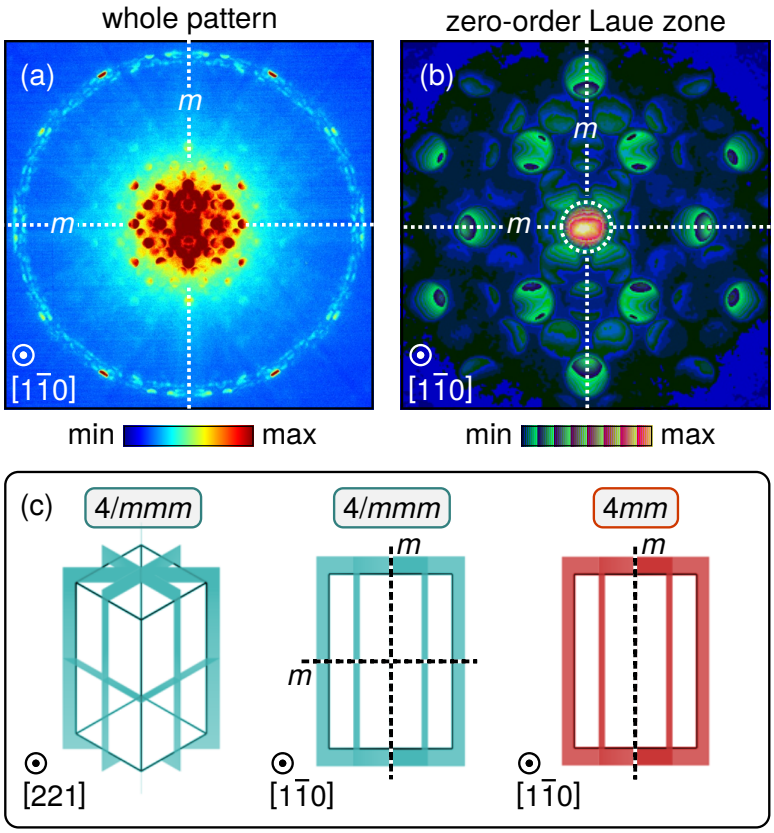

Figure 2.5: Point group symmetries of (001) Cd_3As_2 thin films. Convergent beam electron diffraction patterns along the [1$\bar{1}$0] zone axis, showing (a) the whole pattern and (b) the zero order Laue zone. Figures are adapted from [38]. In addition to the zero order Laue zone, the whole pattern also contains the first order Laue zone (diffuse outer circle). Mirror symmetry elements (m) of the diffraction group are labeled. (c) Schematics showing the two candidate point groups, 4/mmm and 4mm. The key difference is a horizontal mirror.

is 4/mmm [38]. This contrasts with the 4mm point group [36], which lacks a horizontal (ab-plane) mirror, as shown in the schematics of Figure 2.5 (c) and confirmed by simulations [39]. All the (001) Cd_3As_2 thin films discussed in this dissertation correspond to the centrosymmetric 4/mmm point group at room temperature, preserving all the symmetries found in the relaxed version of the compound [39].

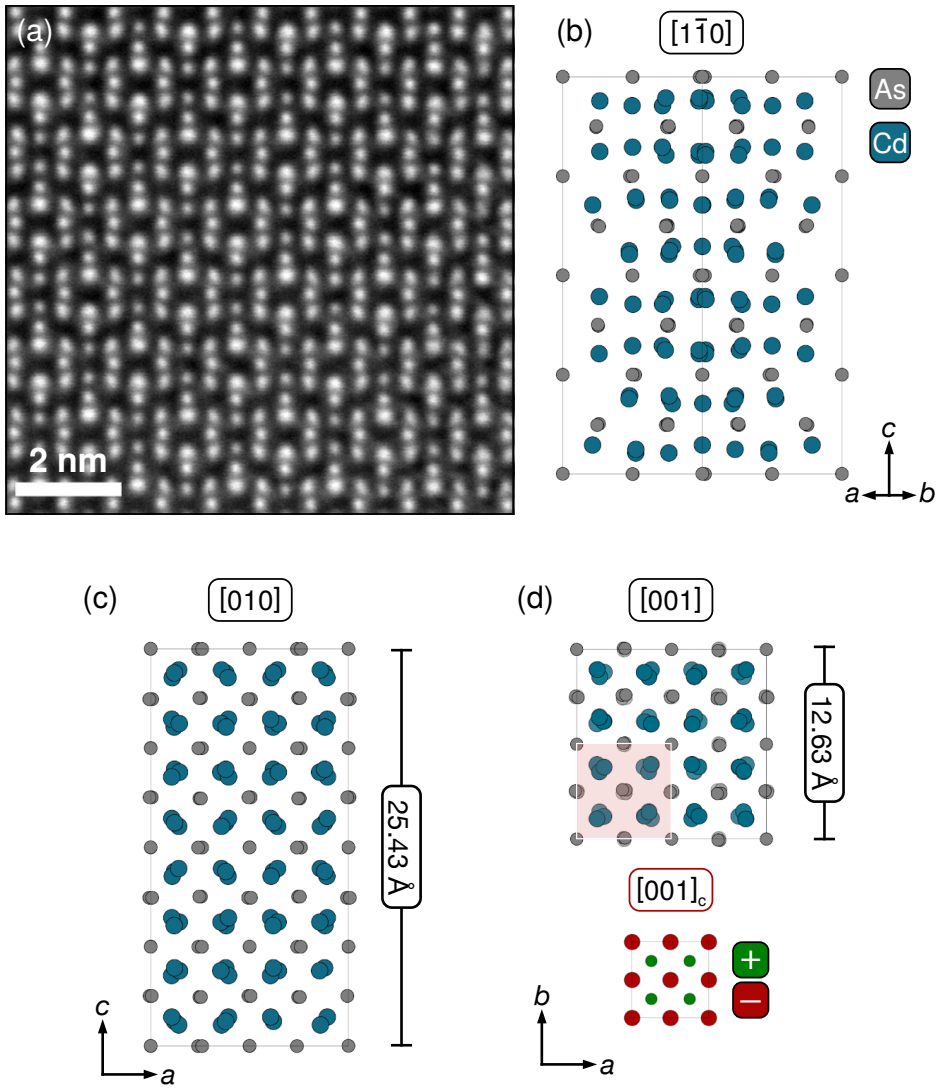

Figure 2.6: Crystal structure of epitaxial (001) Cd_3As_2 thin films. (a) HAADF-STEM image of Cd_3As_2 along the [1$\bar{1}$0] zone axis. The [001] growth direction points upwards. (b) Conventional unit cell viewed along the [1$\bar{1}$0] direction, same as in (a), showing alternating planes of Cd and As atoms. (c)-(d) Orthogonal projections of the unit cell along [010] and [001], respectively. The *a* and *c* lattice parameter lengths are indicated [37]. The [001] projection helps to illustrate the square-like arrangement of As atoms (shaded red) in Cd_3As_2, which is similar to the 4-fold symmetric anion arrangement in the cubic anti-CaF_2 unit cell, shown at the bottom of (d).

Next, having established the $4/mmm$ point group symmetry, the crystal structure is illustrated using the model in [37]. Figure 2.6 presents the atomic model next to an experimental, high-angle annular dark field (HAADF) scanning transmission electron microscopy (STEM) image of Cd_3As_2. This type of image is sensitive to the nuclei's Coulomb potential, resulting in the heavier Cd atomic columns appearing slightly brighter than the As columns. Images of this kind are thus interpretable on an intuitive level. As shown in Figure 2.6(a)-(b), the unit cell of Cd_3As_2 is composed of alternating layers of Cd and As planes, arranged perpendicular to the [001] direction, characterized by lattice parameters a = 12.63 Å and c = 25.43 Å [37]. As a result of Cd vacancy ordering, the conventional unit cell contains an unusually large number of atoms (n = 160), with the specifics of this vacancy arrangement detailed in [37]. For the growth of (001) thin films, it is important to note that the As atoms remain almost undistorted relative to their arrangements in the cubic anti-CaF_2 unit cell, as shown in Figure 2.6(d). It becomes practical to therefore adopt a pseudo-cubic in-plane lattice parameter of a_{pc} = 6.32 Å for Cd_3As_2. The challenge, and consequently the intrigue, in producing high-quality Cd_3As_2 lies in developing a compatible substrate with a lattice parameter close to 6.3 Å.

2.2.2 Vapor pressures and compound sources

From the beginning, our group has pursued a distinctive approach to Cd_3As_2 MBE. While other research groups have successfully achieved MBE growth using separate Cd and As effusion cells [40, 41], the method here is to use compound Cd_3As_2 cells [19]. This is based

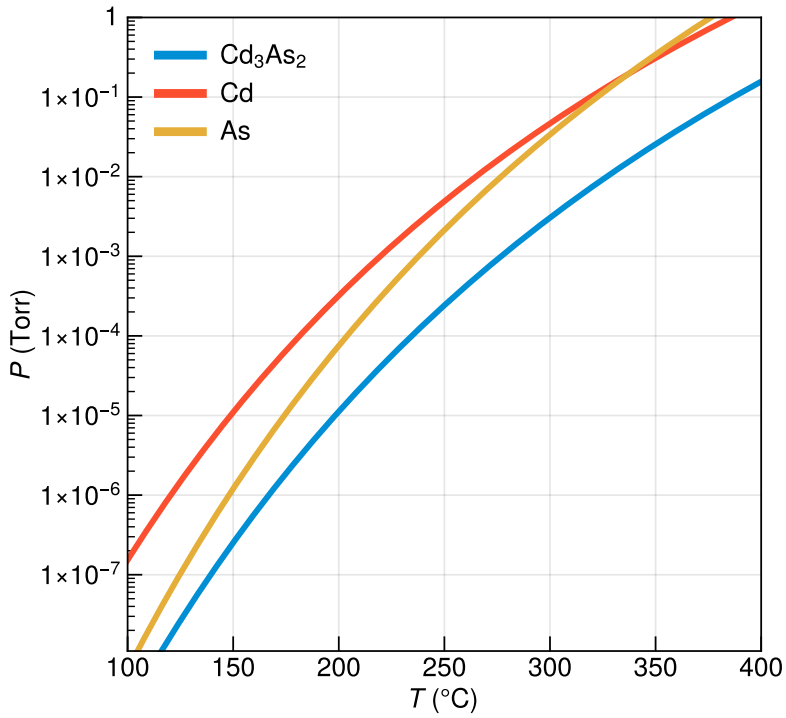

Figure 2.7: Equilibrium vapor pressures of Cd_3As_2 and its elemental constituents. Parameters for Cd and As were obtained from [46], and parameters for Cd_3As_2 were from [42].

on experiments from the early 1960s [42, 43], which found that although the compound dissociates upon vaporization, it condenses from the vapor phase in its original stoichiometry. This characteristic suggests that the target stoichiometry can be effectively transferred during thin film growth using a compound source. Consequently, this bypasses the need to finely adjust Cd to As flux ratios. Recent studies, however, have started to explore the manipulation of the Cd to As flux ratio as a means to control defect concentrations in thin films [44, 45].

To demonstrate the advantage of a compound source, Figure 2.7 provides a comparison of the equilibrium vapor pressures (P) of Cd_3As_2 and its constituent elements, as a function

of temperature (T). These traces are estimates using the semi-empirical (Antoine) expression $\log(P) = A - B/T$, where A and B are material-specific constants. In particular, the trace for Cd_3As_2 was generated by interpolating data from a slightly higher temperature window [42]. An important observation from Figure 2.7 is that for a range of cell temperatures, the vapor pressure of Cd_3As_2 is lower than that of its constituent elements, indicating that it's more stable as a compound. The slight discrepancy between the estimated temperatures and the actual working cell temperatures, which are necessary to achieve our standard operating pressures, can be attributed to factors such as incomplete thermalization and variations in ionization efficiency. In the Gen-2 system, the two compound sources—CdAs1, which faces upwards, and CdAs2, facing downwards—are operated within a reservoir temperature range of ~320 °C to 350 °C, and are set to standby temperatures above 100 °C.

A related consideration in achieving higher quality thin films is often the purity of the source material. Semiconductor-grade materials are valued by how many "Ns" are present in their purity rating, with 7N5 (99.999995%) being sufficient for most electronic applications. Every "N" added indicates a higher purity and, correspondingly, a higher price. However, this rating system does not clarify the exact nature of impurities in the source material. The Cd_3As_2 pieces used for MBE in this dissertation have been sourced from two different suppliers, American Elements and UMC, and both have a 6N rating, which is the highest available. Table 2.1 lists example elemental impurities, in parts per million, as measured by inductively coupled plasma atomic emission spectroscopy. This measurement data was provided by the vendor (UMC) for the Cd_3As_2 batch loaded into

Table 2.1: Impurities in 6N Cd_3As_2 source material. Data provided by UMC.

Element	Al	Bi	Cr	Cu	Fe	Mg	Mn	Ni	Pb
(ppm)	<0.1	<0.1	<0.1	<0.1	0.4	<0.1	<0.1	0.1	0.5

the MBE at the end of 2022. The influence of impurities like Fe and Pb, which are known to create deep donor levels, i.e., *DX* centers, in conventional III-Vs [47], on the electrical properties of (nearly) semimetallic Cd_3As_2 remains an area for further exploration. Since the vapor pressures of these known impurities are also generally higher than that of Cd_3As_2, their impact at the normal cell operating temperatures (~ 330 °C) is possibly negligible. While systematic studies are pending, current results also indicate no observable variations in transport properties of Cd_3As_2 films grown from source material provided by different suppliers.

2.2.3 Thermal stability

An open question is the highest substrate temperature at which Cd_3As_2 epitaxy can take place. Understanding this is important for two reasons: First, the access to higher growth temperatures could potentially increase the growth rate and minimize inclusion of background impurities. Second, it determines the variety of layers that can be successfully grown atop Cd_3As_2, especially in the context of integrating Cd_3As_2 into more advanced heterostructures. To explore this temperature limit, an experiment was conducted based on the standard growth process, involving a ~ 20 nm Cd_3As_2 quantum well grown on a nearly-lattice matched (Al,In)Sb buffer. For the Cd_3As_2 layer, T_S was initially set to 168 °C,

and the fluxes of CdAs1 and CdAs2 were measured by the ion gauge on the substrate manipulator to be 1.69×10^{-6} Torr and 1.75×10^{-6} Torr, respectively. These fluxes possibly increased slightly as the source material achieved better thermalization over the course of the experiment.

Figure 2.8 shows RHEED patterns taken during the heating experiment. As a point of reference, Figure 2.8 (a) shows the surface of the buffer layer before starting the Cd_3As_2 growth. Under these growth conditions, nucleation lasts for approximately 6 s after the shutters are opened, leading to film coalescence by 80 s, as shown in Figures 2.8 (b) and (c), respectively. The shutters for the Cd_3As_2 sources were then closed, and the substrate heater was ramped up at 20 °C min^{-1}. Up to 300 °C, the RHEED pattern remained largely unchanged. However, beyond this point, the background intensity increased, diminishing the spot pattern associated with Cd_3As_2. Given the high vapor pressure of Cd_3As_2, this suggests that atoms on the surface might be re-evaporating, and marks an upper limit to the stability of the Cd_3As_2 surface when there is no intentional over-pressure.

To mitigate re-evaporation, the Cd_3As_2 source shutters were opened again, as shown in Figures 2.8 (g)-(i). Despite this, the intensity of the spot pattern continued to decrease with further increase in the substrate temperature. Eventually, as shown in Figure 2.8 (i), a ring pattern appeared, which is indicative of a polycrystalline surface. Figure 2.8 (j) shows a post growth, out-of-plane x-ray diffraction scan, which reveals no $00\underline{16}$ diffraction peak belonging to Cd_3As_2, confirming that both the film and its surface have turned polycrystalline (or degraded further) due to elevated substrate temperatures. This experiment

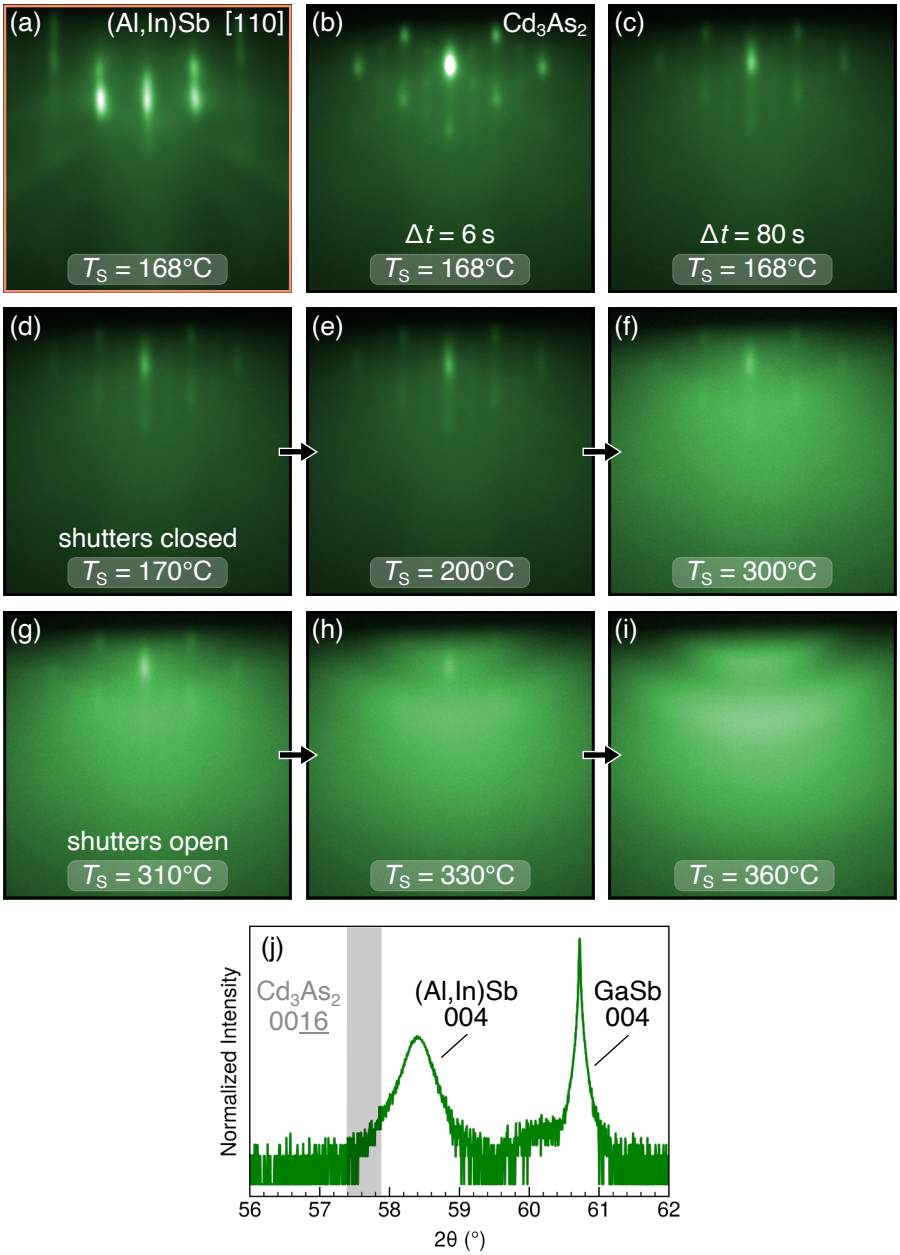

Figure 2.8: Thermal stability of (001) Cd_3As_2. (a) RHEED pattern along the [110] direction of the buffer surface. The incident beam orientation is fixed during the experiment. (b)-(c) Film surfaces after the Cd_3As_2 shutters had been open for 6 s and 80 s, respectively. After 80 s, the shutters were closed. (d)-(f) Film surfaces after the substrate temperature (T_S) had reached three different set points. The shutters remain closed. The background intensity increases noticeably at T_S of 300 °C. (g)-(i) Film surfaces at three increasingly higher set points, but with the shutters open. The spot pattern progressively transitioned into a semi-circular (ring) pattern. (j) Post-growth $2\theta/\omega$ scan using HR-XRD. Shading indicates where the Cd_3As_2 00$\underline{16}$ peak is expected.

therefore suggests that the upper temperature limit for Cd_3As_2 epitaxy is around 300 °C. Pushing this limit higher might be possible with increased source flux, but this comes with the trade-off of operating the cells at higher temperatures, and, as a result, more frequent refilling.

2.3 Metamorphic (Al,In)Sb buffer layer

Buffer layers are critical components of a high quality heterostructure, serving various functions. For example, once the protective oxide is removed from the GaSb substrate, a 100 nm to 150 nm layer of GaSb is typically re-grown. This is referred to as a homoepitaxial or homomorphic buffer. By growing this simple layer, the surface, following oxide removal, is effectively "buried" and made smoother. In the more common situation of heteroepitaxy, the lattice-mismatch, or misfit f, between the material of interest and the substrate is more significant. It can be defined as:

$$f = \frac{a_s - a_f}{a_s}. \tag{2.1}$$

where a_s is the lattice constant of the substrate, assumed to be unstrained due to its greater thickness, and a_f is the unstrained lattice constant of the film of interest. Given that the focus of this dissertation is on investigating the intrinsic properties of Cd_3As_2 films grown on GaSb substrates, which present a notable 3.3% compressive mismatch, the introduction of a buffer layer becomes essential to manage this misfit. This type of strain-relaxed buffer layer, designed to bridge differences in lattice constants and manage lattice defects, is known as a metamorphic buffer. The choice and design of a metamorphic buffer also presents

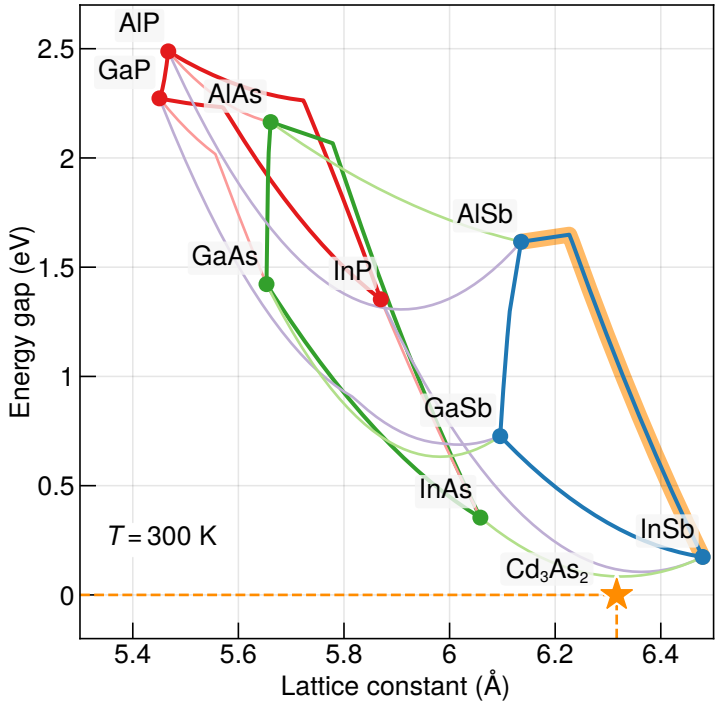

Figure 2.9: Bandgap variation with lattice constant for common III-V binaries and their ternary alloys (illustrated by lines). Kinks in the lines represent direct/indirect bandgap transitions as the alloy composition is tuned. On this plot Cd_3As_2 is represented by its pseudo-cubic lattice parameter of ~6.3 Å and with a bulk bandgap of 0 eV (or a negative bandgap) [37]. The compressive lattice mismatch between Cd_3As_2 and commercially available GaSb substrates is ~ 3.3%. The orange highlighted section represents a range of (Al,In)Sb ternary alloys, which are of interest for lattice-matching to Cd_3As_2. The band parameters at T = 300 K for bulk compounds are taken from [48].

opportunities to control specific properties of Cd_3As_2, including its bi-axial strain state and band offsets with III-V layers. Both of these aspects, especially the later, represent promising areas of research where much still remains to be explored.

Currently, optimal transport properties in Cd_3As_2 layers have been realized through growth on a nearly lattice-matched buffer composed of the ternary $Al_{0.45}In_{0.55}Sb$ compound. This approach builds on and refines earlier research conducted by our group [20].

To make the case for choosing this alloy, Figure 2.9 plots the energy gap versus lattice constant for common, non-nitride, III-V binary compounds and their ternary alloys. Cd_3As_2 is represented by its bulk, pseudocubic lattice constant (a_{pc} ~6.3 Å) and a bandgap of zero [37]. Around 6.3 Å, Figure 2.9 shows that alloys such as In(As,Sb), (Ga,In)Sb, and (Al,In)Sb are potential options, and in particular, the (Al,In)Sb alloy stands out with its largest (direct) bandgap. For the purpose of creating Cd_3As_2-based quantum wells, this property also makes (Al,In)Sb an appealing choice as a barrier material because it helps to eliminate parallel conduction in transport, which turns out to be a valid assumption.

A couple of interesting questions are raised in the mismatched epitaxy of (Al,In)Sb with the substrate and with Cd_3As_2. In direct growth of $Al_{0.45}Ga_{0.55}Sb$ on GaSb substrates with no intervening layers [20], the alloy relaxes above a certain thickness, also known as a critical thickness h_c, allowing line defects to form and lower the total energy of the heterostructure. Although the formation of such defects as misfit dislocations typically cost energy, this is offset by the reduction in misfit strain energy, which in the present case originates from the compression of atomic bonds. In well-studied III-V systems, this phenomenon of a critical thickness can be described by the Matthews-Blakeslee criterion [49]:

$$h_c = \frac{b\left(1 - \nu\cos^2\alpha\right)}{2\pi f\left(1+\nu\right)\cos\lambda}\ln\left(\frac{h_c}{b}+1\right). \tag{2.2}$$

where b is the length of the dislocation's Burgers vector, ν is Poisson's ratio, α describes the angle between the Burgers vector and the dislocation line direction, and lastly, λ describes the angle formed by the Burgers vector and the direction perpendicular to the line where the slip plane intersects with the interface plane.

One limitation of the h_c criterion is that it applies in the thermodynamic limit, which overlooks realities encountered in MBE, a process away from equilibrium. Kinetic constraints often play a more significant role and can impede the formation of dislocations. Consequently, even when the buffer layer's thickness surpasses h_c, it may remain strained. For the purpose of increasing the in-plane lattice constant to 6.3 Å, ensuring a relaxed buffer is essential. To determine the necessary thickness for the (Al,In)Sb layer, changes in the out-of-plane lattice constant are monitored through post-growth HR-XRD. Previous work [20] indicates that, under typical growth conditions with the Gen-2 MBE system, a minimum buffer layer thickness of ~1 μm is required. The resulting density of threading dislocations in Cd_3As_2 grown on this buffer, which are extended defects not completely confined to the buffer/substrate interface, was estimated to be on the order of 1×10^9 cm^{-2} [20].

In a Cd_3As_2 heterostructure, threading dislocations will terminate at surfaces, with the most prominent and accessible one being the Cd_3As_2 top surface. The nanoscale roughness of this surface can be partly attributed to disorder introduced by the threading dislocations that originate from the buffer. Atomic force microscopy (AFM) is therefore routinely used to inspect the surface morphology after growth, as shown in the example surface height maps presented in Figures 2.10 (a)-(b). For this particular Cd_3As_2 sample (covered by a thin layer of GaSb), the surface structure appears uniform across a 400 μm^2 area. It has a root mean square (RMS) roughness of 3.3 nm, which is comparable to the c-axis length of Cd_3As_2's conventional unit cell (~2.54 nm). Furthermore, in Figure 2.10 (c), which shows

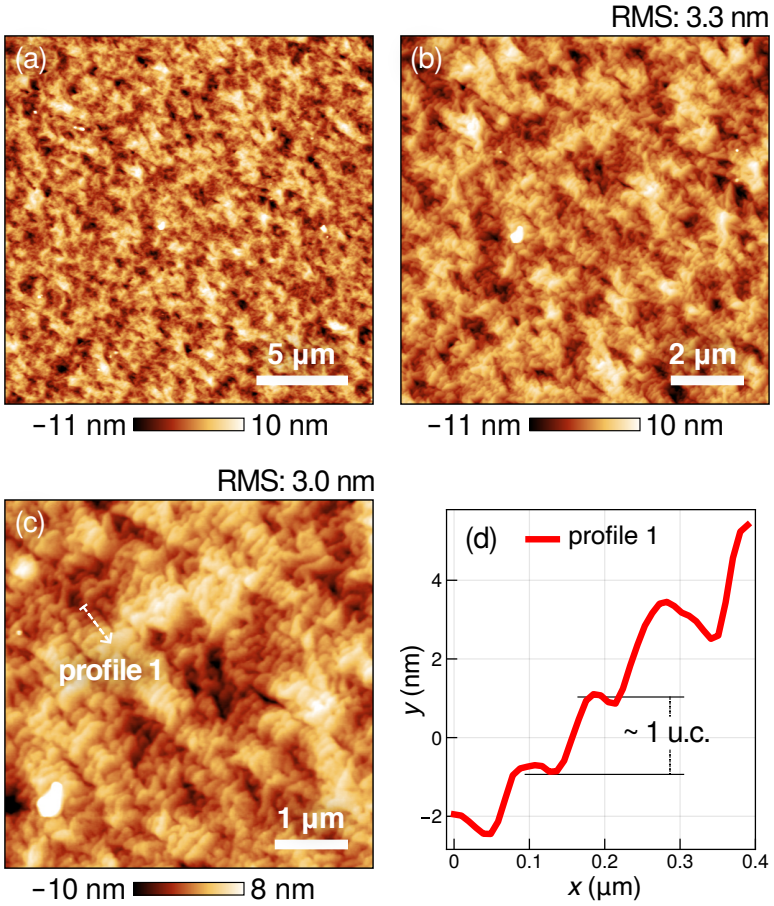

Figure 2.10: Surface morphology of a 20 nm (001) Cd_3As_2 film grown on a metamorphic $Al_{0.45}Ga_{0.55}Sb$ buffer. (a)-(b) Atomic force microscope height maps that provide an overview of the surface morphology. Note the differences in lateral length scales. The room mean square (RMS) surface roughness, for both images, is 3.3 nm, which is slightly greater than the c-axis length of the Cd_3As_2 conventional unit cell (~2.54 nm). (c) Height map showing finer features of the surface, such as steps indicated by the dashed line. The RMS roughness is 3 nm in this area. (d) Height profile along the dashed line in (c), emphasizing that steps are approximately 1 Cd_3As_2 unit cell tall.

a zoomed-in region on the same sample, there is evidence for atomic steps of Cd_3As_2 [also mapped in Figure 2.10 (d)], suggesting an acceptable level of crystalline quality with room for improvement.

2.3.1 Interfaces with Cd_3As_2

Until recently, the atomic-level structure of the interface between Cd_3As_2 and the metamorphic $Al_{0.45}In_{0.55}Sb$ buffer was not well-understood. This interface, similar to those in conventional III-V heterojunctions, plays a role in dictating charge transfer characteristics in the system, making its detailed study crucial. In the InAs/AlSb system, which provides a classic example of interface effects, the termination of the AlSb barrier layer during MBE growth is key to controlling the formation of anti-site defects [50]. This, in turn, significantly modulates the carrier density and mobility within the InAs quantum well.

By using an aberration-corrected scanning transmission electron microscope in HAADF mode, a technique shown earlier, the Cd_3As_2/buffer interface was directly imaged in a cross-section specimen [31]. The results indicate at least two type of interface structures exist, both characterized by a CdSb-like structure. Figure 2.11 depicts one of these atomically-abrupt interfaces. Evidence for an interface atomic arrangement distinct from the bulk of the Cd_3As_2 film can be more easily seen by mapping intensity profiles along two Cd atomic planes separated by 1 unit cell, as shown in Figures 2.11 (b) and (c). Notably, the Cd plane at the interface contains additional, periodically-distributed Cd vacancies. The observed interface structures align with expectations, considering that CdSb is the thermodynamically stable phase in the Cd-Sb system, with Cd_3Sb_2 being metastable [34]. The adoption of the CdSb-like structure therefore most likely serves to minimize the interfacial free energy. These findings underscore the importance of further work in modeling how this interface structure influences the electronic properties of the heterojunction.

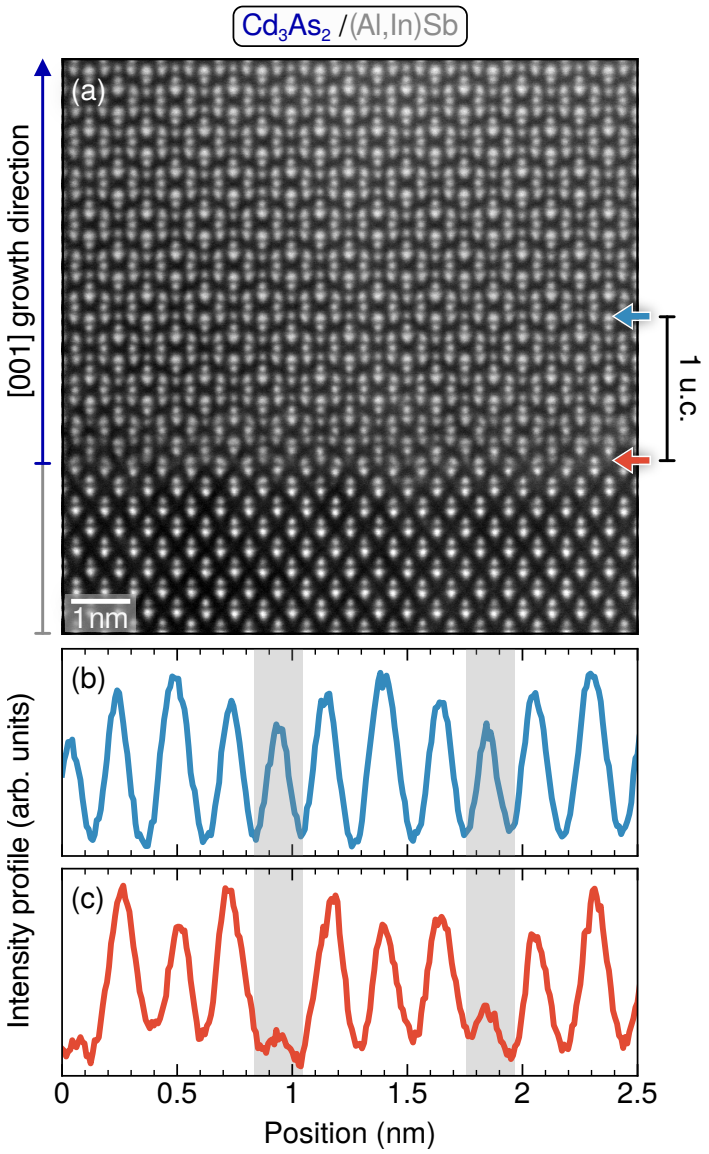

Figure 2.11: Interface between (001) Cd_3As_2 and $Al_{0.45}In_{0.55}Sb$. (a) HAADF-STEM image of a coherent interface along the [110] zone axis with the growth direction indicated. The red arrow marks the interface, below which the atomic columns of the buffer exhibit a characteristic dumbbell motif. Above the interface is the Cd_3As_2 layer with alternating planes of Cd and As atoms. Adapted from Figure 3(a) of [31]. (b) Intensity profile (integration width 0.05 nm) along a plane of Cd atoms in Cd_3As_2, indicated by a blue arrow, located a distance of 1 unit cell above the interface. (c) Intensity profile along a plane of Cd atoms at the interface, indicated by a red arrow. The shading in (c) indicates the locations of additional Cd vacancies at the interface.

2.3.2 Sb_2 flux control

A notable challenge while growing (Al,In)Sb on the Gen-2 is controlling the Sb molecular flux. Group-V molecular beams, such as As and Sb, are typically supplied with a valved effusion cell and thermally cracked into dimers for enhanced reactivity. The valve mechanism on this type of cell allows for a consistent and mechanically controllable supply of group V flux, while the bulk of the cell, also known as the reservoir, can remain uniformly heated. This reduces the need to frequently adjust reservoir temperatures and prevents flux instabilities. However, the Gen-2 system is limited by the fact its Sb thermal cracker source is un-valved, which means the Sb beam equivalent pressure needs to be constantly monitored. Figure 2.12 illustrates this challenge, showing a typical measurement of the Sb BEP over time. It highlights the nearly 2 hour stabilization period required for the Sb cell to reach, and more importantly, to maintain the desired temperature, which is key to long (~2 h to 3 h) buffer layer growths. In particular, it has been found that Sb flux stablized in the range of $\sim 4.5 \times 10^{-7}$ Torr to 4.8×10^{-7} Torr, for a given In BEP of $\sim 1.5 \times 10^{-7}$ Torr and Al BEP of $\sim 4.8 \times 10^{-7}$ Torr, produces the most consistent (Al,In)Sb growths. While it is possible to achieve higher beam fluxes with the un-valved source, even reaching into the low 1×10^{-6} Torr range, to facilitate increased growth rates, this approach also carries the risk of using a higher reservoir temperature that will deplete the charge more rapidly.

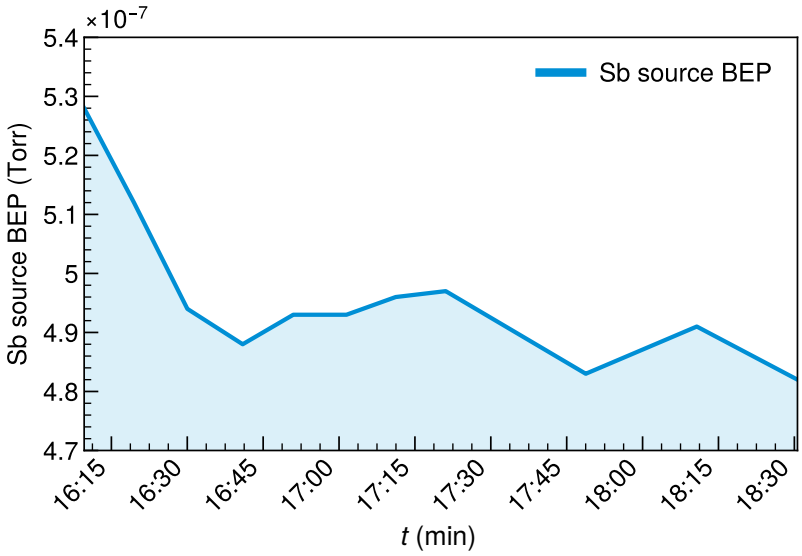

Figure 2.12: An example measurement of the Sb beam equivalent pressure (BEP) as a function of time. Prior to taking the first data point, the Sb cell reservoir was allowed to stabilize at 533 °C for 30 min. Each data point represents the difference between the average ion gauge reading when the shutter is open and the background reading when the shutter is closed. At least 2 hours was required for the BEP to settle at the target value $\sim 4.8 \times 10^{-7}$ Torr.

2.4 GaSb capping layer

As highlighted earlier in this chapter, the limited temperature range ($T_S \leq 300$ °C) for stabilizing Cd_3As_2 restricts the types of layers that can be epitaxially grown *in situ* on its surface. The most useful one would be a capping layer to slow down oxidation and shield the surface from detrimental chemicals in the ambient environment. Our group was primarily motivated to develop a capping layer due to the later reason, which was thought to be hindering the reliable fabrication of thinner films (less than 30 nm) into experimental devices [51]. An ideal capping layer would also need to be compatible with the surface chemistry of Cd_3As_2.

Considering the capabilities of the Gen-2 system, two options are available. An elemental capping layer, such as As or Sb, presents the simplest solution, but has yet to be explored. A III-V compound capping layer, despite the challenge of low temperatures, could however be made possible. The technique that enables this option is a variation of the layer-by-layer growth mode which is known as migration enhanced epitaxy (MEE) [52]. The fundamental idea is to synchronize the group III and V molecular beams with the layer-by-layer growth cycle. In conventional III-V growth where the two beams coexist (and the V flux is supplied in excess), group III adatoms see a high energetic barrier for surface diffusion and are nearly immobile at our target temperatures [53]. This implies that the conventional overpressure growth style at reduced temperatures would result in a 3D surface and incomplete coverage. But when just one beam is present, adatom migration can be appreciably enhanced [52] due to now having a higher concentration of unsaturated bonds. RHEED can be used to track intensity oscillations to determine the shutter timing for approximately monolayer coverage of each type of adatom, ultimately building up to a smooth, epitaxial III-V film.

Using the concept of MEE, homoepitaxy of GaSb was demonstrated at $T_S \sim 200\,^{\circ}\mathrm{C}$, much colder than the normal temperature range of 500 °C to 650 °C. Figure 2.13 summarizes the results of using a nearly optimized shutter sequence for GaSb/GaSb, showing qualitatively that the surface is 2D after growth, as evidenced by streaks in RHEED. To complete a monolayer (half a unit cell) of GaSb, the Ga shutter is first opened for 2.7 s, then closed, followed by a 3 s wait period, and then the Sb shutter is opened for 3.1 s and closed.

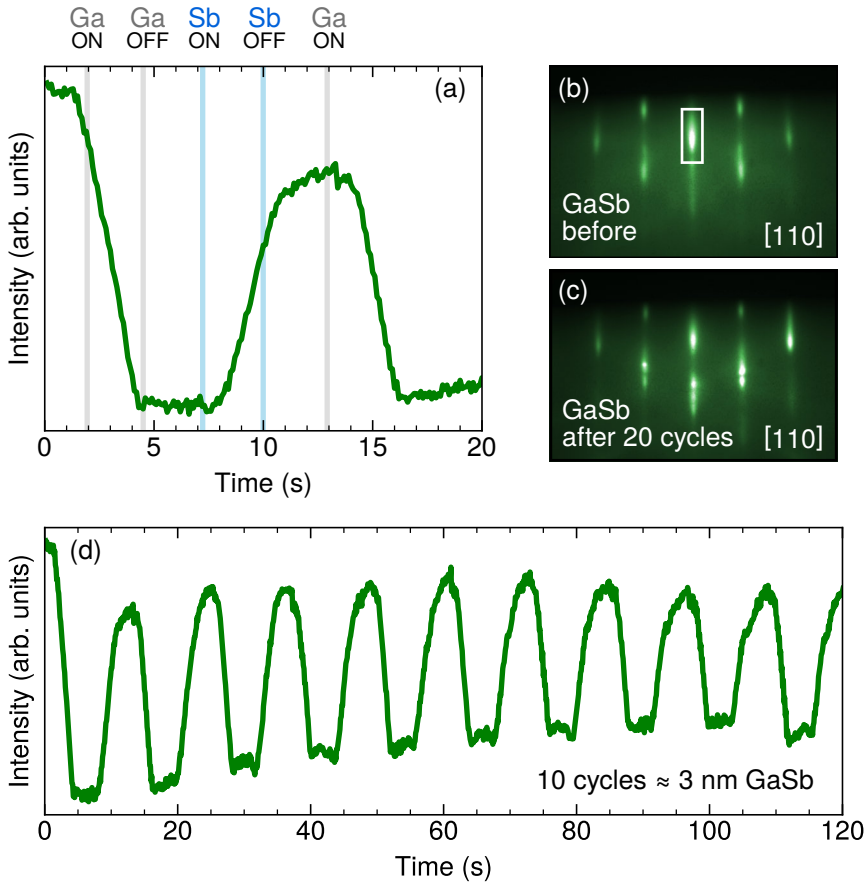

Figure 2.13: Epitaxy of GaSb at low substrate temperatures ($T_S \sim 200\,^{\circ}C$). (a) RHEED specular beam intensity as a function of time, acquired along the [110] direction, during one MEE-style growth cycle of GaSb. The Ga and Sb shutter sequences are labeled and detailed growth conditions are described in the text. (b)-(c) RHEED patterns after completing 20 cycles of GaSb growth. The white box indicates the area from which RHEED intensity data was recorded. (d) RHEED intensity changes recorded during 10 GaSb growth cycles, showing no signs of intensity damping that could suggest surface roughening.

The BEPs of Ga and Sb sources are set to 1.5×10^{-7} Torr and $\sim 2 \times 10^{-7}$ Torr, respectively. Additionally, it should be mentioned that applying this GaSb process to the Cd_3As_2 surface results in a RHEED pattern without clear crystalline characteristics and a diffuse background. Despite not being epitaxial, the capping layer should remain stoichiometric by using this shutter sequence. To enhance its crystallinity on Cd_3As_2, future efforts need

to focus on optimizing factors like wait times and slightly increased surface temperatures. The changes that this capping layer brought to transport characteristics of Cd_3As_2 will be discussed in the next chapter.

2.5 Magnetotransport fundamentals

Magnetotransport is a highly sensitive method for studying the low-energy behavior of carriers in semiconductor heterostructures. This technique, complementing the physical characterization methods previously introduced, not only gives information about fundamental properties of the Cd_3As_2 film's band structure with high resolution in energy, but also serves as a tool for providing feedback on sample growth activities. Its sensitivity to crystalline quality underscores its important role in research covered by this dissertation.

In efforts to improve material quality, an important quantity to measure is the low-temperature carrier mobility μ using the conventional Hall effect. According to semi-classical Drude theory, this parameter is directly linked to the transport scattering time τ_t of charge carriers, offering insights into electronic interactions. μ is typically expressed as:

$$\mu = \frac{e\tau_t}{m^*}. \tag{2.3}$$

where e is the elementary charge and m^* is the carrier effective mass. As shown, μ is directly proportional to τ_t, which represents the average duration a charged particle travels before experiencing a change in the direction of its momentum through a scattering event. Consequently, higher mobilities imply longer transport lifetimes, making the measurement of μ a useful indicator of the level of disorder due to scattering within the material system.

Viewed more optimistically, it provides a benchmark of how "clean" the epitaxial material is. τ_t itself can be written as:

$$\frac{1}{\tau_t} = \int W(\theta)(1 - \cos\theta)d\Omega. \tag{2.4}$$

In this expression, $W(\theta)$ represents the probability of a particle scattering through an angle θ, and this term is also known as the scattering matrix element. The integral is performed over all possible scattering angles, but is modulated by a factor of $(1-\cos\theta)$. This is included to emphasize the fact that, in this semi-classical picture of transport, large-angle scattering events have a stronger influence than other events at altering the paths of particles.

In the context of quantum transport, a more complete description of the particle lifetime treats all scattering events equally. This concept is summarized by the quantum scattering time τ_q, which can be written as:

$$\frac{1}{\tau_q} = \int W(\theta)d\Omega. \tag{2.5}$$

The quantity τ_q represents the average time a charged particle exists in a given momentum eigenstate before undergoing scattering. Experimentally, it can be accurately determined by measuring the thermal dampening of resistivity oscillations in a magnetic field [54]. It may also be roughly estimated from the onset magnetic field B_c for oscillations at a single temperature, which occurs at the well-known condition of:

$$\omega_c\tau_q = \frac{eB_c}{m^*}\tau_q = \mu_q B_c > 1. \tag{2.6}$$

where ω_c, the cyclotron frequency, was written out explicitly to introduce a parameter μ_q, which is known as the quantum mobility. Based on these definitions, calculating the

ratio between τ_t/τ_q, known as the Dingle ratio [54, 55], is therefore able to help narrow down the dominant source of scattering within the material. This is because different scattering mechanisms, such as short-range interface roughness scattering and long-range charged impurity scattering (via Coulomb interactions), have different dependencies on the scattering angle [54].

2.5.1 Cd_3As_2 devices

The majority of transport experiments in this dissertation has been performed using standard, lithographically defined Hall bars of Cd_3As_2. In measurements of this type of device, an electric current is set up to flow from the source to the drain contacts, while both the longitudinal and transverse (Hall) voltages are monitored between pairs of contacts positioned along the current path. Experiments are then carried out as a function of the applied magnetic field (strength and orientation), the temperature, and the gate voltage, in order to investigate a variety of transport phenomena. Making a functional Hall bar device, defined by having Ohmic contacts, minimal gate leakage, and the ability to withstand multiple cool-downs, is not trivial, especially given the limited literature and resources on Cd_3As_2 device fabrication. The main processing considerations are briefly outlined in this section, while the experimental setup for measuring low-temperature transport in these devices will be discussed in Chapters 3 and 4. Additionally, it is important to recognize that much of this processing workflow benefits from helpful discussions with Dr. M. Goyal.

Figure 2.14 shows the layout of a Hall bar equipped with a top gate, with a particular

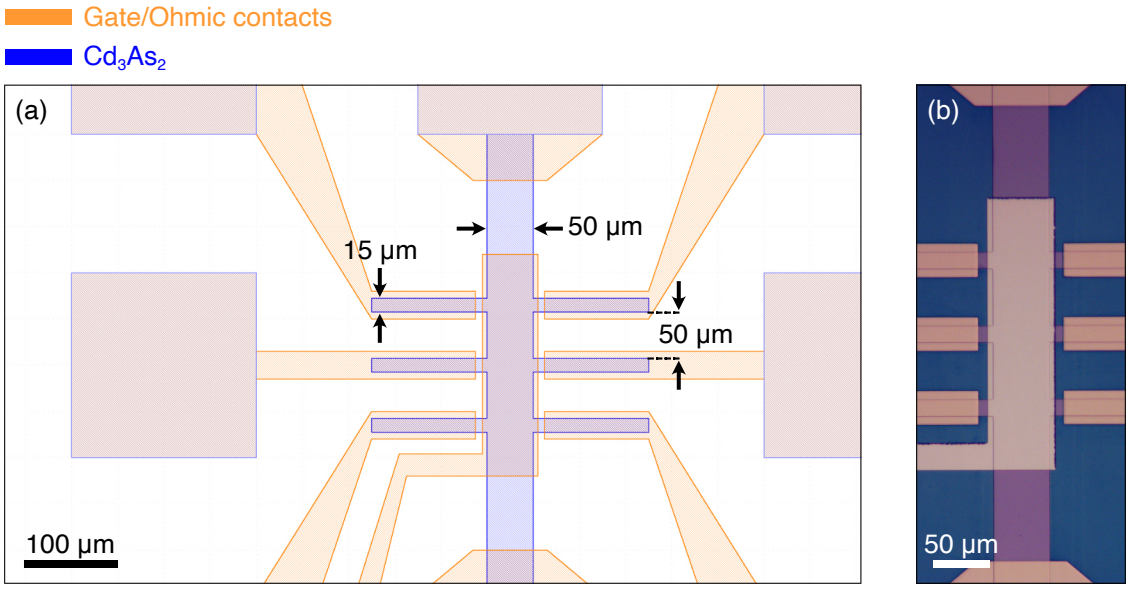

Figure 2.14: Layout of a Cd_3As_2 Hall bar. (a) Design of the different layers to be processed. The mesa is shaded light blue with a darker outline. The transport contacts and the gate contact are outlined in orange. The dielectric layer conformally covers all regions of the exposed device, apart from the square bonding pads. Relevant dimensions of the Hall bar are indicated by black arrows. (b) Optical image of a top-gated Hall bar after all fabrication steps were completed.

current channel width of 50 µm. The first step is patterning a mesa using photolithography to create well-defined current paths and voltage measurement contacts. This is achieved by ion beam etching with a remote plasma of Ar ions (accelerating voltage 0.5 kV). Because of its highly energetic mechanism, this step is often speculated to be the one that causes the most damage to the channel material. After a second round of lithography, Ohmic contacts are preferentially formed by magnetron sputtering of Au (power level of 200 W) using Ti (100 W) as an adhesion layer. This method is chosen in part because the platen that holds the sample can continuously rotate during the process, allowing for metal deposition on the sloped sidewalls of the mesa to minimize air gaps. Contacts extending over the

edge of the mesa are also key to measuring chiral edge states from the QH effect at high magnetic fields. The regions on the contacts designated for wire bonding to the chip carrier are then covered with resist, followed by the deposition of a dielectric consisting of AlO_x using atomic layer deposition (ALD). ALD offers a broad processing window such that this step can be carried out at ~ 120 °C, staying well within the thermal budget of Cd_3As_2. Finally, the gate metal is deposited over the top of the channel by thermal evaporation of Au while using Ni as an adhesion layer. Throughout this procedure, interfaces with minimal contamination were achieved by direct exposure to an oxygen plasma (100W for ~30 s) prior to each step.

Chapter 3

Gate-tunable quantum wells

This chapter introduces electrostatically gated Cd_3As_2 quantum wells as the primary type of sample investigated by magnetotransport in this dissertation. It discusses improvements to gate performance, achieved by adding the GaSb capping layer and performing an *ex situ* oxygen plasma cleaning step before dielectric deposition. These material improvements enabled studies of an insulating $\nu = 0$ state, in an early generation Cd_3As_2 sample near charge neutrality, with an unusual dependence on the magnetic field. In the gate voltage and magnetic field parameter space (B-V_g), the Landau level spectra of Cd_3As_2 quantum wells grown on the $Al_{0.45}In_{0.55}Sb$ buffer were also successfully mapped. Evidence of band inversion was found for a range of Cd_3As_2 well thicknesses, consistent with the quantum confinement model of (001) thin films introduced in Chapter 1.

3.1 Gate performance

Controlling the carrier concentration of a semiconductor, and therefore its chemical potential level, provides an important experimental degree of freedom. The ability to continuously modulate the carrier density within a single sample facilitates a comprehensive analysis of its band structure and expands the scope of potential transport experiments, particularly for micron-scale devices. A common method to achieve this modulation is through electrostatic gating. The basic idea here is to deposit, using ALD, a thin aluminum oxide (AlO_x) dielectric layer on Cd_3As_2. This dielectric layer is key in transforming Cd_3As_2 into the channel material of a metal-oxide-semiconductor field-effect transistor (MOSFET).

Despite its promise, by mid-2021, controlling the carrier concentrations of (001) Cd_3As_2 films by electrostatic gating still presented a considerable technical issue, limiting access to low-energy physics. Previous work had demonstrated the modulation of *n*-type carriers in (001) films with the AlO_x gate dielectric [56], but was unable to reach a majority *p*-type transport regime, even at highly negative gate voltages. The transition from *n*- to *p*-type behavior would provide clear evidence for a gapped (or semimetallic) band structure in thin Cd_3As_2 films. Resolving potential gapped phases, in particular, is required to establish the topological nature of the film.

The default hypothesis to explain the limited gate performance involves the existence of a high density of impurities or trap states at the interface between the device channel and the ALD-grown dielectric. A breakthrough in addressing this limitation came from

changes in two areas: the introduction of a capping layer for Cd_3As_2 and the additional treatment of the capped surface using a low-power oxygen plasma. Although both technologies existed independently, their combination proved to be even more effective than thought. As mentioned earlier, although just ~3 nm thin, the GaSb capping layer is essential in shielding the surface of Cd_3As_2 from atmospheric and humidity exposure, especially during cleanroom processing [57]. With the addition of the capping layer, the interface hypothesis was tested by a direct oxygen plasma exposure, which is a standard cleaning routine, immediately before the ALD process.

Apart from impurity removal, it is also speculated that the low-energy plasma plays a role in enhancing the growth of AlO_x by ALD, a well-established industrial process [58]. Specifically, the plasma likely helps to stabilize hydroxyl (OH^-) groups on the capped surface, promoting the first reaction step that involves chemisorption of trimethylaluminum [$Al(CH_3)_3$ or TMA]. Excess TMA and the reaction product of methane (CH_4) are then removed from the system, followed by the introduction of water vapor, which completes the second step of the ALD cycle. Plasma treatment experiments on Cd_3As_2 samples were done using a Technics PEII-A system in the UCSB Nanofab. To avoid etch damage of Cd_3As_2, these plasma treatments required a lower power, approximately 30 W to 35 W, compared to the 100 W more commonly used. The exposure time was also limited to between 30 s and 60 s, which is kept short to avoid thermal damage to the sample.

3.2 Preliminary results and challenges

The procedure described above yielded promising early results in terms of gate performance, which can be seen in Figure 3.1. This low-temperature transport data was acquired from a gated Hall bar fabricated following the procedure summarized in Chapter 2. It was made on a capped 20 nm Cd_3As_2 film, grown on an early generation (not lattice-matched) buffer of $Al_{0.9}Ga_{0.1}Sb$, which additionally included a thin layer of InAs between the Cd_3As_2 and the buffer [59].

Figure 3.1 serves to illustrate the basic transport properties of the sample that will be closely examined in this chapter. By applying a negative DC voltage to the top gate relative to the drain contact, the Hall carrier density n(Hall) in this as-grown n-type Cd_3As_2 film could be depleted by more than half, from 7.29×10^{11} cm^{-2} to 2.99×10^{11} cm^{-2}, within just a 1 V range. In this dissertation, the convention is such that, under positive magnetic fields (+B), electrons are characterized by a negative slope in the Hall resistivity ρ_{xy}, while holes have a positive slope. Furthermore, the 2D (sheet) carrier densities determined from ρ_{xy} at low fields ($|B| < 0.5$ T) are in close agreement with n(SdH), the values determined from analyzing minima in the Shubnikov–de Haas (SdH) oscillations of the longitudinal resistivity ρ_{xx}, using a form of Equation 1.7:

$$\nu = n_{\mathrm{SdH}} \cdot \left(\frac{h}{2e}\right) \cdot \left(\frac{1}{B}\right). \tag{3.1}$$

In this case, n(SdH) is determined by the slope from a linear fit of a ν versus $1/B$ plot. The close agreement between n(SdH) and n(Hall) at the three gate voltages suggests that

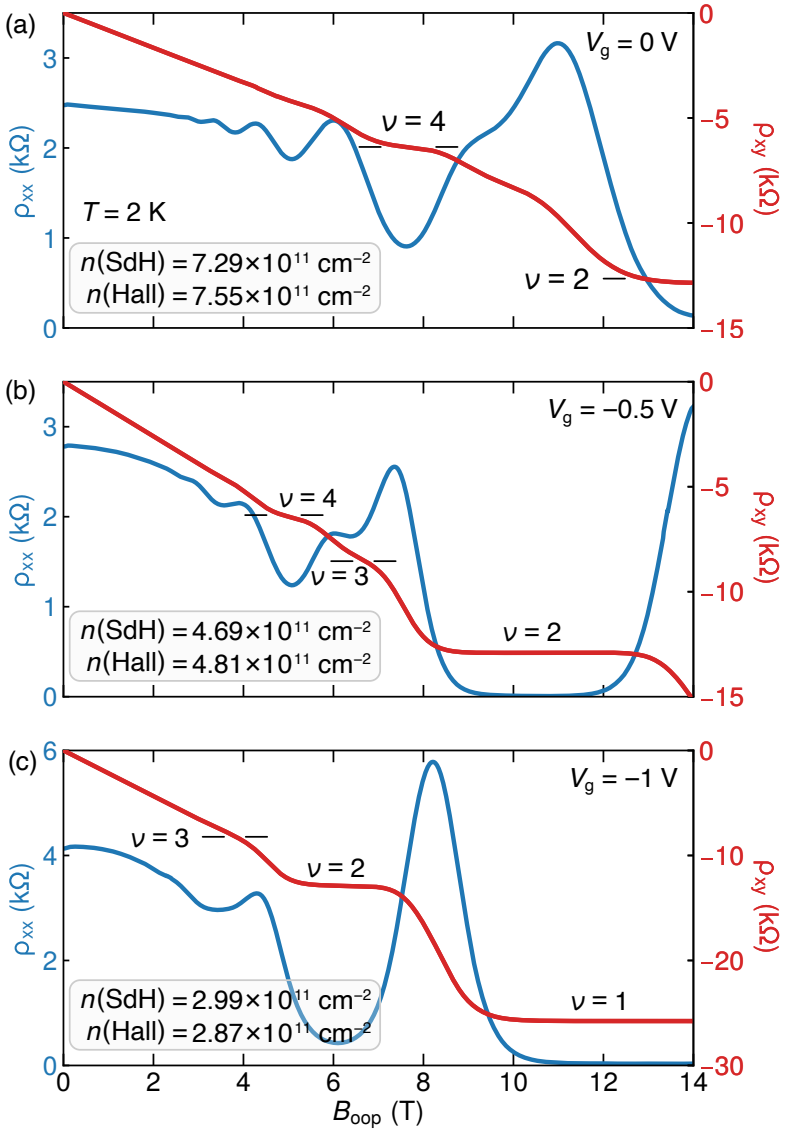

Figure 3.1: Gate voltage dependence of n-type transport in a 20 nm Cd_3As_2 film grown on an InAs/$Al_{0.9}Ga_{0.1}Sb$ buffer, from [13]. (a)-(c) Longitudinal resistivity ρ_{xx} and Hall resistivity ρ_{xy} as a function of the out-of-plane magnetic field B_{oop} at fixed gate voltages of 0 V, −0.5 V, and −1 V, respectively. Negative gate voltages were applied relative to the current drain contact and effectively depleted carriers in the channel. Carrier densities extracted by two methods are indicated.

all carriers involved in electrical transport reside in a 2D state. In addition, the zero-field resistivity can be used to calculate an average Hall mobility $\sim 5000\,\mathrm{cm^2\,V^{-1}\,s^{-1}}$. Other features of data in Figure 3.1, including the integer QHE, will be discussed in later sections.

An alternative approach to measure the gated sample, compared to the method just shown, would be maintaining a constant magnetic field while continuously varying the gate voltage. This approach, involving gate sweeps, introduced unique challenges to the transport measurement setup, thereby motivating the adoption of more reliable transport methods discussed next.

3.2.1 Self-heating effect

Although resistance measurements for Cd_3As_2 are typically straightforward, they can be simultaneously demanding, as the device under test can exhibit a remarkable range of variation, spanning many orders of magnitude. This is most evident in scenarios like transport in the integer quantum Hall regime, where bulk resistivity measurements yield either zero (when the chemical potential lies in a gap between Landau levels) or local maxima (when it resides within a Landau level). However, the most notable challenge in early cryogenic temperature measurements of Cd_3As_2 was found to be accidental sample self-heating. This issue was unexpectedly severe, particularly in initial experiments performing gate sweeps that attempted to reach the band gap or charge neutrality region.

Figure 3.2 presents a comparison of $\rho_{xx}(V_g)$ traces for the same 20 nm Cd_3As_2 film shown earlier, but under two different bias currents: 500 nA in panel (a) and 5 nA in panel

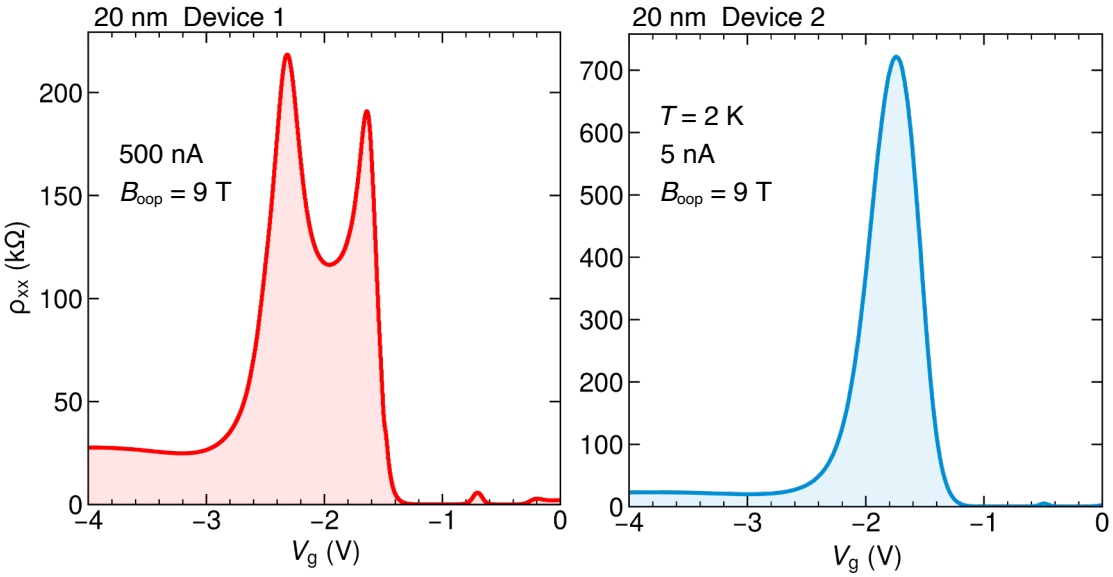

Figure 3.2: Transport near charge neutrality in a 20 nm Cd_3As_2 sample. (a) $\rho_{xx}(V_g)$ for Device 1. This device was current-biased with a 500 nA RMS excitation. (b) $\rho_{xx}(V_g)$ for Device 2. This was an identical device made on the same film, but the measurement was performed with a reduced current bias of 5 nA RMS [13]. The out-of-plane magnetic field was 9 T and the cryostat temperature was 2 K for both measurements.

(b). Both traces were obtained at a fixed out-of-plane magnetic field of 9 T. Using 5 nA, the increasingly negative V_g moves the chemical potential to the charge neutrality condition, resulting in an expected and observed single peak in ρ_{xx}. This behavior aligns with a gapped energy spectrum in the confined Cd_3As_2 film, suggesting effective gate action. However, the very first measurement conducted at 500 nA presented an unexpected valley in place of a peak, with the resistivity in the valley being nearly a factor of 3 lower than the peak observed with 5 nA of current. This phenomenon in fact mirrors the behavior seen for early generations of graphene devices supported by SiO_2, which was discovered to be a consequence of significant Joule heating (refer to Figure 7 in [60] for a comparison).

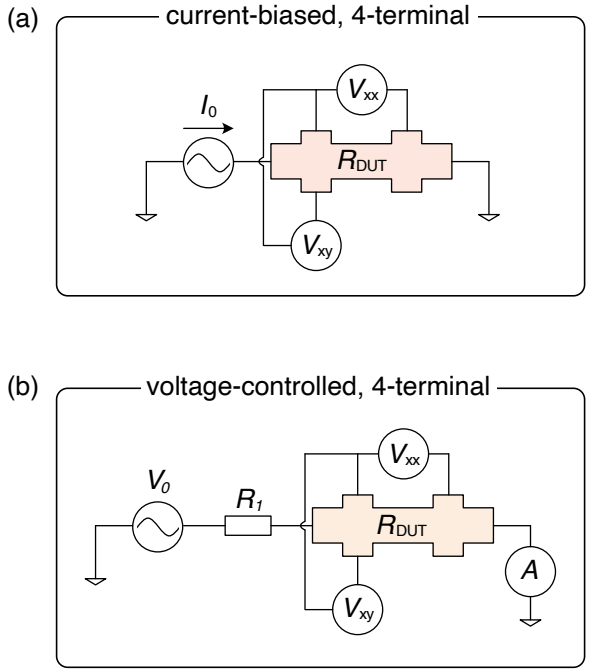

Figure 3.3: Two measurement circuits for a Hall bar. (a) The source-drain current (I_0) is kept constant, while the longitudinal (V_{xx}) and transverse (V_{xy}) voltages are measured by lock-in amplifiers. This circuit is recommended for measuring highly conductive regimes. (b) The applied voltage (V_0) is kept constant and R_{DUT} is in series with a load resistor of a known value (R_1). The source-drain current is measured by a separate lock-in amplifier.

This dependence of the peak behavior at charge neutrality on the current bias prompted a closer look at the measurement circuit in order to minimize unintentional over-biasing. Figure 3.3 illustrates two types of measurement circuits that can be used. The device under test (R_{DUT}) is the multi-terminal Hall bar made on Cd_3As_2. The DC voltage source that applies the gate voltage, present in both circuits, is not depicted for clarity. In the default configuration that resulted in heating, Figure 3.3 (a), a constant AC current is supplied and does not, ideally, vary with the load. However, in an insulating regime, such as when a device is gate-tuned to charge neutrality (or when $R_{DUT} \gtrsim 1\,\mathrm{M\Omega}$), this setup can lead to Joule heating and poor thermalization, potentially opening spurious current paths.

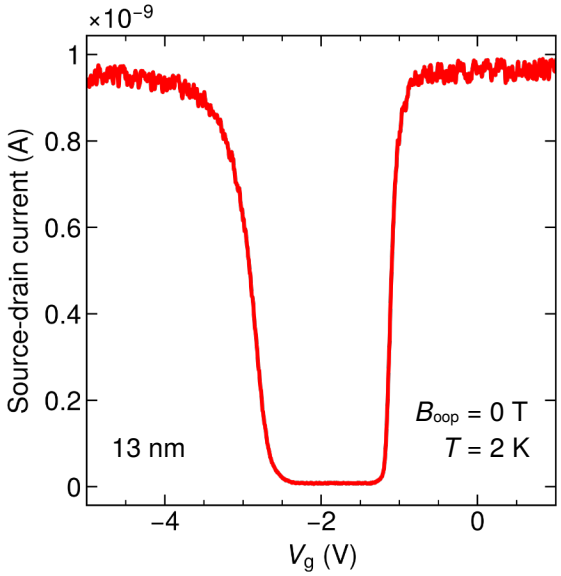

Figure 3.4: Source-drain current as a function of gate voltage for a 13 nm Cd_3As_2 film, measured in a 4-terminal, voltage-controlled configuration. This film has a normal band ordering and a wide, topologically-trivial bandgap. The source-drain current was regulated by a 10 MΩ load resistor so that its value outside the bandgap region is ~1 nA.

An improved setup for measuring both insulating and conducting regimes is shown in Figure 3.3 (b), featuring a load resistor (R_1) that effectively converts an applied AC voltage to current. The maximum current through the sample can furthermore be pre-determined by appropriate choice of R_1. Figure 3.4 demonstrates the advantage of adopting this type of circuit by measuring the transfer curve, or source-drain current as a function of the gate voltage. For this example, a 13 nm Cd_3As_2 film was chosen because it shows the widest insulating region in V_g, a feature that will be elaborated on later. As the chemical potential enters the gap, the film's resistivity sharply increases, leading this circuit to automatically reduce, and even turn off, the current flowing through the channel.

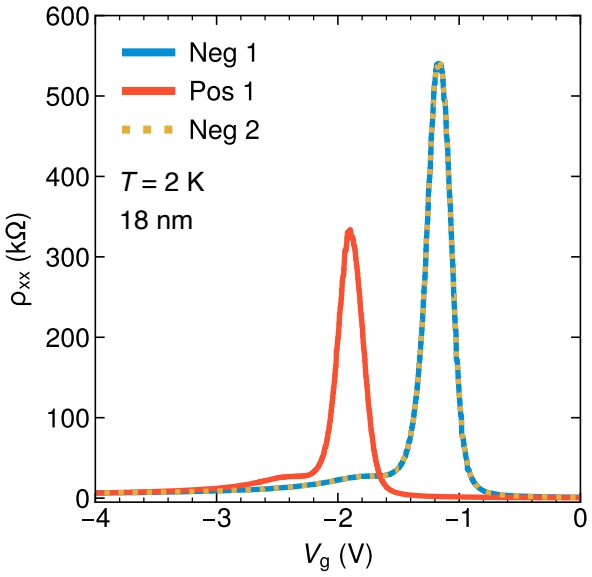

Figure 3.5: Gate hysteresis in $\rho_{xx}(V_g)$ for an 18 nm Cd_3As_2 film at zero field. The blue trace (sweeping to negative V_g) and the red trace (sweeping to positive V_g) demonstrate a shift in the charge neutrality peak position and a change in its magnitude. Successive sweeps in the same direction (blue and yellow traces) show high reproducibility.

3.2.2 Hysteresis effect

Another challenge encountered in gating studies was hysteresis in $\rho_{xx}(V_g)$ traces, depending on the V_g sweep direction, as shown for example in Figure 3.5. This observation suggested residual charged defects were present, either at the gate dielectric and Cd_3As_2 interface or within the dielectric layer itself. Part of the potential supplied by V_g is diverted to charging or discharging these defect levels. To enable fair comparison of $\rho_{xx}(V_g)$ under various magnetic fields and temperatures, a consistent approach was adopted to compare only traces acquired in the same sweep direction, which gave highly reproducible results (Figure 3.5).

3.3 $\nu = 0$ Hall state

A better understanding of gating-induced phenomena in Cd_3As_2 enabled subsequent measurements of the 20-nm-thin Cd_3As_2 sample under low temperatures and high magnetic fields, and, demonstrated for the first time, ambi-polar transport in an (001)-oriented quantum well. This section, largely based on [13], provides a brief overview followed by a discussion on the magnetotransport results and interpretations for this sample.

3.3.1 Motivation

A distinctive feature of a two-dimensional Dirac node, when placed in a perpendicular magnetic field (B), is the presence of a zero-energy ($n = 0$) Landau level that is shared by both electrons and holes [61, 62]. In the example of graphene, the four-fold degeneracy of its $n = 0$ LL can be lifted by either valley or spin splitting, leading to the emergence of $\nu = 0$ quantum Hall (QH) states [63, 64, 65, 66]. In contrast, the surfaces of three-dimensional topological insulators (3D TIs) each support a helical, 2D Dirac node, for which there is no spin degree of freedom. The degeneracy of two $n = 0$ Landau levels belonging to the bottom and top surface states of a 3D TI, respectively, can be removed by introducing a potential difference between these surfaces [67, 68, 69, 70, 71, 72]. In exceptionally thin films where the 3D TI surface states are hybridized, two non-degenerate $n = 0$ LLs can also originate from massive Dirac fermions [28, 73]. Consequently, a $\nu = 0$ QH state can appear in both scenarios associated with the 3D TI when the chemical potential μ is in the

gap between two $n = 0$ Landau levels. These two QH states can, however, be distinguished under a large B-field. In an ideal 3D TI, $n = 0$ LLs remain non-dispersive or constant in B due to equal electron-hole occupation. In contrast, the LLs of a hybridized 3D TI exhibit either electron or hole characteristics, leading to B-dependent energies.

Recent findings in (001) Cd_3As_2 have shown possible evidence for a $n = 0$ LL in quantum capacitance measurements of relatively thick, ~40 nm films, which appeared nearly dispersion-less [74]. This could be interpreted as originating from a 2D Dirac node of the topological surface state, which would suggest that thick (001) Cd_3As_2 films behave like 3D TIs [56]. Confirming a non-dispersive $n = 0$ LL with other forms of direct evidence, such as a $\nu = 0$ quantum Hall state by transport techniques, would reinforce this hypothesis but such measurements are still missing.

3.3.2 Experimental results

Figure 3.6 reports the main findings of this study, once again demonstrating the gate-tunability of the 20 nm sample across the charge neutrality condition. Figures 3.6 (a) and (b) presents the Hall resistivity, ρ_{xy}, and the simultaneously acquired longitudinal resistivity, ρ_{xx} , respectively, as a function of V_g between 1 V and −4 V and magnetic fields between 0 T and 9 T. For $V_g > -2$ V, well-developed electron-like QH plateaus are present in ρ_{xy} and, concurrently, $\rho_{xx} \to 0$. This can be more easily seen in the magnified view of ρ_{xx} at lower magnitudes, as shown in Figure 3.6 (c). For this region, QH plateaus occurring at both even and odd filling factors already point to the lifting of spin degeneracy in the

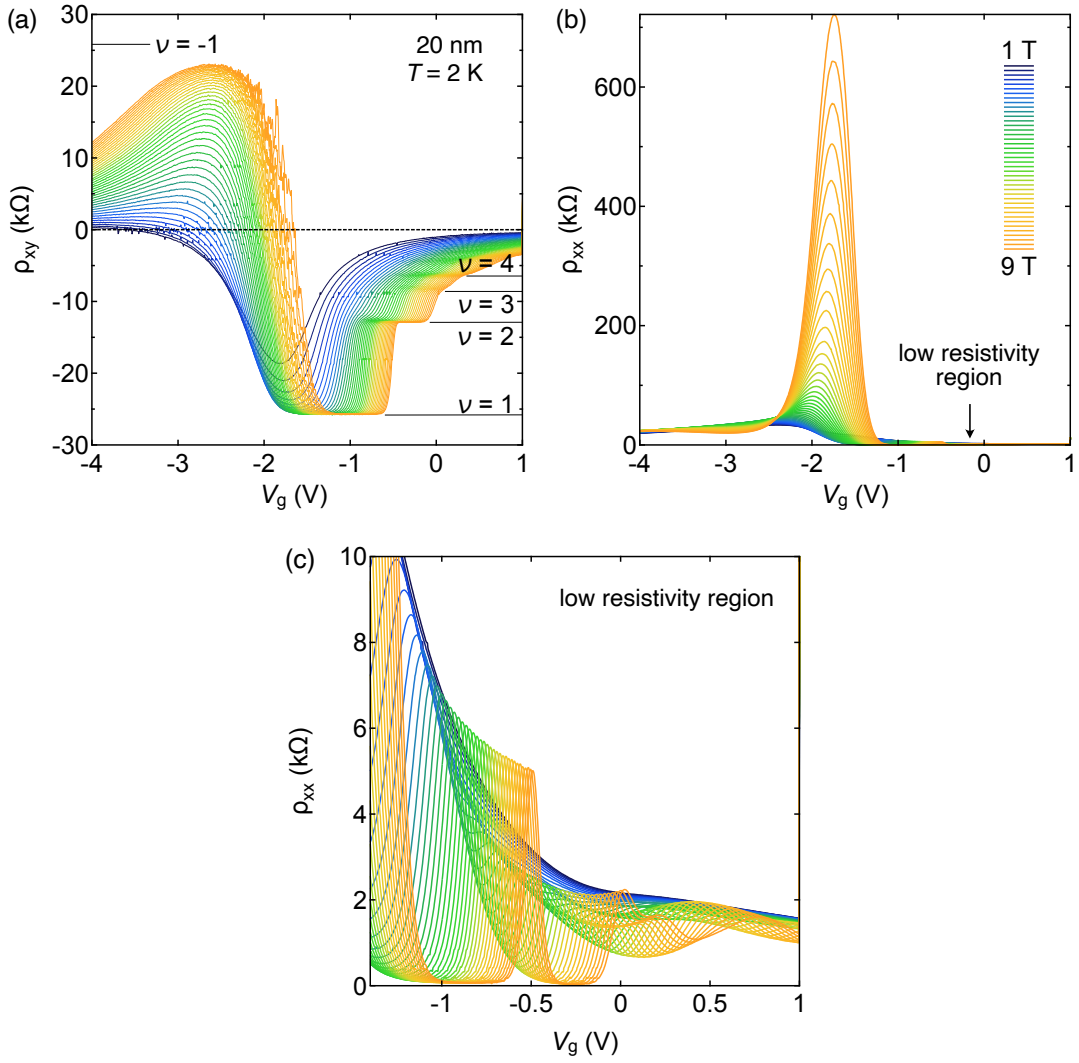

Figure 3.6: Magnetic field dependence of gate sweeps in a 20 nm Cd_3As_2 thin film, from [13]. (a) Hall resistivity ρ_{xy} and (b) the accompanying longitudinal resistivity ρ_{xx} as a function of V_g for B-fields of up to 9 T (step size 0.2 T). Integer quantum Hall plateaus are labelled by their filling factor, while the hole-like $\nu = -1$ plateau is approached, but not reached. (c) Magnified view of ρ_{xx} between V_g of -1.5 V and 1 V.

system. When $V_g < -2\,V$, σ_{xy} approaches hole-like plateaus corresponding to $\nu = -1$, but the values do not quite reach the resistance quantum (h/e^2) at $B = 9$ T, the maximum field applied.

This study will primarily focus on the region around charge neutrality, corresponding to $V_g \approx -2\,V$. At B-fields greater than 3 T, ρ_{xy} evolves smoothly with V_g while crossing through the charge neutrality point at zero, while ρ_{xx} develops a peak that increases in magnitude with increasing B-field. The peak position also shifts to more positive V_g at higher magnetic fields. Further insight can also be gained by converting the resistivity data into conductivity. The two are related by tensor transformation, so the conductivity components can be expressed as:

$$\sigma_{xx} = \frac{\rho_{xx}}{\rho_{xx}^2 + \rho_{xy}^2} \quad \text{and} \quad \sigma_{xy} = \frac{-\rho_{xy}}{\rho_{xx}^2 + \rho_{xy}^2} \tag{3.2}$$

Figure 3.7 presents the conductivity data, with the most prominent feature being the presence of a $\nu = 0$ plateau in σ_{xy}. At the transition from the lowest $\nu = 1$ plateau to $\nu = 0$, σ_{xx} reaches the universal value of $0.5e^2/h$ [75]. In order to demonstrate the widening of the $\nu = 0$ plateau with field, plotting σ_{xx} in the parameter space of B-V_g becomes more effective, which is shown in Figure 3.8 (a). In such a conductivity map, the $\nu = 0$ plateau is represented by a lighter color, flanked by darker regions on both sides. A similar conductivity map for the n-type regime is shown in Figure 3.8 (b). An interesting observation is the skipping of certain QH plateaus, such as $\nu = 4, 5$, which will be explained later.

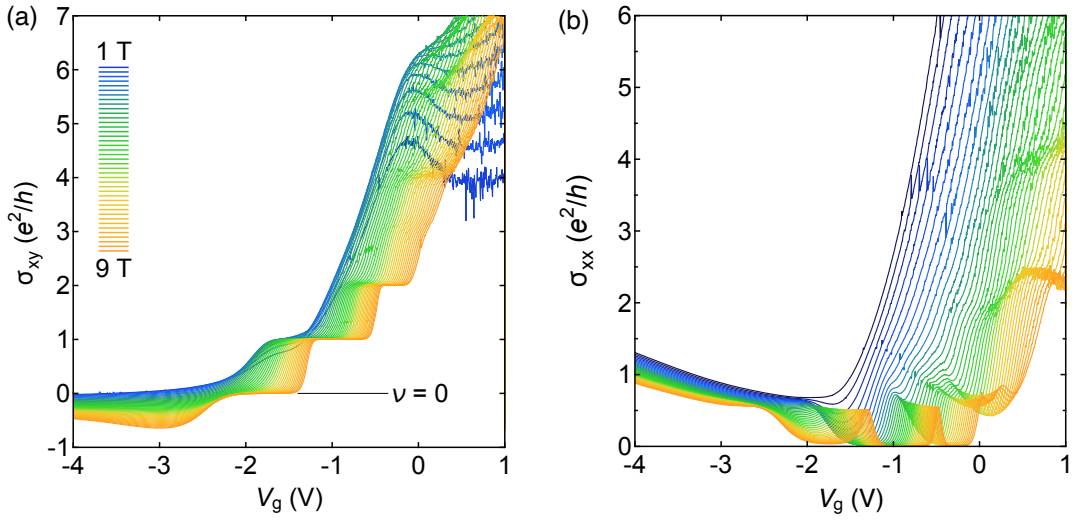

Figure 3.7: Same data as in Figure 3.6, but converted to conductivity. From [13]. (a) Hall conductivity σ_{xy} and (b) longitudinal conductivity σ_{xx} as a function of V_g for B-fields up to 9 T (step size 0.2 T).

Under high magnetic fields, because the $\nu = 0$ state becomes increasingly resistive [as shown in Figure 3.6 (b)], voltage-biased measurements became necessary. Figure 3.9 shows the results and a schematic of the measurement circuit. This type of 2-terminal measurement relies on a simple voltage divider circuit. When the chemical potential reaches the charge neutrality region, leading to extremely large resistances, all of the current will be re-directed through the less resistive branch of the circuit, and no current will flow through the device. This effectively stops self-heating. The directly measured quantity is the conductance G, which inevitably includes the contact resistance. From the offset of the $\nu = 1$ quantum Hall plateaus in Figure 3.9, the contact resistance (per edge channel) is estimated to be ~1.3 kΩ. At $B = 14$ T, G indeed becomes nearly indistinguishable from zero, which is clear evidence for a highly insulating state. This zero-conductance state also contrasts

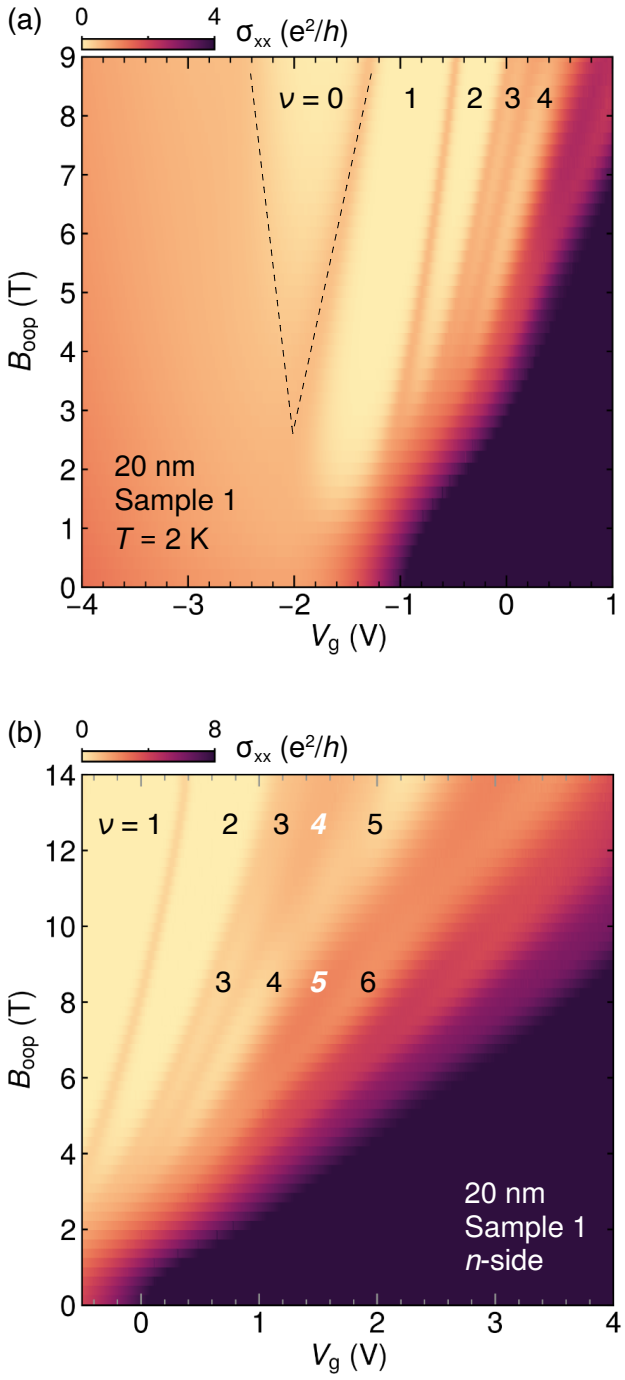

Figure 3.8: Longitudinal conductivity maps as a function of B and V_g for the 20 nm Cd_3As_2 sample. (a) Same data shown in Figure 3.7, from [13], with dashed lines highlighting the widening of the $\nu = 0$ region as B is increased. (b) Conductivity map focusing on only the n-side region and up to $B = 14$ T. The skipped filling factors are labeled in white.

with previous results on 3D TIs, which show finite longitudinal conductivity at charge neutrality [68, 69, 76].

Furthermore, the temperature dependence of the insulating $\nu = 0$ regime was also examined to estimate the transport gap size. Figure 3.10 shows the behavior of the maximum of R_{2pt} $(= G^{-1})$ at $\nu = 0$ as a function of temperature. R_{2pt} demonstrates thermally activated behavior and a crossover to a region with a stronger temperature-dependence at higher temperatures. It is possible that the crossover in R_{2pt} is a transition from hopping transport to Arrhenius-like behavior when the thermal energy $(k_B T)$ is comparable to the energy gap separating the localized states around the Landau levels. For higher temperatures (>20 K), Arrhenius-type fits to the data were used to extract gap sizes, Δ/k_B, for each B-field, which are 11 K, 25 K, 41 K, and 59 K, respectively.

3.3.3 Discussion

Next, a discussion and some comments on the origin of the observed $\nu = 0$ QH state in this film are presented. As mentioned previously, assuming the 3D TI model holds for thicker Cd_3As_2 films, there are two different scenarios for the lifting of the $n = 0$ LL degeneracy in the present 20 nm sample: (1) a 3D TI with surfaces extrinsically offset in energy, creating an energy difference between the $n = 0$ LLs [56, 67, 68, 77]. (2) a modified 3D TI with hybridized surface states, such that there is no longer a distinction between bulk and surface. To experimentally distinguish between these two instances requires examining the energy spectrum near charge neutral conditions.

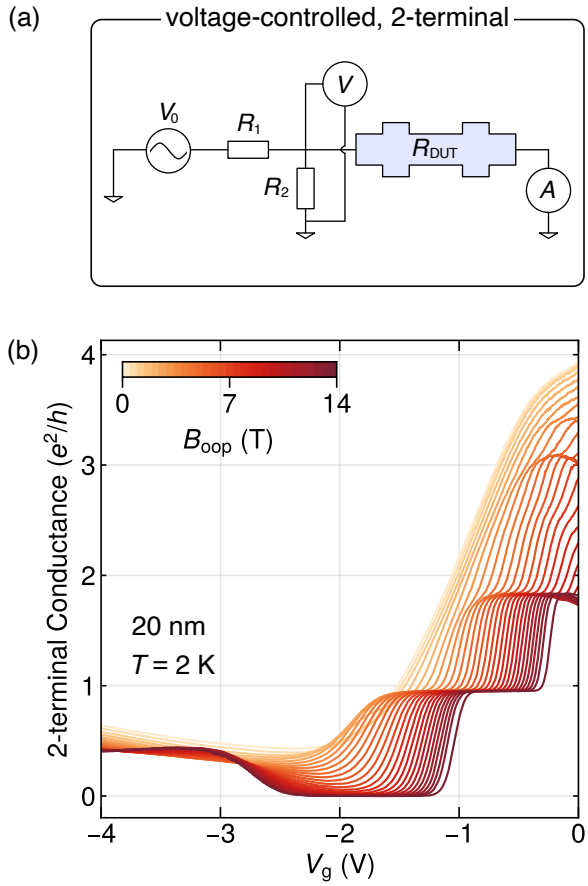

Figure 3.9: Voltage-controlled measurements of the 20 nm Cd_3As_2 film. (a) Schematic of the measurement circuit. With V_0 held constant, R_{DUT} is part of a voltage-divider circuit formed by resistors R_1 and R_2. (b) 2-terminal conductance measurements $G(V_g)$ as a function of B up to 14 T (step size 0.2 T), from [13]. At $\nu = 0$, the conductance is exactly zero with no additional features.

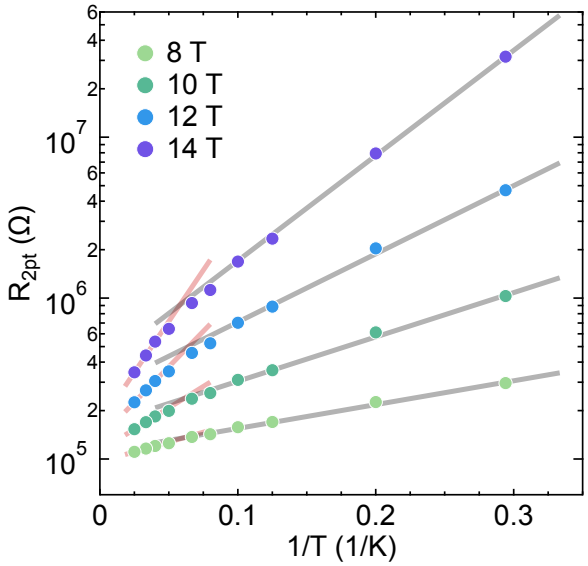

Figure 3.10: Temperature dependence of R_{2pt} at $\nu = 0$, from [13]. T ranges from 3.4 K to 40 K for B-field values of 8 T, 10 T, 12 T, and 14 T. Two regimes of transport behavior are evident with a crossover at ~20 K. In each regime, lines are fits to Arrhenius-type activation gaps.

Figure 3.8 indicates that a constant spacing between the $n = 0$ LLs, independent of the strength of the B-field, is clearly not observed. For the sample in question, this eliminates the possibility of a 3D TI scenario with massless 2D Dirac surface states at different potentials. Instead, the $\nu = 0$ plateau opens up with increasing field, a consequence of the two $n = 0$ Landau levels dispersing in B. Put differently, one of these LLs is hole-like and the other is electron-like. In the 3D TI picture, these results are therefore more consistent with the behavior of massive Dirac fermions that form from the overlap of surface state wave functions, i.e., hybridization, in a quantum well of Cd_3As_2.

The fact that ρ_{xx} is not very high at low B [$\rho_{xx}(B = 0) \sim 1.2h/e^2$] indicates that the band gap is likely small in Cd_3As_2 grown on this buffer, and potentially obscured by

electron–hole puddles. A theoretical estimate for the confinement-induced band gap, using calculated band parameters for Cd_3As_2 , is ~5 meV for a 20 nm film [11]. A more accurate estimate of the gap and the behavior of the quantum well subbands as a function of thickness would require knowledge of band parameters specific to this Cd_3As_2 film embedded in an epitaxial heterostructure (which also induces bi-axial strain in Cd_3As_2 that has not been considered so far).

Returning to the question of surface state hybridization in a 20 nm film, a conservative estimate shows that the hybridization regime is already reached here. The characteristic length of the surface Dirac state varies as $l \propto \hbar v_F/\Delta$ [78], where Δ is the hybridization gap and v_F is the Fermi velocity. Assuming $\Delta = 5$ meV and using a lower bound for v_F of 1.5×10^6 m/s, l becomes close to 20 nm. It is therefore reasonable to expect hybridization in the present sample. Higher surface state Fermi velocities can lead to hybridization at even greater thicknesses in Cd_3As_2. Additionally, it should be noted that the model of a hybridized 3D TI, with massive Dirac fermions, and the model of a quantum well, with discrete subbands, transition into each other in the 2D limit [11, 28].

Finally, it is important to recognize that quantum-confined (001)-oriented Cd_3As_2 films may be either 2D TIs or trivial insulators, based on the ordering of the electron- and hole-like subbands. Unfortunately, the sample here does not provide the means to determine if the subband states responsible for the dispersing $n = 0$ LLs are inverted at $B = 0$.

3.4 Band-inverted regime

To conclusively determine the subband ordering in Cd_3As_2 quantum wells, a new series of films was necessary. These films, grown using a nearly lattice-matched $Al_{0.45}In_{0.55}Sb$ buffer [20] as detailed in Chapter 2, showed significant improvement in materials quality. Most notably, they displayed Hall mobilities nearly five times higher than those with similar electron concentrations on the $InAs/Al_{0.9}Ga_{0.1}Sb$ buffer (see Figure 3.1).

Figure 3.11 shows an example 18 nm Cd_3As_2 quantum well with an $Al_{0.45}In_{0.55}Sb$ barrier, which also exhibits enhanced quantum mobility, as judged using the $\omega_c\tau_q > 1$ criterion, reaching a value as high as $10\,000\,cm^2\,V^{-1}\,s^{-1}$. Since Cd_3As_2 layers grown on $Al_{0.45}In_{0.55}Sb$ experience less bi-axial compressive strain at room temperature, compared to ones grown on buffer layers strained to GaSb, they are more closely aligned with the quantum well model introduced in Chapter 1. The consistency with the quantum well model is discussed in [14], which provides a clearer theoretical framework for further studies.

Although the precise band alignments between Cd_3As_2 and the III-Sb layers are not yet known, the improvement in electron mobility for nearly identical Cd_3As_2 films (in terms of thickness, carrier concentration), invites some speculation. In near-surface quantum wells, such as the Cd_3As_2 samples studied here, dominant sources of scattering are likely the interface roughness and the presence of ionized impurities on the top surface. The $Al_{0.45}In_{0.55}Sb$ buffer potentially addresses these issues by setting up a greater conduction band offset with Cd_3As_2, consequently shifting the wave functions of Cd_3As_2 away from

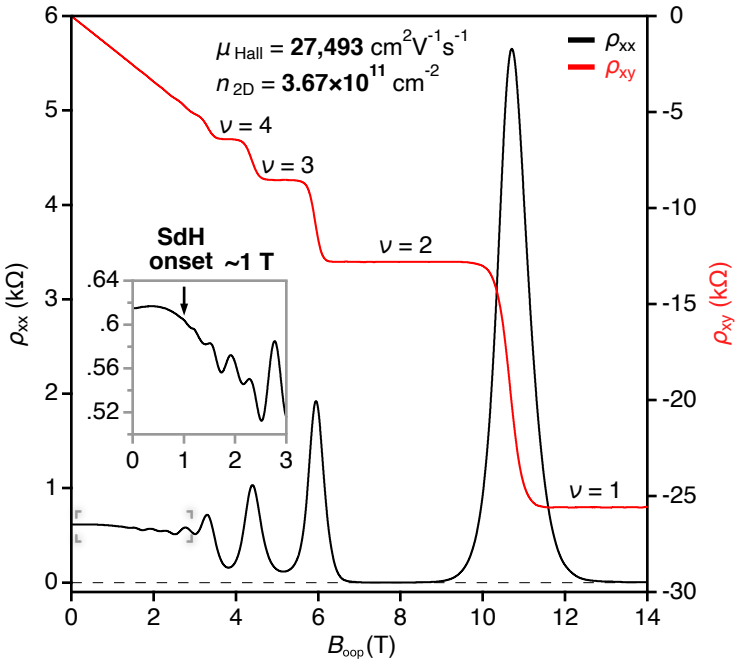

Figure 3.11: Magnetotransport in an 18 nm (001) Cd_3As_2 quantum well grown on $Al_{0.45}In_{0.55}Sb$. This film was measured with $V_g = 0$ V and at $T = 2$ K.

the top interface. The reduced disorder in these new samples can be qualitatively assessed by the quantum scattering time τ_q. Disorder-induced broadening of LLs is typically estimated by Γ, an energy spread that is inversely related to τ_q using the expression:

$$\Gamma = \frac{\hbar}{\tau_q}. \tag{3.3}$$

On the nearly lattice-matched buffer, the lower degree of disorder is evident in Figure 3.12, which presents maps of the LL spectrum for a Cd_3As_2 thickness series [14]. Along the V_g axis, which is proportional to the system's energy scale, the LLs from the electron-like subbands appear much sharper than before. But more importantly, the conductivity maps in Figure 3.12 clearly demonstrate the intersection of two $n = 0$ LLs under a magnetic field, one emerging from an electron-like subband and the other from a hole-like subband. This

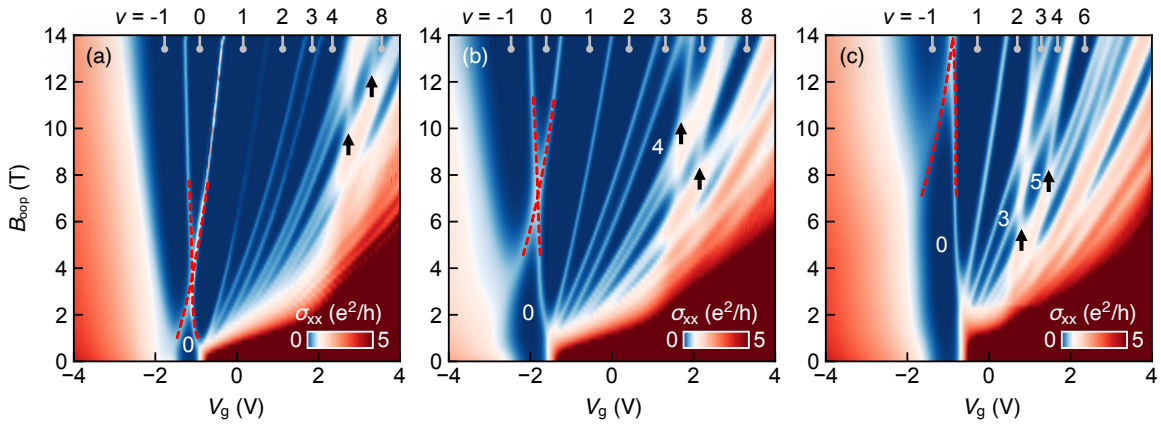

Figure 3.12: Thickness dependence of inverted subbands in (001) Cd_3As_2 quantum wells grown on $Al_{0.45}In_{0.55}Sb$, from [14]. (a)-(c) shows longitudinal conductivity maps acquired for films with increasing thicknesses of 18 nm, 19 nm, and 22 nm, respectively. Arrows point to LLs emerging from a second electron-like subband, consistent with the quantum well model. The second subband was also seen in Figure 3.8, but was obscured by disorder.

firmly establishes the inverted band structure of Cd_3As_2 quantum wells in the thickness range of ~18 nm to 22 nm, which can now be classified as 2D TIs.

Chapter 4

Transport under a Zeeman field

This chapter, largely based on [15], examines how an in-plane (Zeeman) magnetic field affects the transport properties of Cd_3As_2 quantum wells that belong to the band-inverted regime. The evidence presented here supports a topological phase transition from the inverted, 2D TI phase to an emergent 2D Weyl semimetal phase (2D WSM). This gapless phase is predicted to host a pair of Weyl nodes of opposite chirality at charge neutrality that are protected by space-time inversion (C_2T) symmetry. Unique transport signatures are demonstrated, including saturated resistivities on the order of h/e^2 that persist over a range of in-plane magnetic fields. Furthermore, subjecting the 2D WSM phase to a small out-of-plane magnetic field gives rise to an odd-integer QH effect, characteristic of degenerate, massive Weyl fermions. These findings can be qualitatively explained using a four-band $\boldsymbol{k}\cdot\boldsymbol{p}$ model of Cd_3As_2 that incorporates first-principles effective g factors.

4.1 Background and motivation

Two-dimensional, topologically non-trivial states of matter are notable for the ease with which they can be manipulated, either by external electric and/or magnetic fields, epitaxial strain, or proximity effects. Compared to their three-dimensional counterparts, the increased level of control over these materials provides an advantage for experimental research. One significant example is the quantum spin Hall insulator, or 2D topological insulator (2D TI), which can be characterized by helical edge modes that exist within a bulk energy gap under time-reversal symmetry [3, 4].

Subjecting a 2D TI to in-plane magnetization, the focus of this chapter, is expected to give rise to a rich array of electronic states. Potential candidates include quantum anomalous Hall insulators [79, 80, 81, 82], density-wave phases [83], as well as 2D (topological) semimetals [80, 81, 84]. While there exists a significant body of literature studying 2D TIs in out-of-plane magnetic fields (see, e.g., [85, 86] and references cited therein), in-plane magnetization-induced phases have only recently been investigated [87, 88, 89]. Consequently, the underlying nature of the induced phases and the transitions between them are less understood.

Inducing an in-plane magnetization can be approached in two ways: intrinsically, through the use of magnetic dopants, or directly via an external magnetic field B_{ip} oriented within the plane of the 2D system. The latter approach has the advantages of tunability and applicability beyond intrinsically magnetic materials, which typically require controlling

impurity concentrations and magnetic interactions. The primary effect of B_{ip} is to modify the energy levels of a 2D electronic system via Zeeman coupling:

$$\Delta E_Z \sim g\mu_B B_{ip} \tag{4.1}$$

where the g factor is sample and material specific, and μ_B is the Bohr magneton.

Interestingly, most 2D TIs realized experimentally so far tend to be narrow bandgap semiconductors. In such systems, the presence of an in-plane Zeeman field can strongly modify the Fermi surface topology. A few theoretical studies [80, 84, 90, 91] have shown that B_{ip} can close the topological gap observed at zero-field in a 2D TI, potentially driving the system into a metallic state when the hole-like and electron-like subbands overlap in momentum space. However, the topological classification of the anticipated (semi-) metallic phase is still unclear, in both experimental and theoretical contexts. An early study using band-inverted HgTe quantum wells indicated that the resulting phase behaves like a conventional metal, which was based on observing a reduction in the local (and non-local) resistances in the diffusive transport regime [87].

4.2 Symmetry and theoretical considerations

The subsequent sections of this chapter will explore the evolution of the 2D TI phase of Cd_3As_2 quantum wells [14] under in-plane and tilted magnetic fields. As a starting point, crucial insights can be obtained from symmetry arguments for the 2D TI phase of Cd_3As_2. In the absence of a magnetic field, these band-inverted films possess $4/mmm$ point group and time reversal (T) symmetries [11, 38]. Under an in-plane magnetic field, the symmetry

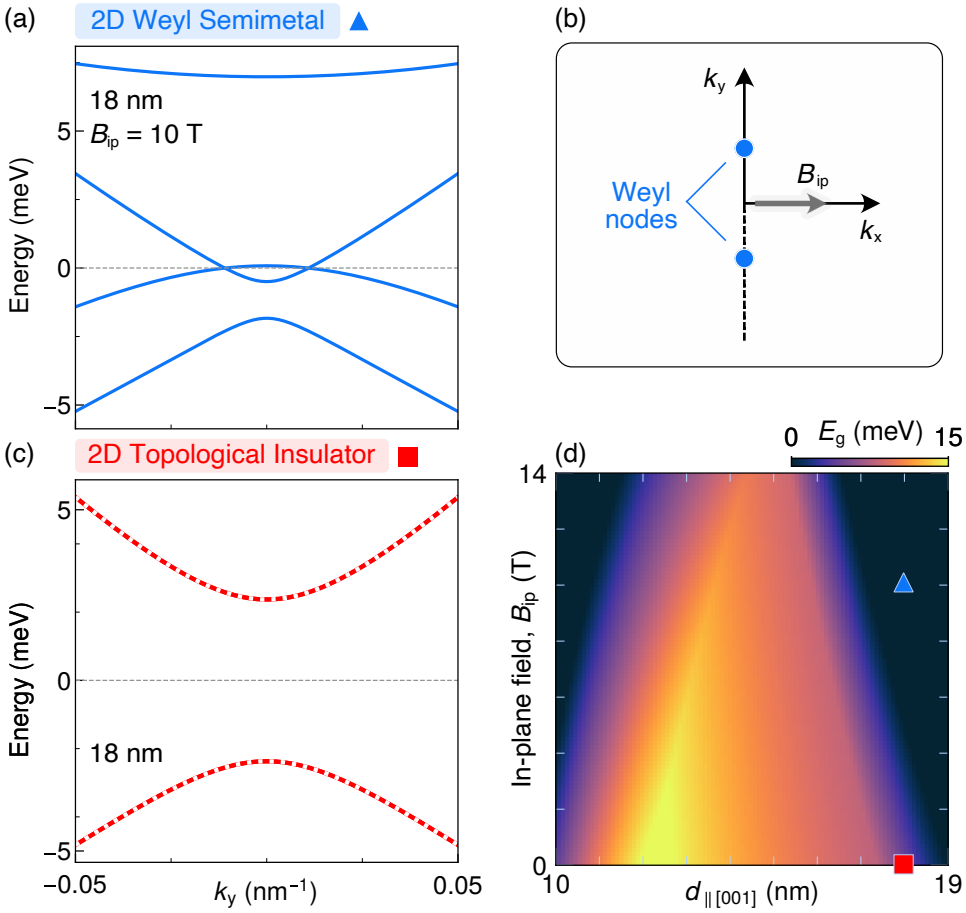

Figure 4.1: 2D Weyl semimetal phase induced by a Zeeman field in quantum confined (001) Cd_3As_2 thin films. (a) Dispersion of the semimetal phase with two Weyl nodes located at charge neutrality (E = 0 meV, dashed line). The 4 bands are spin resolved. In the $\boldsymbol{k}\cdot\boldsymbol{p}$ thin film calculation, Cd_3As_2 has a thickness d = 18 nm along [001] under an in-plane field B_{ip} = 10 T. (b) Schematic of the momentum space locations of the Weyl nodes with respect to the in-plane field direction. (c) Dispersion of the 2D TI phase with no external magnetic field. The spin-degenerate bands are drawn as dashed red lines. (d) Phase diagram of the Γ point energy gap in the B_{ip}-d parameter space. The thickness range corresponds to the band-inverted regime. Blue triangle: 2D WSM. Red square: 2D TI.

reduces to a simple magnetic point group, $2'/m'$, which contains the symmetry operators E, C_2T, M_zT, and inversion (P). As discussed in [92], the presence of C_2T symmetry eliminates one of the three Pauli matrices for the Hamiltonian at any given $\boldsymbol{k}$ point in the 2D Brillouin zone. This can result in a new 2D Weyl semimetal (2D WSM) across a finite phase region when a controllable parameter inverts the bandgap. Here, the strength of the in-plane field serves as that tuning parameter. The significance of C_2T symmetry to the stability of Weyl nodes against perturbations that locally open an energy gap has also been discussed extensively in [93].

This symmetry analysis is further confirmed by computational studies, which were carried out by Wangqian Miao and Prof. Xi Dai. Figure 4.1 (a) shows the dispersion in the E-k_y plane computed for an 18 nm film at B_{ip} = 10 T, which was obtained from the symmetry-invariant $\boldsymbol{k}\cdot\boldsymbol{p}$ Hamiltonian introduced earlier for Cd_3As_2 [11, 94]. The in-plane g factors and other effective model parameters are derived using quasi-degenerate perturbation theory, as outlined in [95, 96], and implemented within a first-principles code, which is detailed in [97, 98]. To obtain an accurate theoretical treatment of the magnitude of B_{ip} effects, the approach used here involves further re-normalizing the bulk g factors of Cd_3As_2 due to quantum confinement. These are already known to be large, with reports of $g_{bulk} > 20$ [99, 100]. The dominating in-plane g factor (g_{1p}) is calculated to be ~ 12 for the bulk and ~ 13 for an 18-nm-thin film. More importantly, the calculation finds an isolated pair of Weyl nodes at charge neutrality, which are split along the direction perpendicular to the applied field, as shown schematically in Figure 4.1 (b).

This result also implies that the low-energy physics of these nodes can be accessed in transport measurements at lab-scale magnetic fields by using electrostatic gating to tune the chemical potential. The degeneracy of the two Weyl nodes is furthermore guaranteed by bulk inversion symmetry present in Cd_3As_2 thin films [6, 37, 38]. Without a Zeeman field, the 18 nm film is a 2D TI, with doubly-degenerate subbands, as shown in Figure 4.1 (c). The detailed calculations also allow the creation of a phase diagram, presented in Figure 4.1 (d), showing the bandgap as a function of the in-plane field strength and the film thickness. The predicted thickness range for the 2D TI phase at zero field is in close agreement with previous experiments [14].

4.3 Measurement setup

Transport measurements were carried out using top-gated Hall bars fabricated from high-mobility (001) Cd_3As_2 films, which were grown by molecular beam epitaxy to thicknesses of 18 nm and 22 nm, respectively, on nearly lattice-matched buffers of $Al_{0.45}In_{0.55}Sb$, supported by (001) GaSb substrates [20]. Both film thicknesses fall within the band-inverted regime [14]. Resistance data were acquired from four-point measurements using low-frequency lock-in techniques and are presented as two-dimensional resistivities or conductivities. Unless stated otherwise, data were recorded at $T = 2$ K. With no gate voltage applied, the 18 nm film had a low-field Hall mobility $\mu_{\mathrm{Hall}} = 2.8\times10^4$ cm^{2}V^{-1}s^{-1} at an electron density $n_{2\mathrm{D}} = 3.6 \times 10^{11}$ cm^{-2}, while the 22 nm film had $\mu_{\mathrm{Hall}} = 1.7 \times 10^4$ cm^{2}V^{-1}s^{-1} at $n_{2\mathrm{D}} = 5.5 \times 10^{11}$ cm^{-2}.

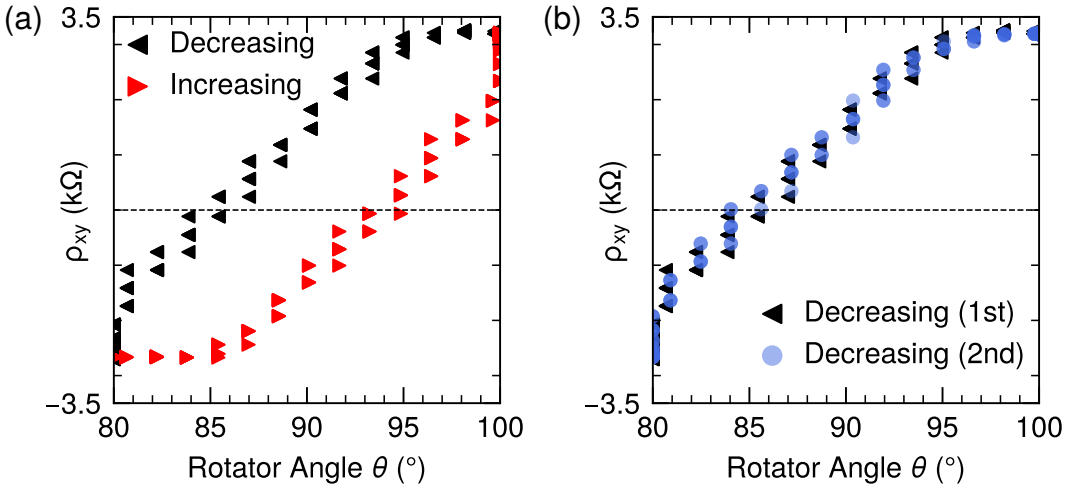

Figure 4.2: Alignment of the in-plane magnetic field. (a) Hall resistivity as a function of rotator index position. The nominally in-plane condition at 90° produces an appreciable Hall signal, which can be zeroed out by decreasing the position to 85.5° (black triangles). This position can then be defined as completely in-plane. Approaching the same index positions from the opposite direction (red triangles) also produces different Hall signals (i.e., backlash). (b) Backlash can be minimized when the approach direction and the approach speed are kept the same. Data were acquired at $T = 2$ K on the 18 nm Cd_3As_2 sample (hb1) with 0 V applied to the gate and a total magnetic field of 14 T.

For in-plane and tilted magnetic field measurements, the samples were attached with varnish to a mechanical rotator stage (Quantum Design Inc.), where a 90° index corresponds to a nominally in-plane position. Because all Cd_3As_2 films studied here were grown on 1.5° miscut GaSb substrates, using the rotator was necessary to minimize alignment errors after mounting. The samples could then be used as a Hall sensor to find the angular index position that corresponded to a zero Hall signal. A completely in-plane field component should not, conventionally, generate a Hall voltage.

An example alignment process is shown in Figure 4.2 (a) using the 18 nm Cd_3As_2 film. While the total magnetic field was set to 14 T (to maximize the Hall signal) and the gate voltage was set to 0 V (to position the chemical potential in an electron-like subband and

not on a quantum Hall plateau), the rotator index was stepped from 100° to 80° and the Hall signal passed through zero at 85.5°, consistent with a misalignment of a few degrees caused by the miscut and mounting error. The signal of a well-aligned sample should drop to zero at an index of 90°. Given a step size of ~ 0.17°, the out-of-plane field error is estimated to be ~ 0.05 T. Figure 4.2 (a) also shows that backlash is significant at $T = 2$ K when approaching the same index from opposite directions. After fixing the approach direction, as shown in Figure 4.2 (b), the Hall signals converge and allow for meaningful angular comparisons. The approach speed is kept at 3 °/min for all measurements. In experiments with an additional out-of-plane field component B_{oop}, the total field B_{tot} was fixed, while the samples were rotated *in situ*. After the calibration procedure described above, the angle θ relative to the sample normal (+z direction) was defined such that $\theta = 90°$ corresponds to the field positioned completely in plane. The fields in other cases are related to each other by $B_{oop} = B_{tot} \cos\theta$ and $B_{ip} = B_{tot} \sin\theta$.

4.4 Out-of-plane and in-plane transport

Before discussing the unusual nature of the in-plane results, an important point of comparison can be made by examining the case with the magnetic field oriented fully out of plane. Figure 4.3 (a) shows the longitudinal conductivity $\sigma_{xx}(B_{oop})$, measured on the 18 nm sample as a function of top-gate voltage. A modified gate voltage scale, $V_g - V_{CNP}$, is used to aid comparison of films with slightly different as-grown carrier densities, where V_{CNP} is the voltage corresponding to a global maximum in $\rho_{xx}(B_{tot} = 0)$. The evolution

of subband LLs, and, in particular, the crossing of the two $n = 0$ LLs, is characteristic of the previously reported subband inversion in Cd_3As_2 [14]. A specific point to note is that spin or "isoparity" degeneracy (when spin is not a conserved quantum number [101]) is lifted at any finite B_{oop} for $n > 0$ LLs in these (001) Cd_3As_2 quantum wells [13, 14], as evidenced by the appearance of completely developed, even and odd integer QH states at the same low $B_{oop} \sim 1.5$ T. This point will be revisited later. Furthermore, from Figure 4.3 (a), a higher-energy conduction subband is visible at 4 V, contributing an additional pair of LLs. Because this subband resides outside the low-energy window of interest for in-plane experiments, i.e., approximately [−2 V, 2 V], it is not discussed in this study.

The same 18 nm device with the magnetic field fully in plane is examined next. Figure 4.3 (b) shows the longitudinal resistivity $\rho_{xx}(B_{ip})$ of the 18 nm sample as a function of gate voltage, which tunes the 2D carrier system from $n-$ to $p-$type transport regimes. Resistivity traces at constant B_{ip} peak around 0 V, but the peak magnitude shows a non-monotonic evolution with increasing B_{ip}: the peak resistivity increases rapidly at low fields, followed by a sharp drop past ~1 T. The 22 nm Cd_3As_2 sample, which lies at the other end of the thickness range for the inverted phase, demonstrates similar behavior, as shown in Figure 4.3 (c). These results for Cd_3As_2 are qualitatively similar to that of inverted (001) HgTe quantum wells at comparable magnitudes of B_{ip} [88]. Representative traces of $\rho_{xx}(V_g - V_{CNP})$ at fixed B_{ip} can be found in the Supplementary Information of [15].

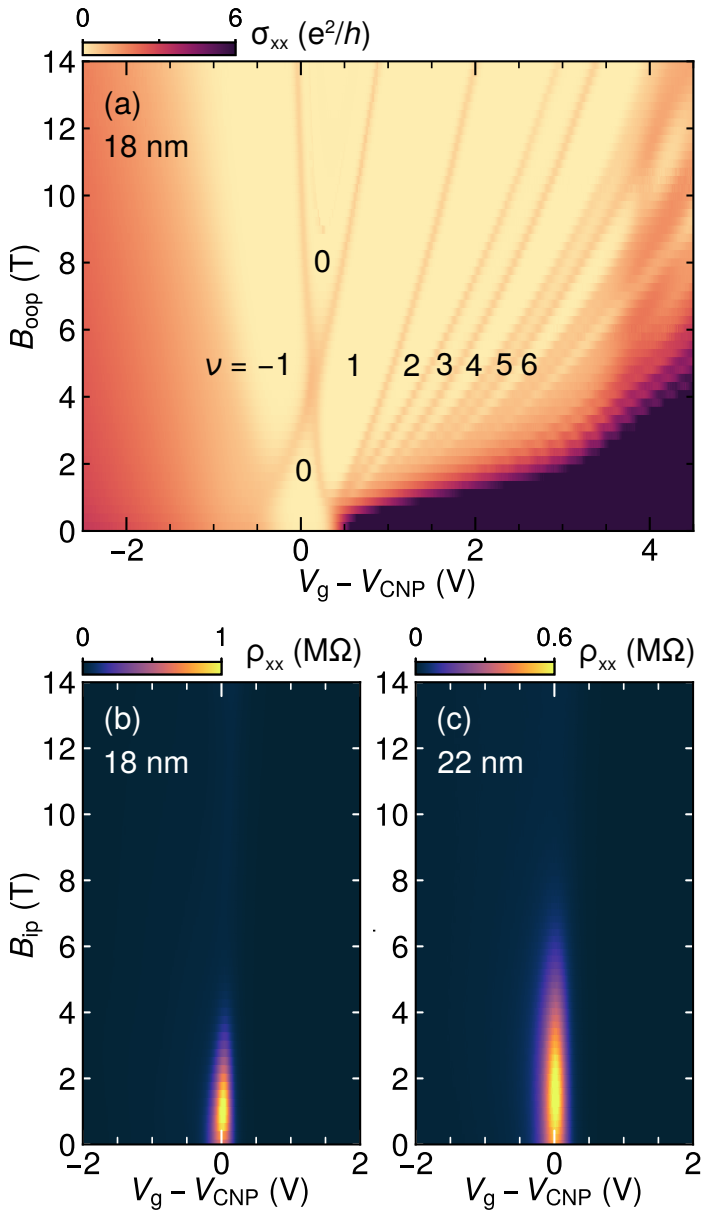

Figure 4.3: Out-of-plane and in-plane magnetotransport in the band-inverted regime. (a) Longitudinal conductivity σ_{xx} as a function of the out-of-plane field B_{oop} and the scaled (relative to V_{CNP}) top-gate voltage for the 18 nm sample (device: hb1). Quantum Hall plateau regions are indexed by their filling factor ν up to 6. V_g is offset by V_{CNP}, which corresponds to the charge neutrality condition defined in the main text. (b) Longitudinal resistivity ρ_{xx} as a function of the in-plane field B_{ip} and the top-gate voltage for the 18 nm Cd_3As_2 sample (device: hb1). The same is shown in (c) for the 22 nm sample. $V_{CNP} = -1.35$ V for the 18 nm sample, $V_{CNP} = -1.165$ V for the 22 nm sample. Measurements were done at $T = 2$ K in the transverse configuration.

Figure 4.4 presents the extracted peak resistivity under B_{ip} from the two inverted samples to clearly visualize the bandgap closing under large Zeeman fields. This analysis interestingly indicates that the transition point, where $d\rho_{xx}/dB_{ip}$ goes to zero, is ~1 T in both samples. Beyond this transition point, the approximate rate of gap closing, using the average slope of $\rho_{xx}(B_{ip})$ from [2 T, 4 T] as a metric, is 1.9 times greater in the 18 nm sample than in the 22 nm sample. The gap is consequently closed at a higher field in the 22 nm sample.

In the gapless region, shown in Figure 4.4 (b), both samples exhibit peak resistivities on the order of the resistance quantum h/e^2, with the 22 nm sample showing slightly lower values just under 0.8 h/e^2. For the 18 nm sample, this implies a > 90% reduction of resistivity as compared to zero-field values, i.e., giant negative magnetoresistance. Additionally, while the 22 nm sample exhibits saturated resistivity [see Figure 4.4 (b)], the 18 nm sample displays additional features. These features, consistently observed across different devices on the same film (hb1 vs. hb2), necessitate further exploration beyond the scope of this current study. It is also notable that a resistivity value near h/e^2 is reasonably close to what is expected for 2D Dirac/Weyl systems [102, 103]. The gap closing and transition to a semimetal phase is further confirmed by the temperature dependence of the resistivities, which are provided in the Supplementary Information of [15]. The relatively wide range of B_{ip}, within which the gapless phase is found, is one of the key experimental results, because it is consistent with the predicted wide stability range of the Zeeman field-induced 2D WSM phase, as discussed earlier.

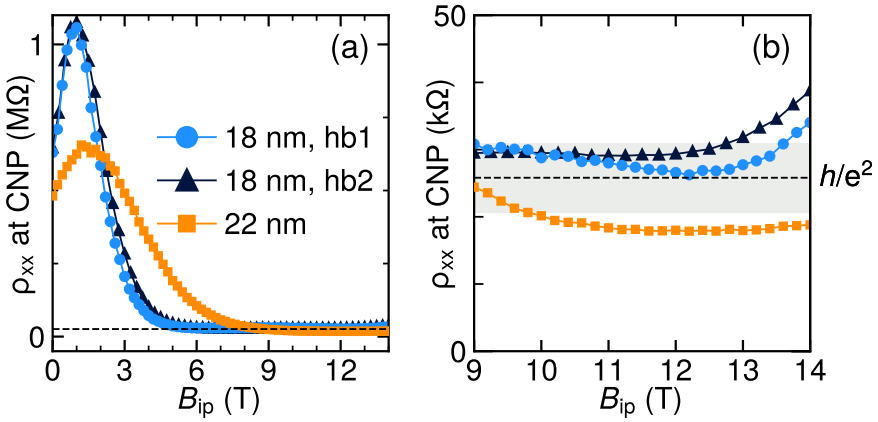

Figure 4.4: Saturated resistivity on the order of h/e^2 in the 2D WSM phase. (a) Extracted ρ_{xx} at the charge neutrality condition as a function of B_{ip} for the 18 nm sample (devices hb1, hb2 are on the same film) and the 22 nm sample. (b) Close-up of the $B_{ip} > 9$ T region for the data in (a). Shading indicates a ± 20% interval around the resistance quantum h/e^2 ≈ 25.81 kΩ (dashed line).

4.5 Tilted field transport

A deeper understanding of the topological nature of the 2D semimetal can be obtained by examining its QH effect under the combined effects of in-plane and out-of-plane magnetic fields. In the present case, these measurements are accomplished by tilting the sample ($\theta < 90°$), while keeping B_{tot} constant. The out-of-plane component of the field will gap the C_2T-symmetric Weyl nodes, thus allowing a QH effect to appear in the 2D WSM phase. For the following analysis, the 18 nm sample is used as an example. It enters the gapless phase at lower B_{ip}, and the V_g range is chosen so that the second conduction subband is not present in this data [see Figure 4.3 (a)]. Figure 4.5 present sets of $\sigma_{xx}(V_g)$ and $\sigma_{xy}(V_g)$ traces, one set for each of four tilt angles, 80°, 75°, 70°, and 65° from panels (a) to (d), at B_{tot} = 14 T. The corresponding B_{oop} values for the respective tilts are 2.43 T, 3.62 T, 4.79

T, and 5.92 T with an uncertainty of ± 0.05 T due to positioning error discussed earlier. B_{ip} is greater than 12.5 T in all four cases so that the sample remains in the B_{ip} range of the gapless phase shown in Figure 4.4 (b).

Two main observations are made regarding the QH effects presented in Figure 4.5. First, the presence of a $\sigma_{xy} = 0$ plateau ($\nu = 0$) in all tilt cases, which connects to $\nu = \pm 1$ plateaus, suggests that the two 0^{th} LLs are spin-resolved. If they weren't, their contribution to the filling factor sequence would be in increments of two or more, accounting for other possible system degeneracies. This is also consistent with their dispersion in B_{oop} up to 5.92 T, which causes the $\sigma_{xy} = 0$ plateau to continuously widen on the V_g scale. This behavior in the gapless phase can be further compared to the LL spectrum with purely B_{oop}, shown earlier in Figure 4.3 (a), where the $\sigma_{xy} = 0$ plateau in that case narrows down until it vanishes below 5 T when the two 0^{th} LLs meet.

Second, the LLs with $n \geq 1$ give rise to an odd integer sequence of filling factors. At $B_{oop} \leq 3.62$ T, as shown in Figures 4.5 (a) and (b), in addition to $\nu = \pm 1$, σ_{xy} plateaus at $\nu =$ 3, 5, and 7 are most prominent, but additional minima in $\sigma_{xx}(V_g)$ appear at electron densities corresponding to $\nu = 9$ and $\nu = 11$. Therefore, the LLs are 2-fold degenerate when B_{oop} is small, in remarkable contrast to the findings when there is no in-plane field, as shown in Figure 4.3 (a). Together with the spin-resolved 0^{th} LLs discussed earlier, this odd-integer-only sequence suggests the existence of a pair of massive Weyl fermions, whose filling factors are expected to follow a $2(n + \frac{1}{2})$ sequence [62, 104]. The two gapped states in the QH regime (i.e., Chern insulators), one that develops from the 2D TI and the other from

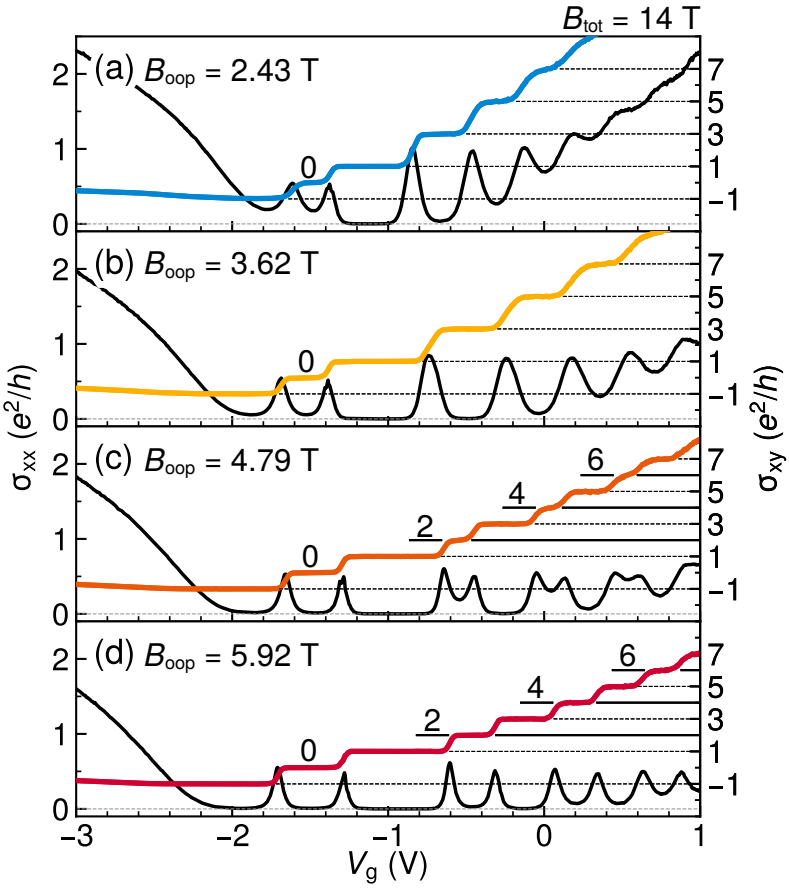

Figure 4.5: Odd integer quantum Hall effect and valley splitting. (a) Longitudinal and Hall conductivities, σ_{xx} and σ_{xy}, as a function top-gate voltage for a fixed B_{oop} = 2.43 T. The same is shown in (b) for B_{oop} = 3.62 T, in (c) for B_{oop} = 4.79 T, and in (d) for B_{oop} = 5.92 T. In all 4 cases, B_{tot} = 14 T, which is fixed, and B_{ip} > 12.5 T. σ_{xy} is drawn with different colors and σ_{xx} is drawn in black. Dashed black lines, ν = odd integers. Bold lines, ν = even integers, which are also labelled. The σ_{xy} = 0 plateaus are labeled separately.

the 2D WSM state, are thus easily distinguished at low out-of- plane fields. Another 32 sets of conductivity traces are presented in Figure 4.6 and Figure 4.7, which were acquired at lower B_{tot} values (down to 10 T) and using the same 4 tilt angles, showing that the results in Figure 4.5 continue to hold for the full range of the gapless phase.

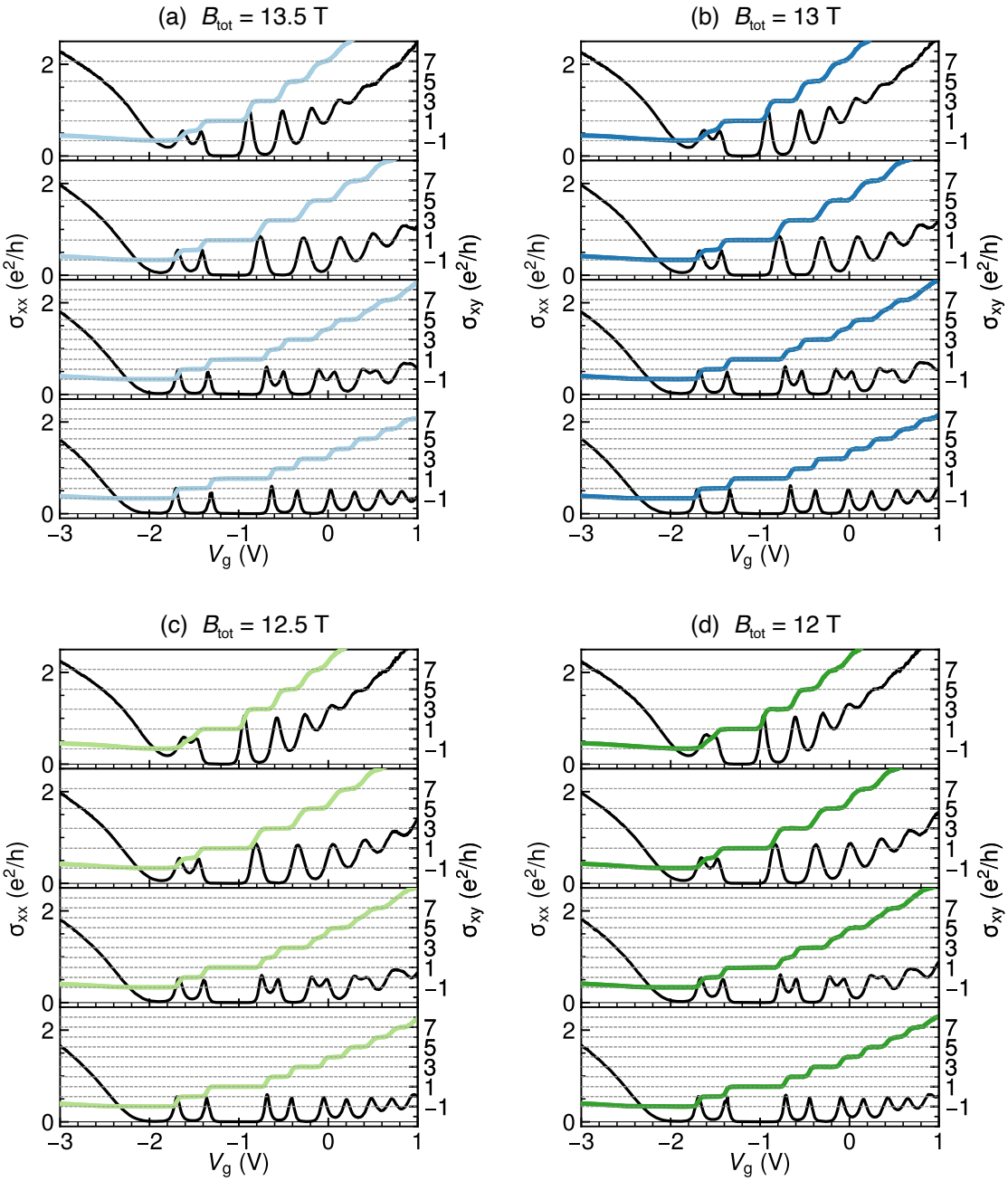

Figure 4.6: Longitudinal and Hall conductivities, σ_{xx} and σ_{xy}, as a function top-gate voltage for the 18 nm sample. The setup is similar to that of Figure 4.5, but with smaller total magnetic fields. Panels (e)-(h) show tilt cases for total magnetic fields of 13.5 T, 13 T, 12.5 T, and 12 T, respectively.

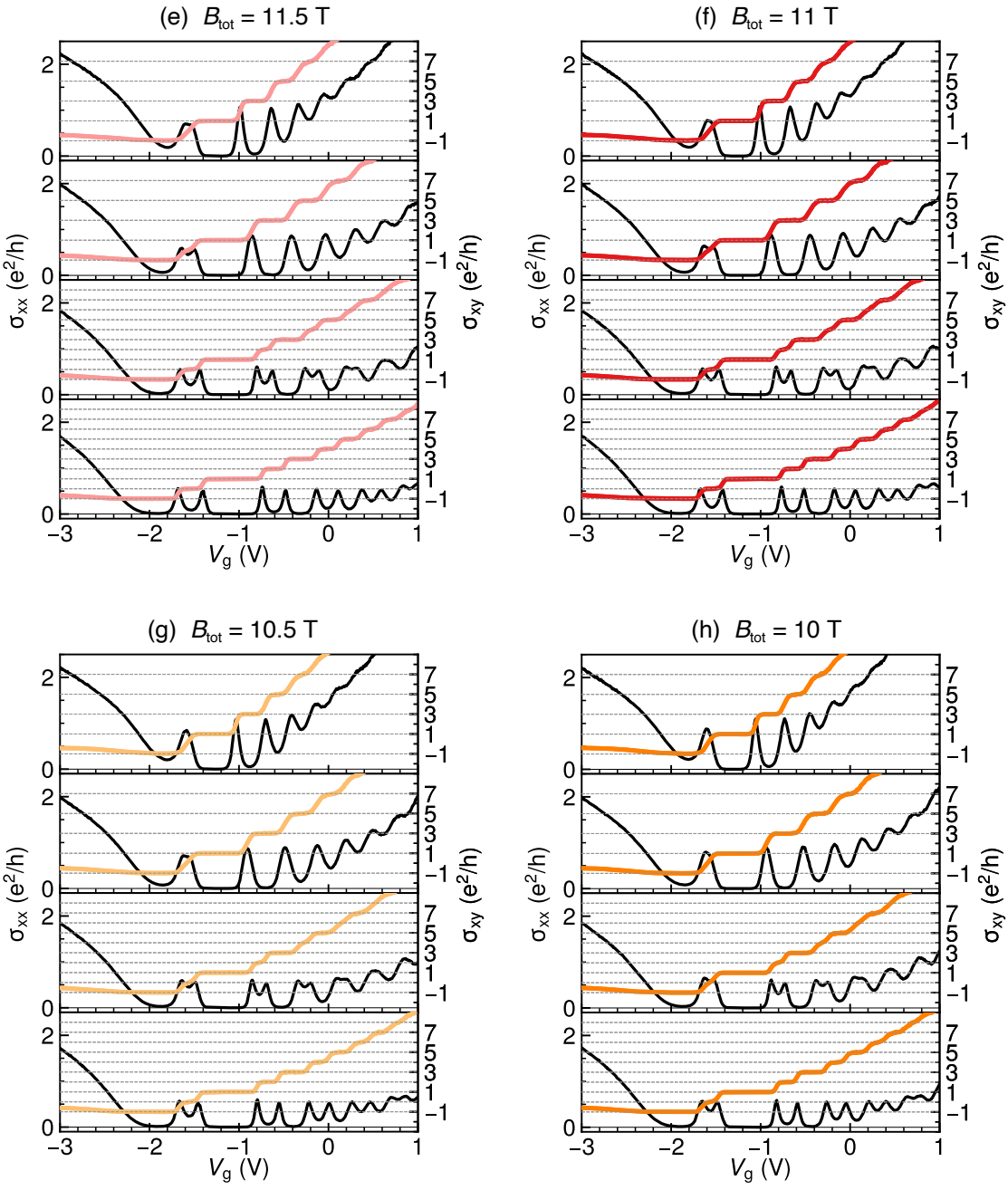

Figure 4.7: Continued from Figure 4.6. Panels (e)-(h) show tilt cases for total magnetic fields of 11.5 T, 11 T, 10.5 T, and 10 T, respectively.

The key features in the data can be explained within a minimal model for a gapped 2D Weyl semimetal under a Zeeman field. For a Weyl point in a single valley (K^+), the Hamiltonian under a magnetic field is well-studied and can be written as:

$$\mathcal{H}_{K^+} = \begin{pmatrix} \Delta & v_F\Pi^\dagger \\ v_F\Pi & -\Delta \end{pmatrix} \tag{4.2}$$

$$\mathcal{H}_{K^+} = \begin{pmatrix} g_z B_z & v_F[(\hbar k_x + eB_z y) - \hbar\nabla_y] \\ v_F[(\hbar k_x + eB_z y) + \hbar\nabla_y] & -g_z B_z \end{pmatrix} \tag{4.3}$$

where Zeeman coupling is included as a mass term $\Delta = g_z B_z = g_z B_{oop}$, g_z is an out-of-plane g factor, and v_F is the Fermi velocity. The energy eigenvalue for the $n^+ = 0$ Landau level is directly obtained as $E(n^+ = 0) = g_z B_z$, and the higher order LLs are $E(|n^+| \geq 1) = \pm\sqrt{|n^+|\hbar^2\omega_0{}^2 + \Delta^2}$, where $\omega_0 = \sqrt{2}v_F/l_B$. The valley with opposite chirality (K^-) shares the same solutions for higher order LLs, but the $n^- = 0$ LL experiences a sign change, with an eigenvalue of $E(n^- = 0) = -g_z B_z$. This model of the 2D WSM readily explains the observed 2-fold degeneracy of higher order LLs as originating from an expected valley degree of freedom, while the absence of any degeneracy for the two 0^{th} LLs are accounted for by their chirality.

By only keeping up to linear terms in momentum, however, the model cannot describe the lifting of the valley degeneracy at large B_{ip}, seen in Figures 4.5 (c) and (d), which creates additional σ_{xy} plateaus at even filling factors of 2, 4, and 6. It is worth noting that the removal of this degeneracy is likely not a result of a Lifshitz transition at high V_g, since all data in Figure 4.5 span the same V_g range. This observation should motivate future work towards a more complete theoretical description. Similar to conventional semiconductor

systems, such as AlAs quantum wells, lifting of valley degeneracy may originate from electron correlation effects [105].

4.6 Concluding remarks

In conclusion, the magnetotransport studies presented here provide evidence for a Zeeman field-induced 2D WSM state in Cd_3As_2, as indicated by: (1) when the chemical potential is tuned to charge neutrality, closing of the inverted gap in Cd_3As_2 leads to saturated resistivities on the order of h/e^2, which span a range of in-plane fields; (2) a well-developed odd integer quantum Hall effect appears when a small out-of-plane magnetic field is applied along with the in-plane field, which is a direct consequence of the chiral zeroth Landau levels contributed by 2D Weyl nodes; and (3) experimental observations are consistent with a four-band $\boldsymbol{k}\cdot\boldsymbol{p}$ model of confined Cd_3As_2 films [11, 24] under an in-plane magnetic field and considering effective g factors calculated by first-principles methods [97, 98].

The identification of a 2D WSM phase adds a new chapter to the already fascinating electrical properties of Cd_3As_2, which first drew attention as a *3D* topological Dirac semimetal more than a decade ago [11]. Future studies might consider characterizing additional transport signatures of 2D Weyl nodes, such as non-linear Hall effects up to the third order [106, 107]. Time-reversal and inversion symmetries should in principle forbid the first and second order Hall signals in Cd_3As_2, making the third order one the predominant effect. One (intrinsic) contribution to a third order Hall effect is the Berry connection polarizability tensor, which has only recently begun to receive theoretical attention

[107, 108].

Observing an anomalous Hall effect [97] driven by the in-plane field could also become possible at even lower sample temperatures (~ mK). To measure such gapped phases requires breaking C_2T symmetry, a subject that was explored in a theoretical study [27] motivated by this experimental work. Possible strategies include applying an additional, controlled out-of-plane field or eliminating C_2 symmetry by developing lattice-matched Cd_3As_2 samples grown in the low-energy (112) orientation. Lastly, it is worth noting that the Zeeman field-induced mechanism reported here holds implications beyond Cd_3As_2 and may be applied to a broader range of narrow bandgap semiconductors.

Chapter 5

Superconductor-Cd_3As_2 hybrid interfaces

This chapter, mostly based on [16], discusses preliminary work on hybrid structures combining Cd_3As_2 with an *s*-wave superconductor, a potential approach for realizing topological superconducting phases. The emphasis is on the superconductor-Cd_3As_2 interface, which needs to allow Cooper pairs to pass through while preserving key materials properties, including the high-mobility electronic states in Cd_3As_2 quantum wells. In particular, a simple device structure is introduced, which is based on (001)-oriented Cd_3As_2 Hall bars partially covered with either Nb or Sn as the superconductor. Under perpendicular magnetic fields, devices with sputter-deposited Nb show signs of superconductivity and a $\nu = 1$ QH plateau in two separate field regimes. In contrast, devices with thermally-evaporated Sn fail to exhibit superconductivity, suggesting poor interface transparency.

5.1 Materials considerations

Topological superconductors (TSCs) feature a superconducting energy gap in the bulk and gapless quasiparticle states along their boundaries or within defects [5]. Experimental searches for these quasiparticles are driven by their promising application as robust qubits in quantum computing systems [109] as well as basic scientific interest. Besides intrinsic candidate compounds, a TSC can also be engineered at interfaces in hybrid structures [110]. One of the most prominent hybrid approaches is based on a theoretical proposal by Fu and Kane [111], which involves interfacing an *s*-wave superconductor (SC) with the surface or edge states of a topological insulator (TI).

Realizing this proposal requires comprehensively understanding and optimizing numerous factors, including the roles of different material properties and their compatibility at the interface. While hybrid structures with 3D and 2D TIs are believed to be less sensitive to disorder than other approaches [112], interfaces must nevertheless preserve the topological boundary states, and, at the same time, they must be transparent to the Cooper pairs. For example, Ar plasma treatments are generally employed to improve the transparency of the interface [113, 114], but highly energetic processes may cause structural damage even deep below the surface, as is well known from compound semiconductor processing [115]. Hence, interpreting transport signatures of hybrid superconductor/topological devices can be challenging [116] and would benefit from understanding the behavior of electronic states after they have been interfaced with a particular SC.

Inspired by the Fu-Kane proposal, the goal of the present chapter is to evaluate the influence of depositing various *s*-wave SCs on the two-dimensional electronic states of Cd_3As_2. While induced superconductivity has been investigated for (112) surfaces of Cd_3As_2 [117, 118, 119], these samples were bulk-like and thus not suitable for realizing proposals that involve isolating the contribution from boundary states. Instead, the focus here is on (001) Cd_3As_2 thin films, which have not yet been explored in hybrid devices. A shared design feature in devices used in this chapter is a superconducting strip placed over the central area of a Hall bar mesa. One type of device employs Sn, a type-I SC, typically deposited by thermal evaporation. The other device uses Nb, a type-II SC, which is sputtered due to its high melting point of ~2500 °C. The sputtering process is known to be generally more aggressive and damaging than thermal evaporation [115].

5.2 Processing and characterization

All experiments were performed on devices fabricated from a standard 20 nm Cd_3As_2 film grown on the nearly lattice-matched buffer discussed earlier [20]. After growth, Hall bars with a 50 µm channel width (and a geometric factor of 1) were patterned by photolithography, mesa isolated by Ar ion beam etching, and contacted by sputtered Au/Ti leads. Two separate processes were then used for depositing a superconductor in the center of the Hall bar. Sn (99.9999%, Alfa Aesar Inc.) was thermally evaporated at rates between 1 Å s^{-1} to 5 Å s^{-1} in a chamber with a base pressure of less than 3×10^{-6} Torr. Magnetron sputtering at a DC power of 250 W was used for Nb deposition (99.95%, Angstrom Sciences Inc.)

under 30 standard cubic centimeters per minute of Ar gas flow at a chamber pressure of 4×10^{-3} Torr. Additionally, control devices were processed without depositing any superconductors. Electrical measurements were carried out using 4-point measurements in magnetic fields (B) up to 9 T. Longitudinal resistivities (ρ_{xx}) were symmetrized and Hall resistivities (ρ_{xy}) were antisymmetrized with respect to the direction of B:

$$\begin{aligned} \rho_{xx} &= \frac{\rho_{xx}(+B) + \rho_{xx}(-B)}{2}, \\ \rho_{xy} &= \frac{\rho_{xy}(+B) - \rho_{xy}(-B)}{2}. \end{aligned} \tag{5.1}$$

As an overview, Figure 5.1 presents optical micrographs of three Hall bar devices. Figure 5.1 (a) depicts the pristine (i.e., not covered by a superconductor) control device, which is a standard eight-terminal Hall bar. On the other devices a strip of Sn (or Nb) is centered on the Hall bar mesa, leaving a 15 µm gap from the mesa periphery. The distances between the superconductor and the neighboring voltage measurement contacts are at least 27.5 µm. The partially Nb-covered device further differs from the Sn one [Figure 5.1 (b)] by having its superconducting strip offset to create a pristine region between the contacts labeled 1 and 2, as shown in Figure 5.1 (c). Lastly, a cross-sectional schematic of the devices (not to scale) is provided in Figure 5.1 (d).

To gain a closer look at the hybrid interfaces, scanning transmission electron microscopy (STEM) was employed on cross-section specimens prepared by focused ion-beam liftout (FEI Helios NanoLab 600). Imaging was performed in high-angle annular dark-field (HAADF) mode using a beam voltage of 200 kV and a semi-convergence angle of 10.5 mrad (TFS Talos G2). Figure 5.2 (a) shows the Sn layer to be granular, consistent with the

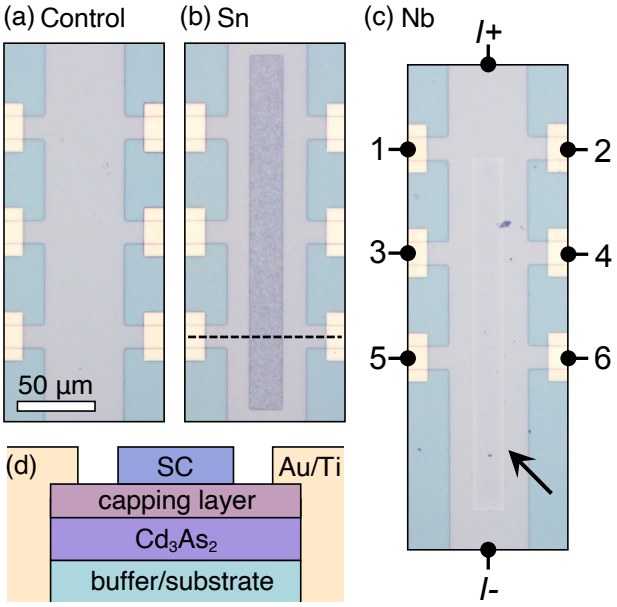

Figure 5.1: Overview of the Cd_3As_2 hybrid devices. (a) Optical micrographs of the control device, (b) partially Sn-covered device, and (c) partially Nb-covered device. Nb is transparent and more difficult to make out than Sn, which is granular. The arrow in panel (c) points to the outline of the Nb region. The Nb strip does not cover the region between contacts 1 and 2. Voltage contacts of the Nb-covered device are labeled. The Sn and Nb regions both measure 20 µm by 220 µm with a thickness of 30 nm. (d) Cross-sectional schematic along the dashed line in panel (b). Dimensions in the schematic are not to scale.

optical images in Figure 5.1 (b), forming large islands and not fully covering the Cd_3As_2 surface. In contrast, the Nb layer is continuous and uniform, as seen in Figure 5.2 (b). This comparison indicates the poor wetting behavior of thermally evaporated Sn on Cd_3As_2, despite its superconductivity. Data showing the superconducting transition of Sn on Cd_3As_2 can be found in the Supplementary Information of [16]. Interestingly, no reaction layers were detected at either interface in Figure 5.2, implying that the differences in transport between the devices, which will be discussed next, cannot be attributed to the formation of reaction products at these interfaces.

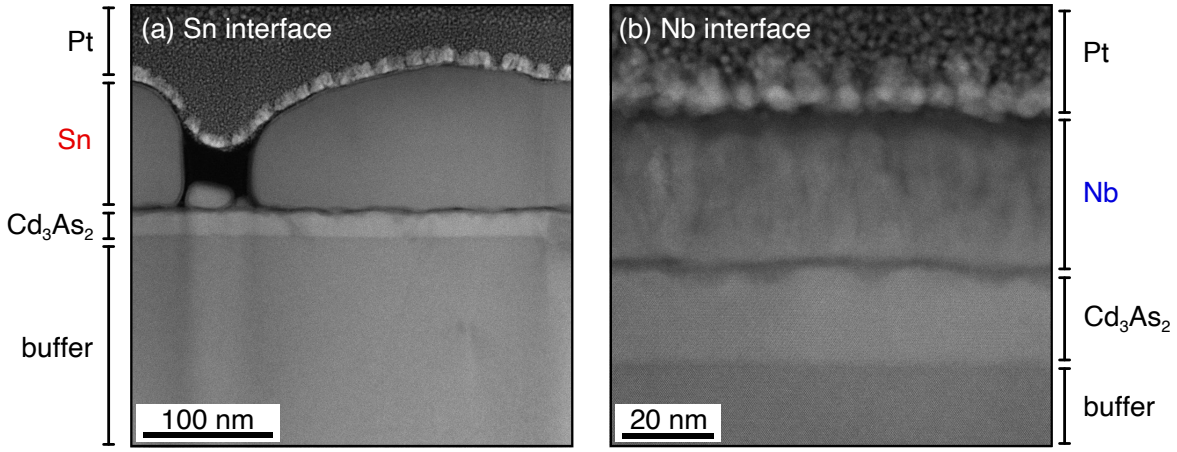

Figure 5.2: Two SC-Cd_3As_2 interfaces. Cross-sectional HAADF-STEM images of interfaces with (a) Sn and (b) Nb. In both TEM specimens there is a Pt protective layer. The image of the Nb-covered device corresponds to device A. The capping layer is not labeled, but visible as a thin dark region between Cd_3As_2 and the SC.

5.3 Magnetotransport results

5.3.1 Sn-covered hybrid device

First, a comparison can be made between the Sn-covered device and the control device. Figure 5.3 shows $\rho_{xx}(B)$ and $\rho_{xy}(B)$ of the control and Sn devices, respectively, measured at 2 K. The measurement setup for both devices was $\rho_{xy} = V_{1,2}/I_{bias}$ and $\rho_{xx} = V_{4,6}/I_{bias}$, where the subscripts refer to contacts as indicated in Figure 5.1 (c). At low magnetic fields ($|B| < 0.5$ T), the Hall mobility, μ_{Hall}, is found to be 2190 $cm^2\,V^{-1}\,s^{-1}$ at a carrier density, n_{2D}, of 3.42×10^{11} cm^{-2} for the control device. The corresponding values for the Sn-covered device are $\mu_{Hall} = 6122$ $cm^2\,V^{-1}\,s^{-1}$ and $n_{2D} = 1.76 \times 10^{11}$ cm^{-2}. This behavior of nearly threefold greater μ_{Hall} for the Sn-covered device is expected, since μ_{Hall} is strongly

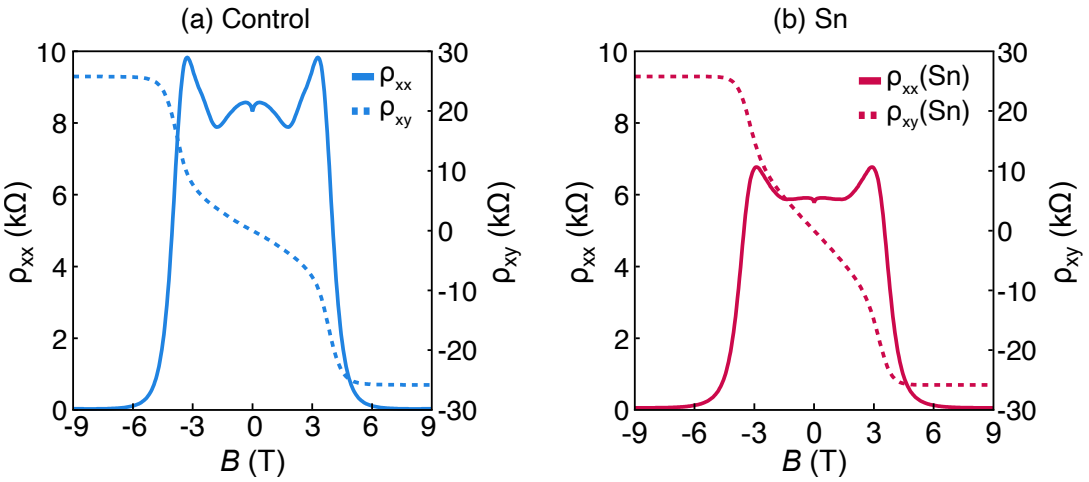

Figure 5.3: Comparison of the Sn-covered device with the control device. Longitudinal and Hall resistivities of (a) control device and (b) partially Sn-covered device at $T = 2$ K. The measurement setup for both devices was $\rho_{xy} = V_{1,2}/I_{bias}$ and $\rho_{xx} = V_{4,6}/I_{bias}$

dependent on n_{2D} in these quantum wells. A similar trend had also been seen in the higher mobility films discussed earlier [14].

Despite the differences in carrier density and mobility, the quantum transport properties of the two devices are largely similar. Around $B = 4$ T, both devices develop a clear $\nu = 1$ quantum Hall plateau in ρ_{xy} that is accompanied by near-zero ρ_{xx}. This indicates that in both cases the chemical potential remains in the first electron subband, which in fact facilitates analysis by avoiding complications introduced by occupation of the second subband (and the resulting quantum oscillations). Overall, the fact that transport is dominated by the response of Cd_3As_2 points to thermal evaporation of Sn on the Cd_3As_2 mesa preserving the quality of the underlying interface. Although no superconductivity is measured in the Hall bar-based device, the Sn layer itself superconducts as mentioned earlier. Additional higher resolution measurements of ρ_{xx} at magnetic fields below the critical field of Sn are also provided in the Supplemental Information of [16].

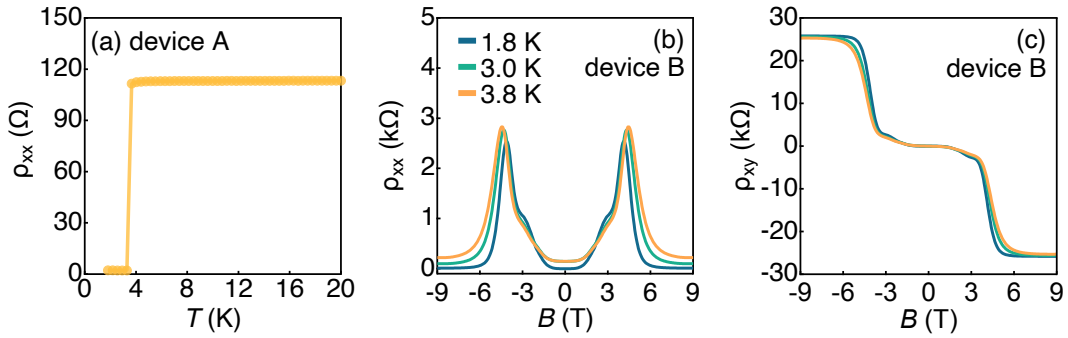

Figure 5.4: Temperature and magnetic field dependence of partially Nb-covered devices. (a) Longitudinal resistivity of device A as a function of temperature. A superconducting transition appears near T = 3.6 K. (b) Longitudinal and (c) Hall resistivities of device B (lithographically identical to device A) at temperatures of 1.8 K, 3.0 K, and 3.8 K. The measurement setup for both Nb-covered devices was $\rho_{xy} = V_{3,4}/I_{bias}$ and $\rho_{xx} = V_{4,6}/I_{bias}$.

5.3.2 Nb-covered hybrid device

Next, Figure 5.4 (a) shows ρ_{xx} of a Nb-covered Hall bar (device A) as a function of temperature at zero applied magnetic field. The contact configuration was $\rho_{xx} = V_{4,6}/I_{bias}$. This temperature dependence clearly shows a superconducting transition associated with the Nb strip. In particular, ρ_{xx} drops by more than a factor of 100 as the temperature is reduced below T = 3.6 K, consistent with a transition to a superconducting state and current flow through the Nb. Figures 5.4 (b) and (c) show the magnetic field dependence of ρ_{xx} and ρ_{xy} measured on device B (which was prepared using an identical procedure as device A) at three different temperatures. Here, $\rho_{xy} = V_{1,2}/I_{bias}$ and $\rho_{xx} = V_{4,6}/I_{bias}$.

The main difference, relative to the control device shown in Figure 5.3 (a), is at low B-fields, where ρ_{xx} vanishes and ρ_{xy} shows a much weaker B dependence, indicative of superconductivity. As expected from the $\rho_{xx}(T)$ trace in Figure 5.4 (a), the ρ_{xx} trace taken at T = 1.8 K, i.e., below T_c (~ 3.6 K) has lower resistance values near B = 0 than the two

traces recorded at $T = 3.0\,\mathrm{K}$ and $T = 3.8\,\mathrm{K}$, respectively. Above the critical field of Nb, the Hall coefficient remains small, as ρ_{xy} varies slowly at low B, reflecting an increased carrier density relative to the control device, consistent with carrier transport through the Nb even in the non-superconducting state. At $T = 3.8\,\mathrm{K}$ (above T_c), for example, $n_{2D} = 7.9 \times 10^{12}\,\mathrm{cm}^{-2}$, which is more than an order of magnitude higher than the control device. The Nb contribution is also evidenced by a monotonic increase of ρ_{xx} with increasing field. Thus, current flows through the Nb until the sample reaches a well-developed QH plateau. In particular, at $B > 3\,\mathrm{T}$, both ρ_{xx} and ρ_{xy} resemble those of the control device, exhibiting a clearly developed $\nu = 1$ QH state in ρ_{xy} and, in ρ_{xx}, an associated maxima at the transition at 4.5 T.

5.3.3 Two transport regimes

The results from the partially Nb-covered devices can be understood in terms of two transport regimes. At low B-fields, and for this particular quantum well with a modest mobility, Landau levels are not fully developed and therefore the 2D bulk remains conducting. The bulk of the not yet quantized surface serves as a contact to the Nb-covered region. As a result, measurements reflect the behavior of Nb. When the chemical potential is between LLs, carriers in the 2D bulk are localized, such that charge transport occurs only through the edge channel. In this case, the Nb-covered region is effectively isolated (any edge channels around the Nb strip are not contacted) and no current flows through Nb. This interpretation is confirmed also by the behavior of the devices at higher temperatures ($T =$

10 K), as seen in the Supplementary Information of [16].

It is important to note that the present measurements cannot distinguish between superconductivity in the Nb itself versus induced superconductivity in Cd_3As_2. Evidence for proximitized superconductivity and its nature requires other measurements, i.e., of Josephson effects, which are beyond the scope of this work. Independent of the question of induced superconductivity, however, the fact that signatures of superconductivity are detected in the Nb-covered devices indicates good interface transparency. At the same time, the intrinsic transport properties of the Cd_3As_2 thin film are well preserved. Both are necessary conditions towards the realization of TSCs in more advanced hybrid structures.

Additionally, it is instructive to compare the Nb-covered devices to those covered by Sn, which do not exhibit superconductivity or even transport through the Sn strip. As noted earlier, the reduced n_{2D} after Sn deposition may suggest the formation of a barrier layer that results in carrier depletion. In general, surface treatments and/or overlayers have a significant influence on band bending in Cd_3As_2 [57]. The observed poor wetting behavior of Sn on the capped Cd_3As_2 surface is an indicator that good electrical contact between these two materials is more difficult to establish than for the Nb interface. In addition, sputtering, which is more energetic than thermal deposition [115], may also serve to provide a better electrical contact, for example by removing surface adsorbates or causing a small degree of intermixing that is not detectable in the electron micrographs of Figure 5.1. It is therefore possible that better coupling between Sn and Cd_3As_2 could be achieved by optimizing the deposition process or by surface cleaning steps.

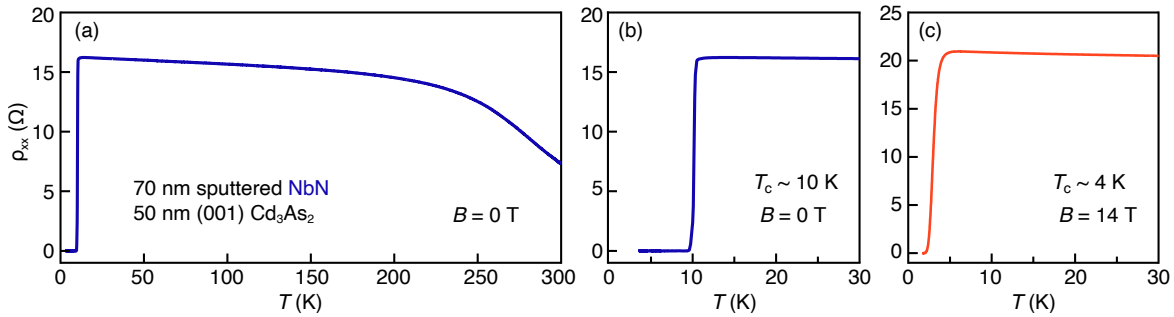

Figure 5.5: $\rho_{xx}(T)$ measurements of NbN sputtered on an (001) Cd_3As_2 film. (a) and (b) Measurements at $B = 0$ T, and (c) measurements at $B = 14$ T. Critical temperatures (T_c) are estimated from the onset of the superconducting transitions.

5.4 Concluding remarks

This chapter has presented a simple yet effective device structure for qualitatively assessing superconducting hybrid interfaces with Cd_3As_2. The initial results suggest the Nb/(001) Cd_3As_2 combination holds promise for implementing TSC proposals such as the Fu-Kane model. Future research should now aim for a quantitative understanding of the superconducting state in this context.

The pairing of Cd_3As_2 quantum wells, known to exhibit well-developed QH states, with superconductors, may also be relevant to recent proposals for creating non-Abelian quasiparticles [120, 121, 122]; this relies on inducing superconductivity into the chiral QH edge states under high magnetic fields, requiring the use of a SC with a high H_{c2}. One possibility for Cd_3As_2 is to use NbN. Early tests indicate that depositing NbN on 50 nm Cd_3As_2 films is achievable, maintaining the film quality and superconductivity up to $B =$ 14 T, as shown in Figure 5.5.

Chapter 6

Summary and future directions

6.1 Summary

This dissertation explores the development of (001) Cd_3As_2 quantum wells, encompassing the full process from epitaxial growth using III-antimonide buffers and substrates to making gate-tunable devices and magnetotransport measurements at low temperatures. The goal is to deepen knowledge of band structure engineering techniques that can modify and control the topology of Cd_3As_2. The main findings of this dissertation are summarized below.

- **Chapter 2:**

  The focus of this dissertation, the MBE growth of Cd_3As_2 in the high-energy (001) orientation, is shaped by several materials factors and thermal constraints. The growth process leverages the low vapor pressure of the Cd_3As_2 compound to ensure the transfer of stoichiometry. Achieving the desired topological 3D Dirac semimetal crystal

structure necessitates keeping the substrate temperature below 300 °C. Cd_3As_2 epitaxy is further facilitated by a nearly lattice-matched buffer of $Al_{0.45}In_{0.55}Sb$, which serves to manage the ~ 3.3% compressive misfit with the GaSb substrate and prevent parallel conduction. Also due to thermal stability considerations, migration enhanced epitaxy is employed to deposit a GaSb capping layer that protects the Cd_3As_2 quantum well during device processing.

- **Chapter 3**:

(001) Cd_3As_2 quantum wells were fabricated into micron-scale devices equipped with electrostatic top gates for transport experiments. Substantial enhancement to the gate performance was achieved by the addition of the GaSb capping layer and an *ex situ* oxygen plasma exposure prior to gate dielectric deposition. The capability to gate-tune the chemical potential across the charge neutrality region enabled the study of an insulating $\nu = 0$ quantum Hall state that demonstrated an unusual dependence on the magnetic field. Applying this technique to higher mobility samples, the subband Landau level spectrum of Cd_3As_2 was successfully mapped, providing transport evidence of subband inversion across various well thicknesses.

- **Chapter 4**:

Cd_3As_2 quantum wells that belong to the band-inverted regime exhibit unique transport behavior when subjected to in-plane (Zeeman) magnetic fields. The results indicate a topological phase transition from the inverted phase to an emergent 2D Weyl semimetal phase. This gapless phase is predicted to host a pair of Weyl nodes

of opposite chirality at charge neutrality that are protected by space-time inversion symmetry. Transport signatures that could be attributed to these Weyl nodes include saturated resistivities $\sim h/e^2$ at charge neutrality, that persist over a range of in-plane magnetic fields. Furthermore, placing the Weyl semimetal in a small out-of-plane magnetic field gives rise to an odd-integer QH effect, characteristic of degenerate, massive Weyl fermions. These findings can be qualitatively explained by adopting a 4-band $\boldsymbol{k}\cdot\boldsymbol{p}$ model of Cd_3As_2 and using first-principles effective g factors.

- **Chapter 5**:

Hybrid structures combining low carrier density (001) Cd_3As_2 quantum wells with an s-wave superconductor, either Nb or Sn, were fabricated and measured under perpendicular magnetic fields. Initial results show that Cd_3As_2 Hall bars, when partially covered with sputtered Nb, exhibit signatures of superconductivity at low magnetic fields and a pronounced $\nu = 1$ QH effect at higher fields, suggesting their compatibility. In contrast, devices covered by thermally-evaporated Sn fail to exhibit superconductivity, which is a result of poor wetting during Sn deposition. These findings also suggest additional research possibilities in inducing superconductivity into the chiral QH edge states of Cd_3As_2, particularly by using large-H_{c2} superconductors such as sputtered NbN.

6.2 Future directions

Developing Cd_3As_2 quantum wells as a platform for engineering topological phases has been a rewarding experience. Yet, there is still much to be done to build upon the groundwork established in this dissertation. A focus has always been on enhancing the crystalline quality of Cd_3As_2, and this research can be potentially explored in the two directions described below.

6.2.1 Virtual substrates

A fundamental challenge in the MBE growth of Cd_3As_2 is the absence of a commercial, lattice-matched substrate. This challenge has led to a first-generation of $Al_{0.45}In_{0.55}Sb$ buffers or virtual substrates with an in-plane lattice constant near 6.3 Å. Enhancing the structural quality of these buffers is likely to raise the electron mobility of Cd_3As_2 quantum wells, and, by reducing disorder from the buffer, help clarify questions regarding important details of the Cd_3As_2 band structure under quantum confinement.

Currently, high densities of misfit dislocations are present at the $Al_{0.45}In_{0.55}Sb$/GaSb interface, with a subset extending into the Cd_3As_2 active region [20]. Adopting more advanced virtual substrate technology, similar to that used in the In(As,Sb) infrared detector community [123], is a possible strategy to effectively manage these defects. One approach involves using a compositionally graded (Al,Ga,In)Sb layer prior to the growth of the $Al_{0.45}In_{0.55}Sb$ barrier [124]. Figure 6.1 (a) shows a cross-section schematic illustrating

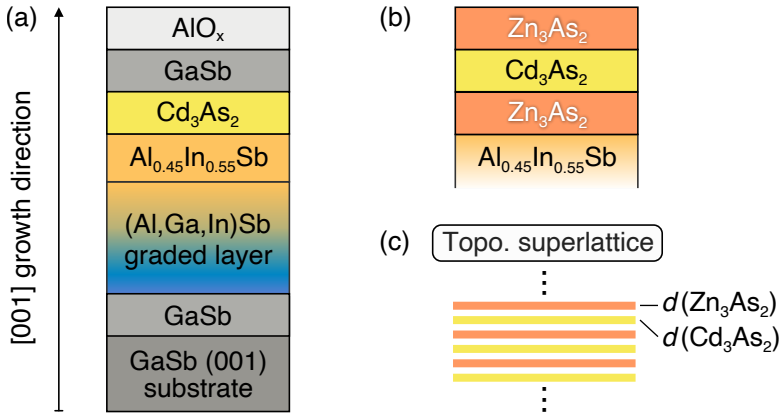

Figure 6.1: Future directions for epitaxial growth of (001) Cd_3As_2. (a) An example of a virtual substrate incorporating a graded (Al,Ga,In)Sb layer preceding $Al_{0.45}In_{0.55}Sb$. (b) Cd_3As_2 quantum well with symmetric Zn_3As_2 barriers. (c) Superlattices made from Cd_3As_2 and Zn_3As_2.

this idea for Cd_3As_2 heterostructures. An improved buffer may also aid future microscopy studies towards a comprehensive understanding of the Cd_3As_2 thin film microstructure, especially by providing a nearly dislocation-free template for its nucleation and growth. This will greatly simplify the analysis of intrinsic dislocation and defect distributions in Cd_3As_2.

Transport will continue to be a sensitive measure of progress in materials quality. Similar to established 2D electron systems in GaAs/AlGaAs, transport phenomena in Cd_3As_2 are most discernible when only the first conduction subband is occupied. This criterion could be useful for making quantitative comparisons between Cd_3As_2 samples grown on various new buffers to understand scattering mechanisms that limit mobility. Furthermore, in samples of higher crystalline perfection, it might be worthwhile to revisit the regime of thicker films or wide Cd_3As_2 quantum wells, which display complex interactions between Landau levels, as shown in Figure 6.2.

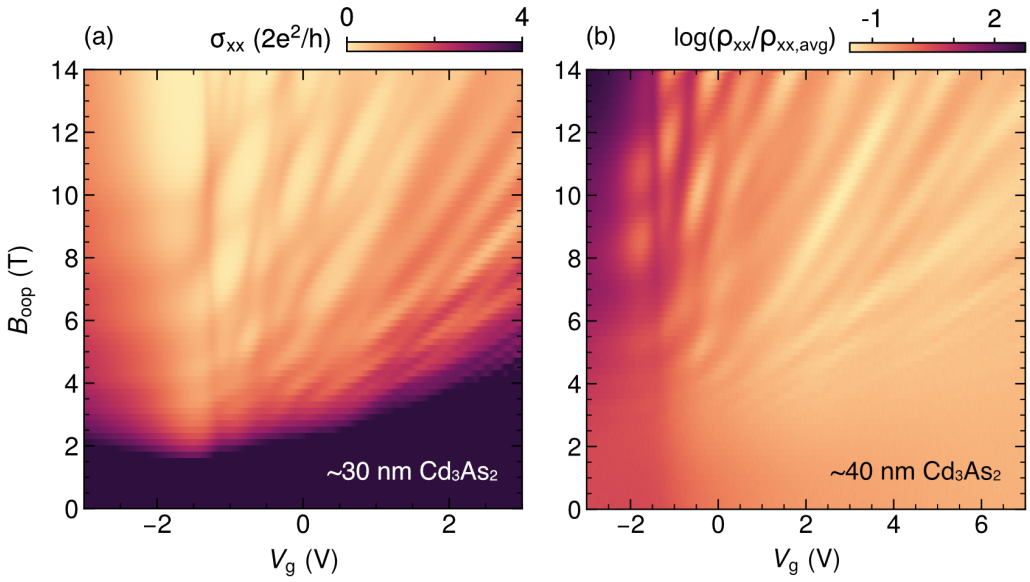

Figure 6.2: Landau level spectra of wide Cd_3As_2 quantum wells grown on the $Al_{0.45}In_{0.55}Sb$ buffer (no graded buffer). (a) $\sigma_{xx}(V_g, B)$ data acquired for a 30 nm Cd_3As_2 film. (b) $\rho_{xx}(V_g, B)$ data normalized by the average ρ_{xx} value for a 40 nm Cd_3As_2 film. Note the use of a log scale to highlight LL crossings. All measurements were done at $T = 2$ K.

6.2.2 Topological superlattices

A second direction is the search for discontinuous materials improvements. This naturally leads to the idea of growing Zn_3As_2 in combination with Cd_3As_2. The similarities in thermodynamic and chemical properties of these two materials [34, 35] suggest that Zn_3As_2 can also be evaporated from a compound source, although trial growths should avoid using the main chamber. More importantly, Zn_3As_2 is closely lattice-matched to Cd_3As_2, sharing the same tetragonal point group, but is a topologically trivial insulator with a bulk bandgap of ~ 1 eV [35]. As shown in Figure 6.1 (b), one can imagine designing Cd_3As_2 quantum wells with lattice-matched Zn_3As_2 barriers, where defects from the mismatched GaSb substrate can be stopped in the bottom barrier before reaching the active region.

Finally, it might be possible to extend the ideas of band structure engineering to design topological superlattices based on Cd_3As_2 for optoelectronic applications [Figure 6.1 (c)].

6.2.3 Testing virtual substrates

To test the virtual substrate approach, a brief collaboration was carried out with Dr. Stefan P. Svensson, who provided wafers with the graded layer structure shown in Figure 6.1 (a). Layer information for the two types of III-V structures that were provided are summarized in Table 6.1, while further details can be found in [123]. Standard As capping was used for protecting the sample surface during shipping (wafer VS-1).

Both types of wafers required re-growth of the buffer before the Cd_3As_2 layers, yet the main obstacle at this stage was preparing an appropriate starting surface for this process. In VS-1, which was capped by As, this issue was possibly caused by a thermally activated reaction between As and Sb on the surface. For VS-2, which lacked an As cap, surface preparation was likely hindered by an oxide layer from the Al-rich buffer. The outcomes of these re-growth experiments on virtual substrates are described next, focusing on VS-1. They suggest that future studies should experiment with Sb as a capping layer to bypass the complications of having an As cap on an antimonide surface.

Table 6.1: Virtual substrates grown on GaSb, courtesy of S. P. Svensson.

Sample	(Al,Ga,In)Sb	(Al,In)Sb	Capping layer
VS-1	2.2 µm	0.5 µm, $Al_{0.53}In_{0.47}Sb$	As
VS-2	2 µm	0.5 µm, $Al_{0.55}In_{0.45}Sb$	–

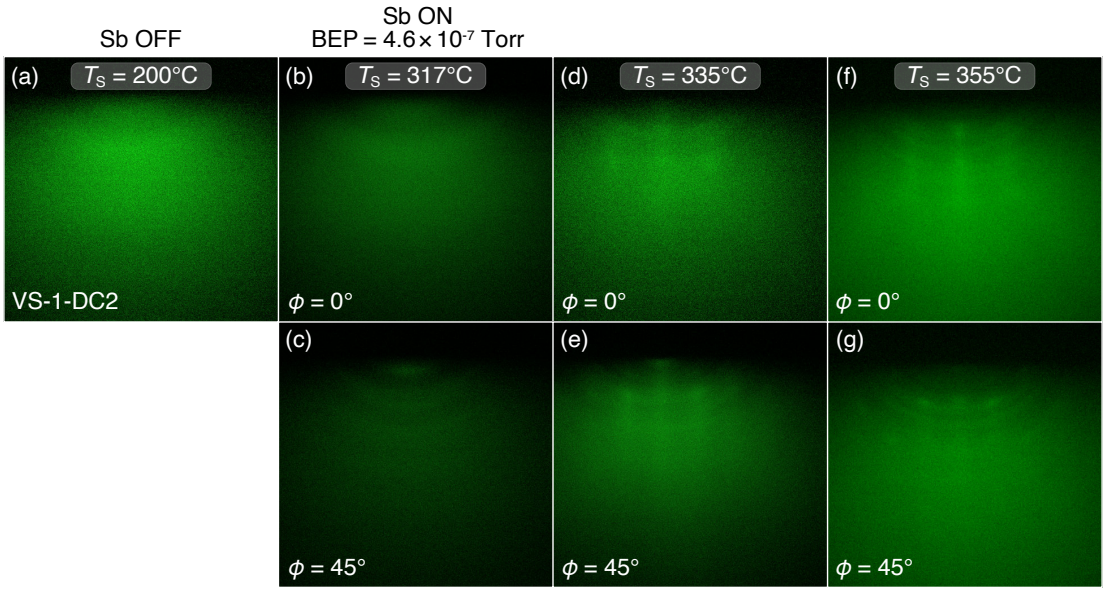

Figure 6.3: Thermal de-capping. (a) RHEED pattern after holding the sample at a substrate temperature of 200 °C for 1 hour with no Sb flux. (b), (c) Polycrystalline RHEED patterns after reaching 317 °C and with an Sb over-pressure applied. The beam incidence angle was rotated 45° between the two patterns. Similar pairs of diffraction patterns are shown in (d), (e) for 335 °C, and in (f), (g) for 355 °C. Sample ID: VS-1-DC2.

The first experiments on VS-1 encountered difficulty with removal of the As cap. Upon heating, the As-capped surface transitioned from amorphous to polycrystalline, as demonstrated by the series of RHEED patterns in Figure 6.3. Annealing the samples at higher temperatures ($T > 400$ °C) produced a 3D surface morphology, which is undesirable because it would later necessitate coverage by a thick re-growth layer. Elevated temperatures further risk causing As for Sb exchange reactions [125], a process that could be detrimental to the quality of the (Al,In)Sb buffer.

Alternatively, hydrogen cleaning at lower substrate temperatures was considered to etch away the As cap. Figure 6.4 presents RHEED results following hydrogen etching experiments, where the H_2 partial pressure was the only variable that was adjusted. The appear-

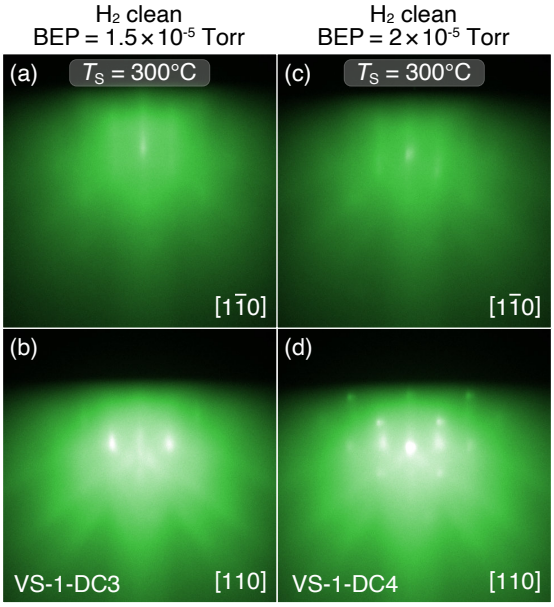

Figure 6.4: Hydrogen cleaning the As-capped surface. (a), (b) RHEED patterns after exposing the surface to ~1.5×10^{-5} Torr of H_2 at a substrate temperature of 300 °C for 30 min. Sample ID: VS-1-DC3. The same temperature and duration were used for (c), (d), but with an increased H_2 partial pressure of ~2×10^{-5} Torr. Sample ID: VS-1-DC4.

ance of a clearer diffraction pattern signifies improvements in surface quality compared to thermal desorption. However, the expected (3×1) reconstruction at low temperatures is absent, possibly due to residual As neutralizing the surface charge (see Appendix A for routine H_2 cleaning results). This preliminary data also indicates that increased H_2 pressures may lead to somewhat sharper RHEED features [Figures 6.4 (b) and (d)], although systematic verification is needed.

Re-growth of the buffer was nevertheless attempted after removing the As cap under the conditions specified in Figures 6.4 (c) and (d). The aim was to cover the interface with the thinnest buffer that would remain coherently strained, even if its alloy composition slightly differed from that of the virtual substrate. The samples were heated under an Sb overpressure of ~4.6×10^{-7} Torr until reaching the buffer growth temperature 520 °C. After

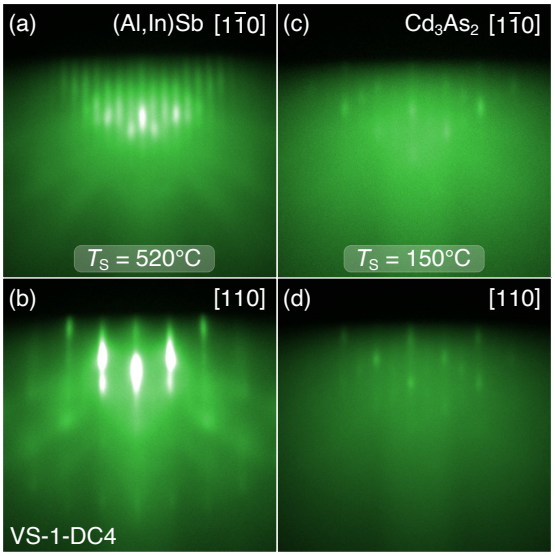

Figure 6.5: Buffer layer re-growth on the hydrogen cleaned surface, followed by Cd_3As_2 growth. (a), (b) RHEED patterns after growing 80 nm of (Al,In)Sb at 520 °C. Sample ID: VS-1-DC4. (c), (d) RHEED patterns after growing ~20 nm of Cd_3As_2 on top of the re-growth layer at 150 °C. The Cd_3As_2 surface crystal structure is 4-fold symmetric with no detectable reconstruction.

opening the Al and In shutters, it took approximately 90 s for the surface to transition from a 3D to a 2D pattern. The layer thickness was estimated to be 80 nm based on growth rate calibrations. Figure 6.5 shows RHEED patterns after completing the buffer re-growth and the subsequent Cd_3As_2 growth. The (3 × 1) surface of the (Al,In)Sb buffer was recovered while Cd_3As_2 nucleation and growth proceeded as normal. The thickness of the Cd_3As_2 layer was set to 20 nm. These results were qualitatively similar to those from routine growths, apart from a slightly higher background intensity.

However, post-growth XRD analysis showed that challenges remained with this approach. Figure 6.6 presents an asymmetric reciprocal space map acquired around the 224 Bragg reflection of the substrate. The key features of interest are two (Al,In)Sb reflections, with peak 1 from the original virtual substrate and peak 2 most likely from the re-growth

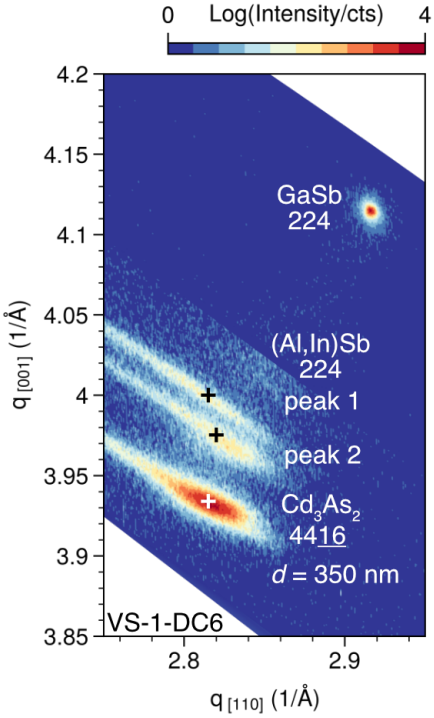

Figure 6.6: Reciprocal space map (RSM) showing the epitaxial relations between the virtual substrate and the Cd_3As_2 film layer. After hydrogen cleaning, re-growth of 80 nm of (Al,In)Sb, 350 nm of Cd_3As_2 was grown. Peak 1 originates from the (Al,In)Sb layer in the virtual substrate, while peak 2 corresponds to the re-growth layer. Data were acquired in an asymmetric geometry on a Rigaku SmartLab diffractometer using a HyPix3000 detector and Cu $K\alpha 1$ irradiation at T = 300 K. Sample ID: VS-1-DC6.

process. Peak 1 and the Cd_3As_2 layer exhibit almost identical in-plane lattice constants, but peak 2 shifts towards a smaller lattice constant. The origin of this peak is the subject of future studies, but is most likely related to excess As being incorporated into the re-growth alloy. A potential solution may be extending the annealing time under Sb over-pressure before re-growth [125].

The surface morphology of virtual substrate samples was also examined by AFM. Representative height maps are shown in Figure 6.7. The comparable RMS roughness observed in both thermal desorption and hydrogen etching tests [Figures 6.7 (a) and (b)] underscores

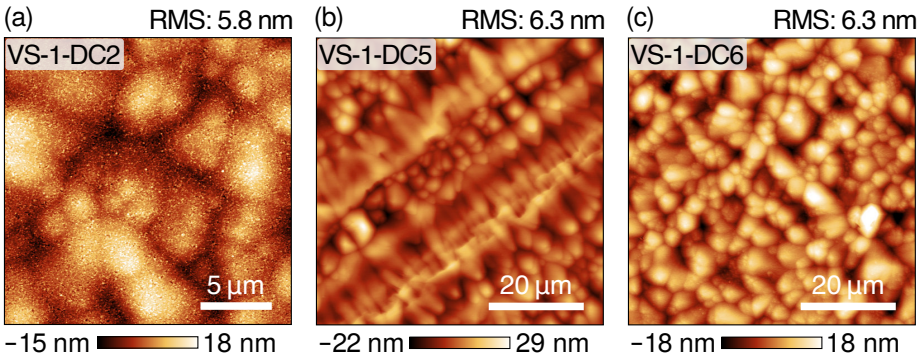

Figure 6.7: AFM height maps of virtual substrate samples. (a) Surface of the virtual substrate following an attempt at thermal desorption. (b) After hydrogen etching, re-growth of (Al,In)Sb, and the addition of a 20 nm Cd_3As_2 layer. (c) Prepared under similar conditions to (b), but with 350 nm of Cd_3As_2. Sample IDs are provided for reference.

that neither approach fully meets the requirements for preparing surfaces for re-growth. In general, the RMS roughness of VS samples after Cd_3As_2 growth is twice as high as the values reported in Chapter 2. This can be attributed to As clusters on the starting surface, as seen in Figure 6.7 (a), which was taken right after an attempt to thermally remove the cap. Additionally, [110]-oriented defects, which may be cross-hatching from the re-growth buffer, shown in Figures 6.7 (b) and (c), introduce anisotropy into the Cd_3As_2 grain structure, which is especially noticeable in the thinner Cd_3As_2 layer.

Appendix A

Hydrogen cleaning (001) GaSb

1. Outgas a substrate on the buffer chamber heater at 200 °C for 1 h. For the next steps, refer to Figure A.1.
2. Open the hydrogen tank valve to let gas into the station.
3. Check that the low pressure gauge reads above 0 psi and below 10 psi. Otherwise adjust the regulator to increase the outlet pressure to a reading that is below 10 psi.
4. In EPIC, start increasing the buffer heater temperature. Target: 450 °C, ramp rate: 5 °C min^{-1} until 350 °C, then 10 °C min^{-1} until the end.
5. Turn on the *H-flux* power supply. Verify that emission current knob is set to the 9 o'clock position, and the other knobs are at their minimum positions.
6. Switch the load lock (LL) over to the turbo pump. Do not open the LL/buffer gate valve yet.
7. Monitor the buffer ion gauge. Slowly open bellows valve # 1 (on the back side) to avoid a pressure spike.

8. Open bellows valve # 2 and verify that the buffer pressure is stable.

9. Slowly open the leak valve until the buffer ion gauge reads around 2×10^{-7} Torr. This valve is partially open between 3 to 4 and typically operated between 4 to 5. Verify that the buffer is still being evacuated by the ion pump.

10. On the *H-flux* power supply, increase the voltage to −1 kV. Slowly adjust the knob and wait 30 s at each major increment.

11. Increase the filament current slowly from 0 A to 1 A and wait 30 s. Then increase to 2 A, wait 30 s. Repeat until the filament current reaches 5 A. The "Under Emission" red light should be ON.

12. Open the leak valve until the buffer ion gauge reads above 2×10^{-6} Torr. Tip: turn slowly, wait, turn again.

13. Turn off the buffer ion gauge, but do not turn off the LL ion gauge.

14. On the electronics rack, locate the buffer ion pump controller. Select "High Voltage Operate", then "Display Select", choose the option "OFF", and finally select "Enter". The H_2 pressure in the buffer chamber can now be safely increased.

15. Open the LL/buffer gate valve. The LL ion gauge should spike and stabilize at a reading close to 5×10^{-6} Torr. Open the leak valve until the target pressure of 1×10^{-5} Torr is achieved. Verify that the turbo pump status is normal.

16. Pause and wait for the buffer heater to reach >350 °C before the next step.

17. Slowly increase the filament current while paying attention to the emission current.

Pause as soon as the emission current increases. Wait for 2 min.

18. Slowly increase the filament current until the "Under Emission" light is OFF. Then, turn the filament current knob a 1/4 of a full turn. The emission current should not respond to this extra adjustment.
19. Slowly increase the emission current. From 0 mA to 10 mA, wait 30 s at each minor increment. Step in larger increments past 10 mA and wait 10 s after each increase.
20. When the emission current reaches half of its maximum value, slowly increase the voltage to its maximum value.
21. Pause and wait for the buffer heater to reach 450 °C before the next step.
22. Increase the emission current to its maximum value. Start a 30 min timer.

---

1. When the time is up, cool down the buffer heater to 200 °C.
2. Slowly decrease the emission current to 10 mA.
3. Below 10 mA, slowly decrease the emission current and stop when the knob is at the 9 o'clock position. The "Under Emission" light will turn ON.
4. Slowly decrease the filament current and pay attention to the emission current dial. Set the filament current knob to its minimum position.
5. Slowly decrease the voltage to its minimum position.
6. Turn off the *H-flux* power supply.

7. Close the leak valve completely, but do not overshoot past 0.
8. Close bellows valve # 1 completely.
9. Close the LL/buffer gate valve. The LL ion gauge will read below 2×10^{-6} Torr.
10. On the electronics rack, select "High Voltage Operate", then "Display Select", choose the option "ON", and finally select "Enter". Wait 5 min and then turn on the buffer ion gauge.
11. Wait for the buffer pressure to stabilize, then close bellows valve # 2 completely.
12. Wait for the buffer pressure to drop below 2×10^{-8} Torr before transferring the substrate into the growth chamber.
13. Close the hydrogen tank valve completely.
14. (optional) If the pumping efficiency of the turbo has dropped after a few cleaning cycles, it is possible that water vapor has built-up in the dry scroll pump. Water is one of the by-products of the hydrogen cleaning process. Open the gas ballast on the scroll pump for 10 min to allow atmospheric gas into the compression stage of the pump, which generates extra heat to help remove residual water.

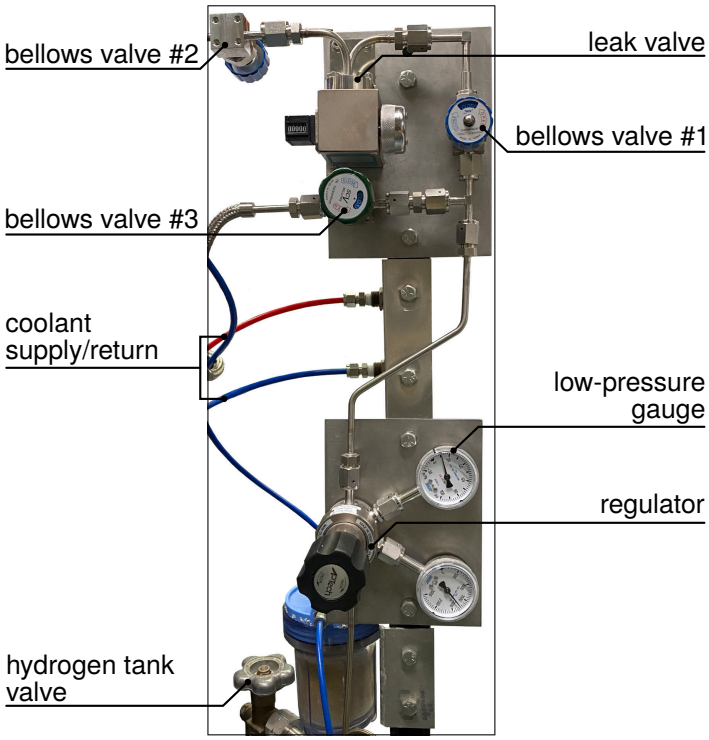

Figure A.1: Cd_3As_2 GEN2 hydrogen substrate cleaning station. Built by J. English and K. Olsson.

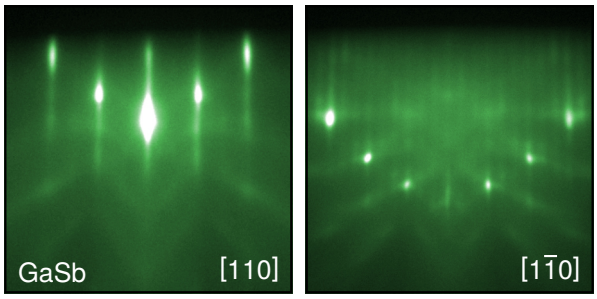

Figure A.2: RHEED patterns of an on-axis GaSb wafer after hydrogen cleaning. The Sb-rich (1×3) reconstruction is consistently produced under the cleaning conditions described in the text.

Appendix B

Retractable Cd_3As_2 effusion cells

Since the retractable Cd_3As_2 cells are only refilled about once per year, it's important to be mindful of failure modes during this less frequent maintenance event. Crashing risks, especially in the region where the dual-rail slider clamps onto the VAT gate valve, can be minimized by checking alignment carefully. This is, unfortunately, the only option with the current design. Additionally, the risk of scratching the cells against the stainless steel bellows can be addressed by having a second person guide the process from the side and making position adjustments upon encountering resistance, like a small degree of rotation. Here are some notes on working with these cells.

1. Retracting the cells: cool CdAs1 (upwards facing) and CdAs2 (downwards facing) to 25 °C on the day of the opening and wait for 1 h.
2. Turn off cell power supplies and Eurotherms. Disconnect power cables and thermocouples (TCs). Base TC on the left (inside), tip TC on the right (outside).
3. Verify that gate valves are fully open before the next step.

4. Slowly retract one cell at a time using a hand wheel attached to the lead screw. The resistance against atmospheric pressure should stay constant. Support the platform with another hand to prevent unnecessary torque. Fully retract both cells using the retracted position of CdAs1 as a reference [Figure B.1 (a)]. The in-vacuum length of the E-Science cell is 18.5 inches. Close both gate valves when done.

5. Venting to atmosphere is typically monitored by the LL ion gauge. First, confirm that the LL is evacuated by the turbo pump. Then, slowly open the valve isolating the LL from the manifold, which is typically maintained at high (static) vacuum.

6. Open the valve isolating the manifold from the retractable cells [Figure B.1 (b)]. Monitor the LL pressure.

7. For each cell, open the valve for the bellows and the extra valve for the dead space around its gate valve. Note: on CdAs1, the valve for the dead space will not open fully due to an obstruction.

8. Verify that the valve isolating the manifold from the growth chamber is closed. Loosen the LL door lock.

9. Turn off the turbo pump to initiate the vent sequence. Support the sagging bellows during the venting process.

10. After the turbo is vented, slowly open the system nitrogen vent valve and bring the LL pressure to atmosphere [see Figure B.1 (c)]. Monitor the growth chamber ion gauge.

11. Loosen the bolts on one cell at a time and leave the nuts in place. Note that pulling out CdAs1 can generate visible amounts of toxic dust.
12. At a work bench, note the crucible/cell combination and inspect the crucibles for cracks. Dispose of remaining source material.
13. If new crucibles are required, they will need to first be inserted into the cells and outgassed in the bake station before loading source material. For CdAs2, the tantalum screen needs to be re-threaded and placed in as well, but do not secure it in place yet.
14. Typical refill amount is 80 g of Cd_3As_2 per crucible.
15. Once maintenance events are completed, insert the cells by following the steps above in reverse order. Pay close attention to the resistance of the hand wheel.
16. To conserve source material, operating the cells at higher than normal temperature settings for a long period to outgas is not necessary. Instead, run 2-3 successive beam flux measurement (BFM) recipes in EPIC, which will help stabilize the charge inside the crucible.

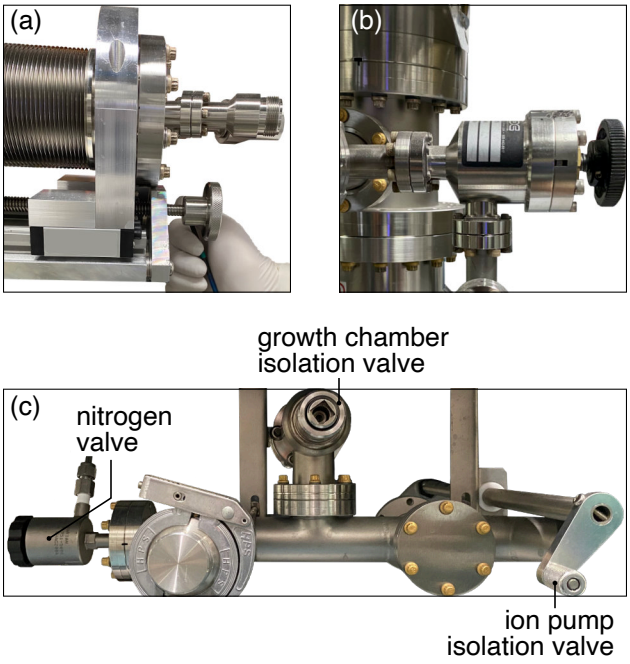

Figure B.1: (a) Fully retracted position of CdAs1. (b) Isolation valve between the retractable cells and the vacuum manifold. (c) Vacuum manifold with important components indicated.

Appendix C

(001) Cd_3As_2 growth window

Alongside efforts to improve the buffer layer growth, exploring the higher flux and higher temperature regime of Cd_3As_2 epitaxy is equally valuable. These studies should aim to identify the optimal Cd_3As_2 growth window on existing (001) buffer technology. It is also possible that higher fluxes might reveal a new growth mode.

Earlier work from our group [19, 51] had ventured in this direction, but was focused on the (112) orientation and limited by how much beam flux could be supplied without using up the only Cd_3As_2 effusion cell available. By installing two retractable effusion cells, the practical restrictions previously encountered are now lifted. Additionally, this dissertation has shown that electronic transport in (001) QWs can serve as a benchmark for assessing material quality, offering a standard structure to evaluate different growth conditions.

A region of the achievable flux-temperature phase space is illustrated in Figure C.1. In Chapter 2, it was demonstrated that increasing only the growth (substrate) temperature led to deterioration of the Cd_3As_2 surface, which suggests that expanding beyond the routine growth window should also involve increasing the flux. Interestingly, preliminary

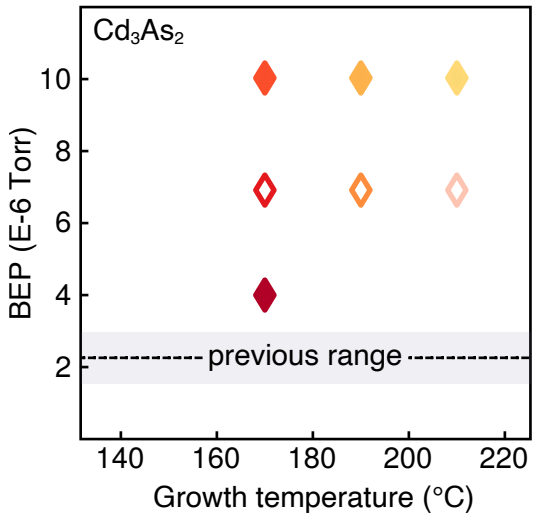

Figure C.1: Flux-temperature phase space for (001) Cd_3As_2 growth. Filled markers represent samples that have been grown, while empty ones are planned for the future.

AFM scans of samples grown under these higher flux/temperature conditions, shown in Figure C.2, exhibit larger Cd_3As_2 grain sizes with only a minor increase in roughness. The immediate question is understanding how changes in these growth conditions affect transport. One theory is that elevated growth temperatures lead to a higher concentration of charged point defects, like As vacancies, that may (1) increase scattering and (2) potentially contribute to higher electron densities. Additionally, when comparing transport properties in QW samples, it's important to consider variations in well thickness. This is because the growth rate significantly increases at higher fluxes, reaching up to approximately $3.6\,\mu m\,h^{-1}$.

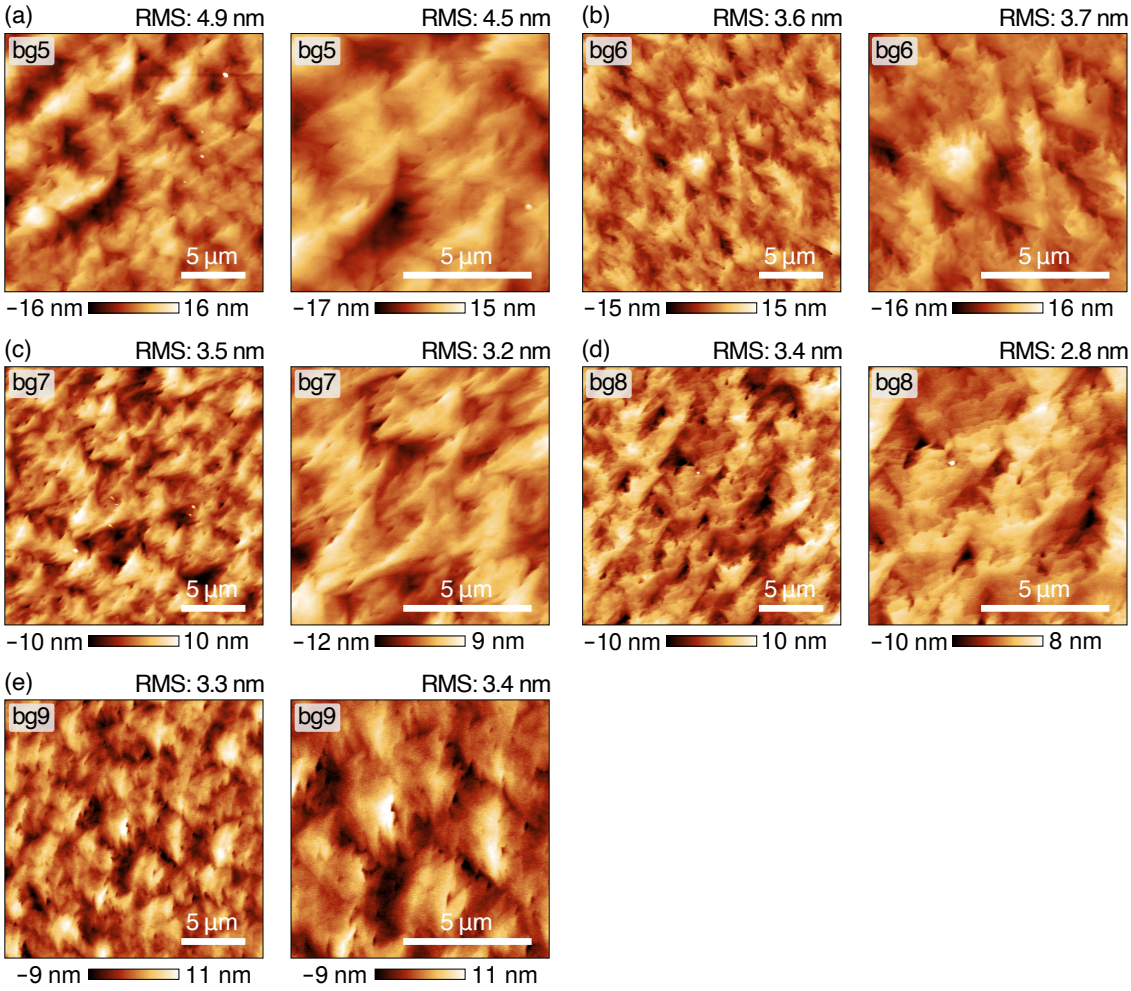

Figure C.2: AFM height maps of (001) Cd_3As_2 films grown at higher temperatures and beam fluxes. The same buffer structure of $Al_{0.45}In_{0.55}Sb$ was used for all films. The growth conditions for (a) and (b) are: 170 °C, 1×10^{-5} Torr. For (c) and (d): 190 °C, 1×10^{-5} Torr. For (e): 210 °C, 1×10^{-5} Torr. Sample IDs are indicated for reference. Apart from bg5, which is 80 nm thick, all Cd_3As_2 films are ~ 20 nm.

References

[1] K. V. Klitzing, G. Dorda, and M. Pepper, Phys. Rev. Lett. **45**, 494 (1980).

[2] D. J. Thouless, M. Kohmoto, M. P. Nightingale, and M. Den Nijs, Phys. Rev. Lett. **49**, 405 (1982).

[3] C. L. Kane and E. J. Mele, Phys. Rev. Lett. **95**, 146802 (2005).

[4] B. A. Bernevig, T. L. Hughes, and S.-C. Zhang, Science **314**, 1757 (2006).

[5] X.-L. Qi and S.-C. Zhang, Rev. Mod. Phys. **83**, 1057 (2011).

[6] N. Armitage, E. Mele, and A. Vishwanath, Rev. Mod. Phys. **90**, 015001 (2018).

[7] M. König, S. Wiedmann, C. Brüne, A. Roth, H. Buhmann, L. W. Molenkamp, X.-L. Qi, and S.-C. Zhang, Science **318**, 766 (2007).

[8] C.-Z. Chang, J. Zhang, X. Feng, J. Shen, Z. Zhang, M. Guo, K. Li, Y. Ou, P. Wei, L.-L. Wang, Z.-Q. Ji, Y. Feng, S. Ji, X. Chen, J. Jia, X. Dai, Z. Fang, S.-C. Zhang, K. He, Y. Wang, L. Lu, X.-C. Ma, and Q.-K. Xue, Science **340**, 167 (2013).

[9] R. Yu, W. Zhang, H.-J. Zhang, S.-C. Zhang, X. Dai, and Z. Fang, Science **329**, 61 (2010).

[10] M. J. Gilbert, Commun. Phys. **4**, 1 (2021).

[11] Z. Wang, H. Weng, Q. Wu, X. Dai, and Z. Fang, Phys. Rev. B **88**, 125427 (2013).

[12] I. Crassee, R. Sankar, W.-L. Lee, A. Akrap, and M. Orlita, Phys. Rev. Mater. **2**, 120302 (2018).

[13] B. Guo, A. C. Lygo, X. Dai, and S. Stemmer, APL Mater. **10**, 091116 (2022).

[14] A. C. Lygo, B. Guo, A. Rashidi, V. Huang, P. Cuadros-Romero, and S. Stemmer, Phys. Rev. Lett. **130**, 046201 (2023).

[15] B. Guo, W. Miao, V. Huang, A. C. Lygo, X. Dai, and S. Stemmer, Phys. Rev. Lett. **131**, 046601 (2023).

[16] B. Guo, A. C. Lygo, T. N. Pardue, and S. Stemmer, Phys. Rev. Mater. **6**, 034203 (2022).

[17] T. Liang, Q. Gibson, M. N. Ali, M. Liu, R. J. Cava, and N. P. Ong, Nat. Mater. **14**, 280 (2015).

[18] A. J. Rosenberg and T. C. Harman, J. Appl. Phys. **30**, 1621 (1959).

[19] T. Schumann, M. Goyal, H. Kim, and S. Stemmer, APL Mater. **4**, 126110 (2016).

[20] M. Goyal, S. Salmani-Rezaie, T. N. Pardue, B. Guo, D. A. Kealhofer, and S. Stemmer, APL Mater. **8**, 051106 (2020).

[21] E. O. Kane, J. Phys. Chem. Solids **1**, 82 (1956).

[22] E. O. Kane, J. Phys. Chem. Solids **1**, 249 (1957).

[23] E. O. Kane, in *Semiconductors and Semimetals, Vol. 1*, edited by R. K. Willardson and A. C. Beer (Elsevier, 1966) pp. 75–100.

[24] J. Cano, B. Bradlyn, Z. Wang, M. Hirschberger, N. P. Ong, and B. A. Bernevig, Phys. Rev. B **95**, 161306 (2017).

[25] H. Gao, J. W. Venderbos, Y. Kim, and A. M. Rappe, Annu. Rev. Mater. Res. **49**, 153 (2019).

[26] J. Bodnar, arXiv:1709.05845.

[27] W. Miao, B. Guo, S. Stemmer, and X. Dai, arXiv:2309.15457.

[28] C.-X. Liu, H. Zhang, B. Yan, X.-L. Qi, T. Frauenheim, X. Dai, Z. Fang, and S.-C. Zhang, Phys. Rev. B **81**, 041307 (2010).

[29] A. H. Castro Neto, F. Guinea, N. M. R. Peres, K. S. Novoselov, and A. K. Geim, Rev. Mod. Phys. **81**, 109 (2009).

[30] M. Büttiker, Phys. Rev. B **38**, 9375 (1988).

[31] G. Zhu, B. Guo, and S. Stemmer, Appl. Phys. Lett. **123**, 223101 (2023).

[32] M. A. Herman and H. Sitter, in *Molecular Beam Epitaxy: Fundamentals and Current Status* (Springer, 1996) pp. 215–277.

[33] H. Okamoto, J. Phase Equilibria **13**, 147 (1992).

[34] D. N. Nasledov and V. Y. Shevchenko, Phys. Stat. Sol. A **15**, 9 (1973).

[35] W. Zdanowicz and L. Zdanowicz, Annu. Rev. Mater. Sci. **5**, 301 (1975).

[36] G. A. Steigmann and J. Goodyear, Acta. Cryst. B **24**, 1062 (1968).

[37] M. N. Ali, Q. Gibson, S. Jeon, B. B. Zhou, A. Yazdani, and R. J. Cava, Inorg. Chem. **53**, 4062 (2014).

[38] T. N. Pardue, M. Goyal, B. Guo, S. Salmani-Rezaie, H. Kim, O. Heinonen, M. D. Johannes, and S. Stemmer, APL Mater. **9**, 051111 (2021).

[39] H. Kim, M. Goyal, S. Salmani-Rezaie, T. Schumann, T. N. Pardue, J.-M. Zuo, and S. Stemmer, Phys. Rev. Mater. **3**, 084202 (2019).

[40] Y. Nakazawa, M. Uchida, S. Nishihaya, S. Sato, A. Nakao, J. Matsuno, and M. Kawasaki, APL Mater. **7**, 071109 (2019).

[41] A. D. Rice, K. Park, E. T. Hughes, K. Mukherjee, and K. Alberi, Phys. Rev. Mater. **3**, 121201 (2019).

[42] V. J. Lyons and V. J. Silvestri, J. Phys. Chem. **64**, 266 (1960).

[43] J. B. Westmore, K. H. Mann, and A. W. Tickner, J. Phys. Chem. **68**, 606 (1964).

[44] S. X. Zhang, J. Zhang, Y. Wu, T. T. Kang, N. Li, X. F. Qiu, and P. P. Chen, Mater. Res. Express **7**, 106405 (2020).

[45] A. D. Rice, M. O. Liedke, M. Butterling, E. Hirschmann, A. Wagner, N. M. Haegel, and K. Alberi, APL Mater. **11**, 061109 (2023).

[46] P. J. Linstrom and W. G. Mallard, J. Chem. Eng. Data **46**, 1059 (2001).

[47] P. M. Mooney, J. Appl. Phys. **67**, R1 (1990).

[48] I. Vurgaftman, J. R. Meyer, and L. R. Ram-Mohan, J. Appl. Phys. **89**, 5815 (2001).

[49] J. W. Matthews and A. E. Blakeslee, J. Cryst. Growth **27**, 118 (1974).

[50] G. Tuttle, H. Kroemer, and J. H. English, J. Appl. Phys. **67**, 3032 (1990).

[51] M. Goyal, PhD Dissertation, UC Santa Barbara (2020).

[52] Y. Horikoshi, M. Kawashima, and H. Yamaguchi, Jpn. J. Appl. Phys. **25**, L868 (1986).

[53] J. H. Neave, P. J. Dobson, B. A. Joyce, and J. Zhang, Appl. Phys. Lett. **47**, 100 (1985).

[54] T. Ando, A. B. Fowler, and F. Stern, Rev. Mod. Phys. **54**, 437 (1982).

[55] A. Gold, Phys. Rev. B **35**, 723 (1987).

[56] D. A. Kealhofer, L. Galletti, T. Schumann, A. Suslov, and S. Stemmer, Phys. Rev. X **10**, 011050 (2020).

[57] L. Galletti, T. Schumann, T. E. Mates, and S. Stemmer, Phys. Rev. Mater. **2**, 124202 (2018).

[58] A. W. Ott, J. W. Klaus, J. M. Johnson, and S. M. George, Thin Solid Films **292**, 135 (1997).

[59] D. A. Kealhofer, H. Kim, T. Schumann, M. Goyal, L. Galletti, and S. Stemmer, Phys. Rev. Mater. **3**, 031201 (2019).

[60] J. G. Checkelsky, L. Li, and N. P. Ong, Phys. Rev. B **79**, 115434 (2009).

[61] F. D. M. Haldane, Phys. Rev. Lett. **61**, 2015 (1988).

[62] A. M. J. Schakel, Phys. Rev. D **43**, 1428 (1991).

[63] Y. Zhang, Z. Jiang, J. P. Small, M. S. Purewal, Y.-W. Tan, M. Fazlollahi, J. D. Chudow, J. A. Jaszczak, H. L. Stormer, and P. Kim, Phys. Rev. Lett. **96**, 136806 (2006).

[64] D. A. Abanin, P. A. Lee, and L. S. Levitov, Phys. Rev. Lett. **96**, 176803 (2006).

[65] D. A. Abanin, K. S. Novoselov, U. Zeitler, P. A. Lee, A. K. Geim, and L. S. Levitov, Phys. Rev. Lett. **98**, 196806 (2007).

[66] A. F. Young, C. R. Dean, L. Wang, H. Ren, P. Cadden-Zimansky, K. Watanabe, T. Taniguchi, J. Hone, K. L. Shepard, and P. Kim, Nat. Phys. **8**, 550 (2012).

[67] T. Morimoto, A. Furusaki, and N. Nagaosa, Phys. Rev. Lett. **114**, 146803 (2015).

[68] R. Yoshimi, A. Tsukazaki, Y. Kozuka, J. Falson, K. Takahashi, J. Checkelsky, N. Nagaosa, M. Kawasaki, and Y. Tokura, Nat. Commun. **6**, 6627 (2015).

[69] Y. Xu, I. Miotkowski, and Y. P. Chen, Nat. Commun. **7**, 11434 (2016).

[70] S. K. Chong, K. B. Han, A. Nagaoka, R. Tsuchikawa, R. Liu, H. Liu, Z. V. Vardeny, D. A. Pesin, C. Lee, T. D. Sparks, and V. V. Deshpande, Nano Lett. **18**, 8047 (2018).

[71] S. K. Chong, K. B. Han, T. D. Sparks, and V. V. Deshpande, Phys. Rev. Lett. **123**, 036804 (2019).

[72] J. Ziegler, D. A. Kozlov, N. N. Mikhailov, S. Dvoretsky, and D. Weiss, Phys. Rev. Res. **2**, 033003 (2020).

[73] H.-Z. Lu, W.-Y. Shan, W. Yao, Q. Niu, and S.-Q. Shen, Phys. Rev. B **81**, 115407 (2010).

[74] D. A. Kealhofer, R. Kealhofer, D. Ohara, T. N. Pardue, and S. Stemmer, Sci. Adv. **8**, eabn4479 (2022).

[75] S. Murzin and A. Jansen, Physica E Low Dimens. Syst. Nanostruct. **43**, 1576 (2011).

[76] M. Salehi, H. Shapourian, I. T. Rosen, M. Han, J. Moon, P. Shibayev, D. Jain, D. Goldhaber-Gordon, and S. Oh, Adv. Mater. **31**, 1901091 (2019).

[77] Y. Xu, I. Miotkowski, C. Liu, J. Tian, H. Nam, N. Alidoust, J. Hu, C.-K. Shih, M. Z. Hasan, and Y. P. Chen, Nat. Phys. **10**, 956 (2014).

[78] D. A. Kealhofer, M. Goyal, T. N. Pardue, and S. Stemmer, Phys. Rev. B **104**, 035435 (2021).

[79] C.-X. Liu, X.-L. Qi, X. Dai, Z. Fang, and S.-C. Zhang, Phys. Rev. Lett. **101**, 146802 (2008).

[80] S. Sun, H. Weng, and X. Dai, Phys. Rev. B **106**, L241105 (2022).

[81] J.-Y. You, C. Chen, Z. Zhang, X.-L. Sheng, S. A. Yang, and G. Su, Phys. Rev. B **100**, 064408 (2019).

[82] X. Liu, H.-C. Hsu, and C.-X. Liu, Phys. Rev. Lett. **111**, 086802 (2013).

[83] Y. Zeng, F. Xue, and A. H. MacDonald, Phys. Rev. B **105**, 125102 (2022).

[84] F. Dominguez, B. Scharf, and E. Hankiewicz, SciPost Phys. Core **5**, 024 (2022).

[85] J. Maciejko, T. L. Hughes, and S.-C. Zhang, Annu. Rev. Condens. Matter Phys. **2**, 31 (2011).

[86] M. König, H. Buhmann, L. W. Molenkamp, T. Hughes, C.-X. Liu, X.-L. Qi, and S.-C. Zhang, J. Phys. Soc. Jpn. **77**, 031007 (2008).

[87] G. M. Gusev, E. B. Olshanetsky, Z. D. Kvon, O. E. Raichev, N. N. Mikhailov, and S. A. Dvoretsky, Phys. Rev. B **88**, 195305 (2013).

[88] T. Khouri, S. Pezzini, M. Bendias, P. Leubner, U. Zeitler, N. E. Hussey, H. Buhmann, L. W. Molenkamp, M. Titov, and S. Wiedmann, Phys. Rev. B **99**, 075303 (2019).

[89] Y. Xu, G. Jiang, I. Miotkowski, R. R. Biswas, and Y. P. Chen, Phys. Rev. Lett. **123**, 207701 (2019).

[90] O. E. Raichev, Phys. Rev. B **85**, 045310 (2012).

[91] M. Kubisa and K. Ryczko, Phys. Rev. B **104**, L161406 (2021).

[92] J. Ahn and B.-J. Yang, Phys. Rev. Lett. **118**, 156401 (2017).

[93] C. Fang and L. Fu, Phys. Rev. B **91**, 161105 (2015).

[94] C.-X. Liu, X.-L. Qi, H. Zhang, X. Dai, Z. Fang, and S.-C. Zhang, Phys. Rev. B **82**, 045122 (2010).

[95] R. Winkler, in *Spin-Orbit Coupling Effects in Two-Dimensional Electron and Hole Systems* (Springer, 2003) pp. 201–205.

[96] P. Löwdin, J. Chem. Phys. **19**, 1396 (2004).

[97] S. Sun, Z. Song, H. Weng, and X. Dai, Phys. Rev. B **101**, 125118 (2020).

[98] Z. Song, S. Sun, Y. Xu, S. Nie, H. Weng, Z. Fang, and X. Dai, in *Memorial Volume for Shoucheng Zhang* (World Scientific, 2020) pp. 263–281.

[99] F. A. P. Blom, J. W. Cremers, J. J. Neve, and M. J. Gelten, Solid State Commun. **33**, 69 (1980).

[100] S. Jeon, B. B. Zhou, A. Gyenis, B. E. Feldman, I. Kimchi, A. C. Potter, Q. D. Gibson, R. J. Cava, A. Vishwanath, and A. Yazdani, Nat. Mater. **13**, 851 (2014).

[101] W. Beugeling, Phys. Rev. B **104**, 115428 (2021).

[102] J. Nilsson, A. H. C. Neto, F. Guinea, and N. M. R. Peres, Phys. Rev. Lett. **97**, 266801 (2006).

[103] J. Tworzydło, B. Trauzettel, M. Titov, A. Rycerz, and C. W. J. Beenakker, Phys. Rev. Lett. **96**, 246802 (2006).

[104] R. Jackiw, Phys. Rev. D **29**, 2375 (1984).

[105] M. Shayegan, E. P. De Poortere, O. Gunawan, Y. P. Shkolnikov, E. Tutuc, and K. Vakili, Phys. Status Solidi B **243**, 3629 (2006).

[106] S. Lai, H. Liu, Z. Zhang, J. Zhao, X. Feng, N. Wang, C. Tang, Y. Liu, K. S. Novoselov, S. A. Yang, and W.-B. Gao, Nat. Nanotechnol. **16**, 869 (2021).

[107] H. Liu, J. Zhao, Y.-X. Huang, X. Feng, C. Xiao, W. Wu, S. Lai, W.-B. Gao, and S. A. Yang, Phys. Rev. B **105**, 045118 (2022).

[108] Y. Gao, S. A. Yang, and Q. Niu, Phys. Rev. Lett. **112**, 166601 (2014).

[109] A. Kitaev, Ann. Phys. **303**, 2 (2003).

[110] J. Alicea, Rep. Prog. Phys. **75**, 076501 (2012).

[111] L. Fu and C. L. Kane, Phys. Rev. Lett. **100**, 096407 (2008).

[112] A. C. Potter and P. A. Lee, Phys. Rev. B **83**, 184520 (2011).

[113] C. Nguyen, H. Kroemer, and E. L. Hu, Appl. Phys. Lett. **65**, 103 (1994).

[114] L. Maier, J. B. Oostinga, D. Knott, C. Brüne, P. Virtanen, G. Tkachov, E. M. Hankiewicz, C. Gould, H. Buhmann, and L. W. Molenkamp, Phys. Rev. Lett. **109**, 186806 (2012).

[115] C.-H. Chen, E. L. Hu, W. V. Schoenfeld, and P. M. Petroff, J. Vac. Sci. Technol. B **16**, 3354 (1998).

[116] S. M. Frolov, M. J. Manfra, and J. D. Sau, Nat. Phys. **16**, 718 (2020).

[117] C.-Z. Li, C. Li, L.-X. Wang, S. Wang, Z.-M. Liao, A. Brinkman, and D.-P. Yu, Phys. Rev. B **97**, 115446 (2018).

[118] W. Yu, W. Pan, D. Medlin, M. Rodriguez, S. Lee, Z.-Q. Bao, and F. Zhang, Phys. Rev. Lett. **120**, 177704 (2018).

[119] C. Huang, B. T. Zhou, H. Zhang, B. Yang, R. Liu, H. Wang, Y. Wan, K. Huang, Z. Liao, E. Zhang, S. Liu, Q. Deng, Y. Chen, X. Han, J. Zou, X. Lin, Z. Han, Y. Wang, K. T. Law, and F. Xiu, Nat. Commun. **10**, 2217 (2019).

[120] Z. Wan, A. Kazakov, M. J. Manfra, L. N. Pfeiffer, K. W. West, and L. P. Rokhinson, Nat. Commun. **6**, 7426 (2015).

[121] F. Amet, C. T. Ke, I. V. Borzenets, J. Wang, K. Watanabe, T. Taniguchi, R. S. Deacon, M. Yamamoto, Y. Bomze, S. Tarucha, and G. Finkelstein, Science **352**, 966 (2016).

[122] G.-H. Lee, K.-F. Huang, D. K. Efetov, D. S. Wei, S. Hart, T. Taniguchi, K. Watanabe, A. Yacoby, and P. Kim, Nat. Phys. **13**, 693 (2017).

[123] S. P. Svensson, N. A. Mahadik, G. Kipshidze, D. Donetski, J. Zhao, and G. Belenky, J. Vac. Sci. Technol. A **41**, 040802 (2023).

[124] J. Tersoff, Appl. Phys. Lett. **62**, 693 (1993).

[125] L. He, L. E. Clinger, and C. J. K. Richardson, J. Vac. Sci. Technol. B **31**, 061204 (2013).